

1 Cloud response to co-condensation of water and organic vapors over the boreal 2 forest

3
4 Liine Heikkinen^{1,2}, Daniel G. Partridge³, [Sara Blichner^{1,2}](#), Wei Huang⁴, [Sara Blichner^{1,2}](#), Rahul
5 Ranjan^{1,2}, [Paul Bowen³](#), Emanuele Tovazzi³, Tuukka Petäjä⁴, Claudia Mohr^{1,2}, and Ilona
6 Riipinen^{1,2}

7 ¹Department of Environmental Science (ACES), Stockholm University, Stockholm, Sweden

8 ²Bolin Centre for Climate Research, Stockholm University, Stockholm, Sweden

9 ³Department of Mathematics and Statistics, Faculty of Environment, Science and Economy, University of Exeter,
10 Exeter, United Kingdom

11 ⁴Institute for Atmospheric and Earth System Research (INAR) / Physics, University of Helsinki, Helsinki, Finland

12
13 *Correspondence to:* Liine Heikkinen (liine.heikkinen@aces.su.se) and Ilona Riipinen (ilona.riipinen@aces.su.se)

14 Abstract

15 Accounting for the condensation of organic vapors along with water vapor (co-condensation) has been shown in
16 adiabatic cloud parcel model (CPM) simulations to enhance the number of aerosol particles that activate to form
17 cloud droplets. The boreal forest is an important source of biogenic organic vapors, but the role of these vapors in
18 co-condensation has not been systematically investigated. In this work, the environmental conditions under which
19 strong co-condensation -driven cloud droplet number enhancements would be expected over the boreal biome are
20 identified. Recent measurement technology, specifically the Filter Inlet for Gases and AEROSols (FIGAERO)
21 coupled to an iodide-adduct Chemical Ionization Mass Spectrometer (I-CIMS), is utilized to construct a volatility
22 distribution of the boreal atmospheric organics. Then, a suite of CPM simulations initialized with a comprehensive
23 set of concurrent aerosol observations collected in the boreal forest of Finland during Spring 2014 is performed.
24 The degree to which co-condensation impacts droplet formation in the model is shown to be dependent on the
25 initialization of [temperature, relative humidity, the](#) updraft velocity, aerosol size distribution, organic vapor
26 concentration and the volatility distribution. The predicted median enhancements in cloud droplet number
27 concentration (CDNC) due to accounting for the co-condensation of water and organics [fall on average between](#)
28 [16 and 22% \(interquartile range 9–14%\)](#). This corresponds to activating particles [121–166](#) nm smaller in
29 dry diameter, that would otherwise remain as interstitial aerosol. The highest CDNC enhancements (Δ CDNC) are
30 predicted in the presence of a nascent ultrafine aerosol mode with a geometric mean diameter of ~40 nm and no
31 clear Hoppel minimum, indicative of pristine environments with a source of ultrafine particles (e.g., via new
32 particle formation processes). Such aerosol size distributions are observed 30–40% of the time in the studied
33 boreal forest environment in spring and fall when new particle formation frequency is the highest [\(six years of](#)
34 [statistics\)](#). Five years of UK Earth System Model (UKESM1) simulations are further used to evaluate the
35 frequencies to which such distributions are experienced by an Earth System Model over the whole boreal biome.
36 The frequencies are substantially lower than those observed at the boreal forest measurement site (<6% of the
37 time) and the positive values, peaking in spring, are modeled only over Fennoscandia and western parts of Siberia.
38 [Overall, the similarities in the size distributions between observed and modeled \(UKESM1\) are limited, which](#)
39 [would limit the model's ability of this model, or any model with a similar aerosol representation, to project the](#)
40 [climate-relevance of co-condensation](#). ~~For the aerosol size distribution regime simulated by UKESM1~~ [For the](#)
41 [critical aerosol size distribution regime, offline simulations with the adiabatic parcel model reveal the](#) Δ CDNC
42 to be sensitive to the concentrations of semi-volatile and some intermediate-volatility organic compounds (SVOCs)

43 and IVOCs) especially when the overall particle surface area is low. The magnitudes of Δ CDNC remain less
44 affected by the more volatile vapors such as formic acid and extremely low and low volatility organic compounds
45 (ELVOCs and LVOCs) in the CPM simulations. The reasons for this are that most volatile organic vapors
46 condense inefficiently due to their high volatility below cloud base and the concentrations of LVOCs and ELVOCs
47 are too low to gain significant concentrations of soluble mass to reduce critical supersaturations enough for needed
48 for droplet activation to occur. Suppression-Reduction of the critical supersaturation caused by organic
49 condensation emerges as the main driver of the modeled Δ CDNC. The results highlight the potential significance
50 of co-condensation in pristine boreal environments close to sources of fresh ultrafine particles. For accurate
51 predictions of co-condensation effects on CDNC, also in larger scale models, an accurate ~~the~~ representation of the
52 aerosol size distribution is of essence critical. Further studies targeted at finding observational evidence and
53 constraints for co-condensation in the field are encouraged.

55 1 Introduction

56 Boreal forests emit significant quantities of volatile organic compounds (VOCs, Guenther et al., 1995; Artaxo et
57 al., 2022), such as monoterpenes, that undergo oxidation in the atmosphere. The condensable oxidation products
58 contribute considerably to the secondary organic aerosol (SOA) mass concentrations in the boreal forest air (e.g.,
59 Tunved et al., 2006; Artaxo et al., 2022). The emissions of monoterpenes are strongly temperature-dependent,
60 which leads – together with the higher oxidative potential in the sunlit months – to highest biogenic SOA
61 concentrations in summer (Paasonen et al., 2013; Heikkinen et al., 2020; Mikhailov et al., 2017). This has recently
62 been shown to have implications for cloud properties above the boreal forest through the availability of more
63 cloud condensation nuclei (CCN; Yli-Juuti et al., 2021; Petäjä et al., 2022; Paasonen et al., 2013). Under constant
64 meteorological conditions in the boreal forest, an increase in aerosol concentration typically results in an increase
65 in cloud droplet number concentration (CDNC) and smaller average droplet size for a given liquid water content
66 (Yli-Juuti et al., 2021). These effects alter the cloud brightness making clouds scatter incoming solar radiation
67 more efficiently (Twomey effect; Twomey, 1974, 1977). The relationships between the number of aerosol
68 particles, CDNC, and their effects on climate are, however, non-linear and complex, which makes aerosol-cloud
69 interactions the largest source of uncertainty in radiative forcing estimates from climate models (e.g., Lohmann
70 and Feichter, 2005; Carslaw et al., 2013; Bellouin et al., 2020). The development of “bottom-up” predictive
71 models is needed for providing accurate, yet robust, simplifications of key processes involved in aerosol-cloud
72 interactions – eventually for inclusion in climate models in computationally efficient parameterizations.

73 Numerous studies have been carried out to understand the role of condensable organic vapors in SOA
74 formation (e.g., Hallquist et al., 2009; Shrivastava et al., 2017) and hence the concentrations of CCN (i.e. particles
75 of at least 50–100 nm in diameter for the water vapor supersaturations typical of the boreal environments; Cerully
76 et al., 2011; Sihto et al., 2011; Paramonov et al., 2013; Hong et al., 2014; Paramonov et al., 2015). The yields of
77 volatile, intermediate-volatility or semi-volatile organic compounds (VOCs, IVOCs, or SVOCs) from
78 monoterpene oxidation, such as those of pinonaldehyde, formic acid, or acetic acid, are generally much higher
79 than those of the readily condensable lower-volatility vapors (low-volatility organic compounds, LVOCs and
80 extremely low volatility organic compounds, ELVOCs), but they are typically not considered directly important
81 for SOA or CCN formation. The above-mentioned volatility classes are determined based on the volatilities of

82 individual compounds binned into a volatility basis set (VBS; Donahue et al., 2006): VOCs have a saturation
83 vapor concentration (C^* ; given in units of $\mu\text{g m}^{-3}$ throughout the paper) of at least $10^7 \mu\text{g m}^{-3}$, IVOCs are distributed
84 in the C^* range of $[10^3, 10^6] \mu\text{g m}^{-3}$, SVOCs of $[1, 100]$, LVOCs of $[10^{-3}, 10^{-1}]$ and ELVOCs have a C^* below 10^{-4}
85 $\mu\text{g m}^{-3}$ (e.g., Donahue et al., 2011). While VOCs, IVOCs, and some SVOCs are unlikely to produce significant
86 concentrations of SOA at ground level without additional oxidation steps or ~~reactive uptake~~ multiphase
87 chemistry, ~~some of them can condense at higher altitudes if transported aloft (e.g., Murphy et al., 2015).~~ In
88 addition, aerosol liquid water plays a key role in determining the amount of SVOCs and IVOCs in the condensed
89 phase. Liquid water acts as an absorptive medium, and a higher liquid water content can enable a higher quantity
90 of organic vapors to partition into the condensed phase. However, the role of water in determining partitioning
91 coefficients is often neglected when absorptive partitioning theory (Pankow et al., 2001) is applied. Barley et al.
92 (2009) demonstrated that the inclusion of water, when predicting absorptive partitioning using Raoult's law, could
93 lead to evident increases in organic aerosol (OA) mass concentrations under atmospherically relevant OA
94 loadings. Later work by Topping and McFiggans (2012) showed ~~in turn~~ how under a decreasing temperature
95 trend, the concentration of aerosol liquid water increases making the solution particle more dilute enabling
96 enhanced dynamic partitioning of organic vapors (together with water vapor). ~~likely~~ This work focuses
97 on the dynamic SVOC and IVOC condensation together with water vapor (co-condensation) in rising and cooling
98 air motions, and the effects co-condensation poses on cloud microphysics.

99 Warm (liquid) clouds can form when air rises and cools, eventually leading to the air being supersaturated
100 with water vapor. The excess water vapor condenses onto aerosol particles, rapidly growing them into cloud
101 droplets. While water ~~vapor~~ represents the most abundant vapor in the atmosphere, also other trace species can
102 influence the cloud droplet activation process as the cooling of the rising air triggers also their condensation. The
103 partitioning of these other vapors is partially driven by the decrease in temperature itself, which makes the species
104 less volatile, but more important it is the increase in aerosol liquid water, and the dilution of the aerosol solution
105 that enables them to partition to the liquid phase (Topping and McFiggans, 2012). As the trace vapors condense
106 in the rising air under sub-saturated conditions, the molar fraction of water in the swelling ~~droplets-aerosol~~
107 particles increases slower than in the absence of this co-condensation process, which in turn leads to the
108 condensation of additional water by the time the air parcel reaches lifting condensation level. The co-condensation
109 of water with other trace vapors eventually leads to a reduction in critical supersaturation (s^*) required for droplet
110 activation of the particles due to an increased amount of organic solute (Topping and McFiggans, 2012), as
111 described by Köhler theory (Köhler, 1936). Topping et al. (2013) studied the impact of organic co-condensation
112 on CDNC using a cloud parcel model (CPM) initialized with a suite of realistic conditions describing the aerosol
113 particle number size distribution (PNSD), composition, and ~~organic aerosol (OA)~~ volatility distribution. They
114 showed significant enhancements in CDNC (ΔCDNC up to roughly 50%) when comparing simulations with
115 organic condensation (CC) to simulations without it (noCC). In addition to co-condensing organics and water,
116 also co-condensation of nitric acid and ammonia together with water has been suggested to enhance CDNC in
117 earlier process modeling studies (e.g., Kulmala et al., 1993; Korhonen et al., 1996; Hegg, 2000; Romakkaniemi
118 et al., 2005). Direct experimental studies of co-condensation remain challenging, however, as aerosol particles are
119 typically dried during the sampling process and the loss of liquid water may lead to evaporation of co-condensed
120 organics, too. While direct observational evidence of ~~organic co-condensation is scarce in the atmosphere is still~~
121 lacking, recent laboratory studies show significant water uptake due to co-condensation of propylene glycol and

122 water onto ammonium sulfate particles (Hu et al., 2018). In addition, ambient observations from Delhi and Beijing
123 suggest co-condensation of hydrochloric acid (HCl) or nitric acid (HNO₃) with water vapor, respectively, to be of
124 essence in reproducing particle hygroscopicities corresponding to the visibility measurements during haze events
125 (Gunthe et al., 2021; Wang et al., 2020).

126 The cloud response to co-condensation in the form of Δ CDNC has been previously shown to ~~is the~~ result
127 from the ~~of a~~ complex interplay between updraft velocity, PNSD and organic compound volatility distribution
128 (Topping et al., 2013). For the same amount of organic vapor, Topping et al. (2013) modelled a non-linear updraft
129 response of Δ CDNC. The highest Δ CDNC were obtained when updrafts were below 1 m s⁻¹, but the peak Δ CDNC
130 was dependent on the initial PNSD characteristics. Under higher updrafts, the modelled Δ CDNC was found to
131 decrease exponentially as a function of updraft, but the asymptote plateau of the curve depended on the initial
132 PNSD – although the dependence on the exact parameters describing multimodal PNSD were not extensively
133 explored. If assumed representative of the global continents, Δ CDNC values of tens of percent could impose a
134 significant impact on predictions of cloud albedo and the Earth's radiative budget. In fact, Topping et al. (2013)
135 suggest accounting for co-condensation could result in up to 2.5% increase in cloud albedo (corresponding to
136 global Δ CDNC = 40%). This albedo increase would translate into a -1.8 W m⁻² change in the global cloud
137 radiative effect over land. Topping et al. (2013) stress, however, that the impacts of co-condensation will be
138 spatially heterogeneous because of variable surface albedo and variation in VOC sources. For comparison, one
139 should note that the net radiative effect of clouds is approximately -20 W m⁻² (Boucher et al., 2013). The recent
140 best estimate of the effective radiative forcing from aerosol-cloud interactions is, on the other hand, -1.0 [-1.7 to
141 -0.3] W m⁻² (Forster et al., 2021). The potential contribution of co-condensation to estimates of in aerosol-radiative
142 forcing ~~due to aerosol-cloud-climate feedbacks or to future cloud radiative effects~~ remains unclear.

143 Boreal forests make up about one third of the Earth's forested area, which makes the boreal biome ~~it~~ an
144 important source of biogenic organic vapors that could affect droplet activation in warm clouds through co-
145 condensation. Δ CDNC due to co-condensation over the boreal forest could reduce the albedo over the dark boreal
146 forest canopy. In a warming climate, temperature-dependent biogenic terpene emissions (Guenther et al., 1993)
147 are expected to rise (e.g., Turnock et al., 2020). These increasing emissions enrich the ambient pool of organics
148 available for condensation in rising air. As suggested in Topping et al. (2013), through the effects organic co-
149 condensation poses on CDNC, organic co-condensation could enhance the proposed negative climate feedback
150 mechanism associated with the biogenic SOA (Kulmala et al., 2004; Spracklen et al., 2008; Kulmala et al., 2014;
151 Yli-Juuti et al., 2021), the magnitude of which is currently highly uncertain (Thornhill et al., 2021; Sporre et al.,
152 2019; Scott et al., 2018; Paasonen et al., 2013; Sporre et al., 2020).

153 Since the publication of the Topping et al. (2013) study, improved constraints of the effective volatilities
154 of organic aerosol (e.g., Thornton et al., 2020) can be placed ~~are~~ available through the application of chemical
155 ionization mass spectrometers (CIMS) providing molecular level information on gas- and particle-phase
156 composition in near-real time. With the up-to-date volatility parameterizations using the molecular formulae
157 retrieved from CIMS data, volatility distributions can be calculated along a volatility scale ranging from ELVOCs
158 to VOCs, while previous techniques could not enable constraints on volatilities exceeding $C^* = 1000 \mu\text{g m}^{-3}$
159 (SVOC) (Cappa and Jimenez, 2010). This means that a notable amount of semi- and intermediate volatility vapors
160 with high co-condensation potential were not included in the early organic co-condensation work (Topping et al.,

2013; Crooks et al., 2018). The recent methodological developments motivate revisiting work of Topping et al. (2013), as potentially large concentrations of condensable organic vapors have been so far neglected.

In this study, the cloud response to the co-condensation of organic vapors over the boreal forest of Finland is investigated using a CPM. Measurements and parameterization techniques involving FIGAERO-I-CIMS data are utilized to constrain the volatility distribution of organics for these simulations. In addition, to ensure realistic modeling scenarios, simultaneously recorded measurements of PNSD and chemical composition from the Aerosol Chemical Speciation Monitor (ACSM) are used for the CPM initialization. 97 unique CPM simulations are performed, initialized with conditions from boreal spring and early summer following measurement time series recorded during the Biogenic Aerosols – Effects on Clouds and Climate (BAECC) campaign at the Station Measuring Atmosphere–Ecosystem Relationships (SMEAR) II (Hari and Kulmala, 2005) in Finland (Petäjä et al., 2016) and the sensitivity to updraft velocity meteorological conditions is studied. These simulations are then used to characterize the environmental conditions (with respect to the size distribution and organic aerosol volatility distribution characteristics) that promote co-condensation-driven CDNC enhancements in the boreal atmosphere. The frequencies to which a strong cloud response to co-condensation can be expected and its potential spatiotemporal variability over the boreal biome is further investigated using long-term measurements from SMEAR II station and UK Earth System Model (UKESM1) simulations.

2 Methods and ~~d~~Data

This section covers the description of the main modeling tools and measurement data used in this work involving the description of the CPM utilized (Sect. 2.1), the CPM initialization and simulation setup (Sect. 2.2.), and CPM input data measurements and data processing, with independent sections dedicated to the retrievals of volatility distributions for atmospheric organics (Sect. 2.3 and subsections therein). The final section is dedicated for describing the UKESM1 simulations (Sect. 2.4).

2.1 The adiabatic cloud parcel model (~~ICPM~~PARSEC-UFO)

The base of the CPM chosen for this study is the Pseudo-Adiabatic bin-microphysics university of Exeter Cloud parcel model (PARSEC). It was developed based on the Institute for Marine and Atmospheric research Utrecht (IMAU) pseudo-adiabatic CPM (ICPM, Roelofs and Jongen, 2004; Roelofs, 1992) to allow for simulation of both pseudo-adiabatic and adiabatic ascents of air parcels (Partridge et al., 2011, 2012) as well as numerous optimizations to reduce simulation computational costs, such as a variable time-stepping scheme option for the dynamics/microphysics. PARSEC simulates the condensation and evaporation of water vapor on aerosol particles, particle activation to cloud droplet, unstable growth, collision and coalescence between droplets, and entrainment. In all simulations performed in this study PARSEC is used in adiabatic ascent configuration and the fixed time-stepping option in PARSEC is employed.

The model can be initialized with aerosol populations consisting of one or more internal or external mixtures of sulfuric acid, ammonium bisulfate, ammonium sulfate, OA, black carbon, mineral dust and sea salt. The PNSD are presented in a moving-center binned microphysics scheme comprising 400 size bins between 25 nm and 5 μm in dry radii, which are constructed at model initialization from the three parameters describing log-normal size distributions for the i number of modes – the geometric mean diameter (D_i), the total mode number concentration (N_i), and the geometric standard deviation (σ_i). The model can be initialized with up to four log-normal aerosol modes. The ~~ICPM~~PARSEC further provides time evolutions of key thermodynamic and

201 microphysical parameters e.g., the air parcel temperature (T), pressure (p), supersaturation (s), altitude (z) and the
 202 aerosol particle and hydrometeor size distributions.

203 The dynamical equations used in ~~the ICPMPARSEC~~ to simulate the adiabatically ascending air parcel
 204 equations are ~~the~~ same to those presented by Lee and Pruppacher (1977), where the vertical parcel displacements
 205 are determined by the updraft velocity (w , set to a fixed positive constant value in the ~~ICPM PARSEC~~
 206 simulations):

$$\frac{dz}{dt} = w. \quad (1)$$

207 The changes in pressure are calculated assuming hydrostatic balance and the temperature decrease along the ascent
 208 follows the dry adiabatic lapse rate while also accounting for the latent heat release due to condensation:

$$-\frac{dT}{dt} = \frac{gw}{c_{p,a}} + \frac{L_e}{c_{p,a}} \frac{dx_v}{dt} + \mu_j \left[\frac{L_e}{c_{p,a}} (x_v - x'_v) + (T - T') \right] w \quad (2)$$

209 where g is the acceleration of gravity, L_e the latent heat of evaporation, $c_{p,a}$ the specific heat capacity of air and x_v
 210 the water vapor mixing ratio of the air parcel. μ_j is the entrainment rate describing mixing of parcel air with
 211 environmental air characterized with x'_v and T' . ~~In this study, in which adiabatic simulations are performed,~~
 212 ~~entrainment is not considered ($\mu_j = 0$).~~ The water vapor mixing ratio in the air parcel changes with the evolving
 213 ambient supersaturation:

$$\frac{ds}{dt} = \frac{p}{\varepsilon e_s} \frac{dx_v}{dt} - (1 + s) \left[\frac{\varepsilon L_e}{R_a T^2} \frac{dT}{dt} + \frac{g}{R_a T} w \right], \quad (3)$$

214 where $\varepsilon = R_a/R_v = M_w/M_a = 0.622$ i.e., the ratio between the specific gas constants for air and water vapor,
 215 ~~respectively~~, or alternatively the molecular weight of water and air, ~~respectively~~. e_s is the saturation vapor pressure
 216 of water. To solve the ordinary differential equations (Eqs. 2–3), the time derivative of the water vapor mixing
 217 is approximated as

$$\frac{dx_v}{dt} \approx -\frac{\Delta x_L}{\Delta t} - \mu_j (x_v - x'_v + x_L) w \quad (4)$$

218 where Δt is the model time step (~~$10^{-3} 0.1$~~ seconds) and the liquid water mixing ratio (x_L) is calculated as a sum of
 219 the liquid water mixing ratio across all the 400 size bins (index i) for each assigned mode composition (index j):

$$\Delta x_L = \frac{4\pi\rho_w}{3\rho_a} \sum_{i=1}^{n_a} \sum_{j=1}^{n_b} n_{ij} (r_{ij}^3 - r_{ij, \text{dry}}^3), \quad (5)$$

220 where ρ_w is density of water, ρ_a is the density of ~~the particle dry mass dry air~~, n_{ij} is the number of particles within
 221 size bin i and composition j , and finally r_{ij} and $r_{ij, \text{dry}}$ are the wet and dry radii of the particles, respectively. The
 222 wet radii and hence also the particle masses (m) change as water condenses onto the particle (indices dropped for
 223 simplicity):

$$\frac{dm}{dt} = 4\pi\rho_w r^2 \frac{dr}{dt} = \frac{4\pi\rho_w r (S - S_{\text{eq}})}{\frac{\rho_w RT}{\text{DIFF}_v^* e_s} + \frac{L_e \rho_w}{kT} \left(\frac{L_e}{RT} - 1 \right)}, \quad (6)$$

224 where k is the thermal conductivity of air, and DIFF_v^* is size-dependent water vapor diffusivity (from Pruppacher
 225 and Klett, 1997). Eq. (6) is approximated within ~~the ICPMPARSEC~~ using a linearized form of the condensation
 226 equation (Hänel, 1987). Finally, S is the ambient saturation ratio ($S = s + 1$) and S_{eq} ($S_{\text{eq}} = \text{RH} / 100\%$) the
 227 equilibrium saturation ratio over the (spherical) wet particle surface, the difference of which determines the

228 quantity of excess vapor for the diffusional growth of the particle. While S depends on the updraft source and
 229 condensation sink (Eq. 3), S_{eq} depends on the particle wet radius and composition and it can be calculated using
 230 the Köhler equation (Köhler, 1936), traditionally expressed as:

$$S_{\text{eq}} = \frac{e}{e_s} = a_w \exp\left(\frac{2M_w \gamma}{RT \rho_w r}\right) \quad (7)$$

231 where e is the partial vapor pressure of water in equilibrium, a_w the water activity, γ the droplet surface tension
 232 (assumed to be that of water; see Table 1), R the universal gas constant, T the droplet temperature and r the droplet
 233 radius. Assuming dilute droplets, Eq. 7 is approximated in ICPM-PARSEC as follows for the equilibrium
 234 supersaturation ratio (Hänel, 1987):

$$S_{\text{eq}} \approx \exp\left(\frac{A}{r} - \frac{B}{\left(\frac{r}{r_{\text{dry}}}\right)^3 - 1}\right), \quad (8)$$

235 where

$$A = \frac{2M_w \gamma}{RT \rho_w} \quad (9)$$

236 and

$$B = \frac{\phi_s M_w \varepsilon_V \rho_s \nu}{M_s \rho_w} \quad (10)$$

$$B = \frac{3n_s M_w}{4\pi \rho_w}$$

237 A and B in Eqs. (9) and (10) are the Köhler coefficients, where M_w is the molecular weight of water (g mol^{-1}), M_s
 238 refers to the molar mass of the soluble fraction, ρ_w is the density of water (g m^{-3}),
 239 n_s is the total number of solutes (mol), ϕ_s is the osmotic coefficient of salt in the solution ($\phi_s \approx 1$ in ideal
 240 solutions), ν is the dissociation constant, and ρ_s and ε_V are the density and the volume fraction of the soluble
 241 mass in the aerosol particle, respectively. The dissociation constant is calculated as $\nu = (\sum_i c_i^+ + \sum_j c_j^-) / \sum_{ij} c_{ij}$,
 242 where, c_i^+ and c_j^- are the concentrations of positive and negative ions and c_{ij} is the concentration (mol L^{-1}) of the
 243 electrolytes in solution. For detailed descriptions of the B term, the reader is directed to Roelofs (1992a).

244 The Raoult term (Eq. 10) is reformulated within the ICPM in terms of solute concentrations enabling its
 245 adjustments by dissolving or partially dissolving chemical constituents. For detailed descriptions of the B term,
 246 the reader is directed to Roelofs (1992).

247 PARSEC has been further extended to include Köhler and condensation/evaporation equations for
 248 organic species of varying volatilities (Lowe, 2020). This extension of the model is referred to as PARSEC with
 249 the Unified Framework for Organics (PARSEC-UFO), and it is the CPM version used throughout the presented
 250 study. Within PARSEC-UFO, the volatility distributions are given using the VBS framework (Donahue et al.,
 251 2006) with q volatility bins – each assigned with a different saturation vapor concentration, C^* . The
 252 condensation/evaporation equation for organic species is described in the same manner as in Topping et al. (2013)
 253 and as shown for water vapor in Eq (6):

$$\frac{dm_q}{dt} = \frac{4\pi \rho_w r \text{DIFF}_g^* (S_q - S_{\text{eq},q}) e_{s,q}}{\frac{\text{DIFF}_g^* \Delta H_{\text{vap},q} S_{\text{eq},q} e_{s,q} \rho_q}{\lambda T} \left(\frac{\Delta H_{\text{vap},q}}{R_{v,q} T} - 1 \right) + \rho_q R_{v,q} T} \quad (11)$$

where DIFF_g^* is the gas phase diffusivity (see details in Topping et al., 2013 supplementary information), and λ is the heat conductivity of air. Both DIFF_g^* and λ are corrected for the transition regime of condensation. $\Delta H_{\text{vap},q}$ is the enthalpy of vaporization, $e_{s,q}$ the saturation vapor pressure, $S_{\text{eq},q}$ the equilibrium saturation ratio and ρ_q the density of organic species in the q^{th} volatility bin. $S_{\text{eq},q}$ is calculated analogous to the Köhler equation (Eq. 8):

$$S_{\text{eq},q} = a_q \exp\left(\frac{2v_q \gamma}{RT r}\right) \quad (12)$$

where a_q is the activity of q^{th} volatility bin in the bulk condensed phase, which equals the molar fraction of q due to the ideal solution approach of the study, and v_q is the molar volume of q . Following the organic condensation, the Köhler B term (Eq. 10) is updated along the adiabatic ascent, which impacts S_{eq} for water and thereby its condensation. Finally, as temperature decreases along the parcel's adiabatic ascent, the reductions in C^* are accounted for using an Arrhenius-type Clausius-Clapeyron relation:

$$C^* = C^*(T_{\text{ref}}) \exp\left(\frac{\Delta H_{\text{vap}}}{R} \left(\frac{1}{T_{\text{ref}}} - \frac{1}{T}\right)\right), \quad (13)$$

where R is the universal gas constant and T is the air parcel's ambient temperature in Kelvin, and T_{ref} is 298.15 K. The $C^*(T_{\text{ref}})$ are calculated within PARSEC-UFO using the initial conditions as reference. ΔH_{vap} remain constant throughout the simulations in this study, and are not C^* -dependent for simplicity. It should be noted that the time step of 0.1 seconds can be too high for solving Eq. (11) for the highest volatility bins. For instance, during condensation the model may encounter

$$m_q + \frac{dm_q}{dt} < 0.$$

If this happens then the condensation step is rejected, and instead condensation happens with a temporary timestep of $dt/2$ across two iterations. This ensures non-negative m_q . We should stress, that this sub-timestep is a new feature unique to PARSEC-UFO which is different to the variable time-stepping scheme option available in PARSEC.

2.21.1 Gas particle partitioning of organics PARSEC-UFO initialization and simulation setup

The simulations shown within this work are performed with PARSEC-UFO with or without co-condensation. Initially, before the start of the adiabatic ascent, an initialization takes place in PARSEC-UFO. This involves the calculation of the binned wet particle number size distribution and in the case, where co-condensation is enabled, the initialization of the volatility distribution of organics. The binned wet PNSD is calculated using the parameters describing a dry log-normal PNSD (N_i , D_i , σ_i), information on aerosol chemical composition (mass fractions of chemical species), initial RH and temperature – all given as inputs for the model. For simulations including co-condensation, the organic volatility distribution with q volatility bins is also given as input. The input volatility distribution input is required to reveal only the relative proportions of each volatility bin, and the organic mass per volatility bin includes both organic vapor ($C_{g,q}$) and particle phase concentrations ($C_{p,q}$; $C_{g+p,q} = C_{g,q} + C_{p,q}$) of

the compounds with a given C^* . When co-condensation is turned on, PARSEC-UFO takes in the summed volatility distributions (gas+particle phase i.e., $C_{g+p,q} = C_{g,q} + C_{p,q}$) –corrected for the PARSEC-UFO initialization temperature offline (Sect. 2.3) – as input. It is then assumed upon PARSEC-UFO initialization that the gas and particle phase are in equilibrium under the initialization RH. Finally, PARSEC-UFO solves partitioning coefficients for each volatility bin (ζ_q) i.e., the distribution of organic mass between gas and particle phase:

$$\zeta_q \equiv \frac{C_{p,q}}{C_{p,q} + C_{g,q}} \quad (144)$$

where the total particle phase organic mass concentration across all volatility bins is

$$C_p = \sum_q C_{p,q} = \sum_q C_{g+p,q} \zeta_q \quad (152)$$

and the partitioning coefficients depend on C^* as follows

$$\zeta_q = \frac{C_p}{C_p + C_q^*} \quad (163)$$

Each ζ_q is solved iteratively from Equations (152–163) following absorptive partitioning theory including water (Barley et al., 2009), as it was done by Topping et al. (2013) at model initialization assuming equilibrium conditions. The iterative method is possible, as – Similarly, as in the work of Topping et al. (2013), C_p is constrained –using the by the –initial PNSD and the organic mass fraction, and –in addition to the the relative proportions of the various–volatility bins (volatility distribution shape) are preserved. As assuming equilibrium conditions limits the amount of organic vapor available for co-condensation, it may also reduce the cloud response to co-condensation. Therefore, the initial organic vapor concentrations provided here can be taken as a lower limit.

Overall, 97 daytime scenarios (local time between 10:00 and 19:00) are simulated adiabatically with PARSEC-UFO. The initialization data originate from the Biogenic Aerosols – Effects on Clouds and Climate (BAECC) campaign, which took place in 2014 at the Station Measuring Ecosystem–Atmosphere Relationships (SMEAR) II in Hyytiälä, Finland (Petäjä et al., 2016). The measurements and data processing relevant to this study are described in Sect. 2.3. The configuration of PARSEC-UFO used in this study only considers the adiabatic ascent of an air parcel, without treatment of variable vertical updraft during ascent, droplet collision and coalescence or entrainment. The simulations are performed for fixed updraft velocities of 0.1 m s^{-1} , 0.3 m s^{-1} , and 1.0 m s^{-1} , with and without co-condensation. During the CPM simulation period, SMEAR II was under daytime clouds roughly 50–60% of the time (Ylivinkka et al., 2020), which were most often low level clouds motivating selection of updraft velocities. The initial atmospheric pressure and relative humidity are set to 980 hPa and 90%, respectively, in all simulation scenarios, unless otherwise stated. The PARSEC-UFO initialization temperature varies throughout the simulation set, and is taken from interpolated radiosonde data that represents the 90% initialization RH (Sect. 2.3). The selection of the 90% RH was motivated by the previous study by Crooks et al. (2018). However, we acknowledge that more work is needed to better harmonize this parameter, along with initialization pressure, to in-situ aerosol measurements. Each modelled scenario has log-normal parameters describing a bimodal aerosol size distribution from BAECC measurements and the organic mass fraction from ACSM measurements (Sect. 2.3). The rest of the mass is assumed to be ammonium sulfate, which is generally a good approximation for SMEAR II (Heikkinen et al., 2020). For the simulations performed here, BC is not included given its small (about <5%) contribution to aerosol mass from late spring to summer (Luoma, 2021). While PARSEC-UFO does not utilize κ -Köhler theory (Petters and Kreidenweis, 2008), it might be useful to

320 know that the assumed hygroscopicity, if translated to the hygroscopicity parameter κ , would be 0.14 and 0.72 for
321 organics and ammonium sulfate, respectively (ideal solution; median $\kappa_{\text{tot}} \approx 0.32$). The assumed overall
322 hygroscopicity is therefore likely to be overestimated, and it would exceed κ determined for SMEAR II
323 experimentally in previous studies (e.g., Sihto et al., 2011 suggest $\kappa = 0.18$). Due to the likely overestimation of
324 aerosol liquid water at initial conditions, it is also likely that the amount of organic vapor available for co-
325 condensation after PARSEC-UFO initialization is underestimated.

326 Table 1 contains a summary of the simulation input data along with the values used for mass
327 accommodation coefficient, surface tension, the vaporization enthalpy and effective soluble fraction of organics
328 as well as the number of PNSD size bins. A more comprehensive look into the input data can be found in Table
329 S.1. The simulation output at 50 m above cloud base, discussed later in the results section of the paper (Sect. 3),
330 is summarized in Table 2. Particles exceeding the critical radius (calculated by Köhler theory) in their wet radii
331 are considered as cloud droplets in this work. The output data are averaged to a fixed height output grid spaced
332 with a two-meter resolution until 200 meters above cloud base.

334 **2.32 PARSEC-UFO input data measurements and processing** ~~Measurement data from SMEAR II used for~~ 335 ~~ICPM initialization~~

336 ~~The observational data used for as the ICPMPARSEC-UFO initialization input (Fig. 1) were collected during the~~
337 ~~Biogenic Aerosols—Effects on Clouds and Climate (BAECC) campaign which took place in 2014 at the Station~~
338 ~~Measuring Ecosystem—Atmosphere Relationships (SMEAR) H-II station in Hyytiälä, Finland (Petäjä et al., 2016).~~
339 ~~SMEAR II is a well characterized atmospheric measurement supersite located within a boreal forest in Southern~~
340 ~~Finland (61°51'N, 24°17'E; Hari and Kulmala, 2005). The surroundings of the measurement site are mostly~~
341 ~~forested (80% within a 5 km radius and 65% within a 50 km radius; Williams et al., 2011). The atmospheric~~
342 ~~composition measured at the site suggests strong influence of biogenic emissions on aerosol and aerosol precursor~~
343 ~~(i.e., biogenic VOCs, BVOCs) concentrations (e.g., Hakola et al., 2012; Yan et al., 2016; Allan et al., 2006;~~
344 ~~Heikkinen et al., 2021). Anthropogenic influence is pronounced when air masses arrive from heavily~~
345 ~~industrialized areas such as St Petersburg, Russia (Kulmala et al., 2000).~~

346 As PARSEC-UFO simulations are initialized at 90% RH, which is most of the time higher than that
347 measured at ground level, a ~~an~~ interpolated radiosonde data product from the BAECC campaign (ARM Data
348 Center, 2014) is used to find temperatures matching 90% RH. Radio soundings are performed four times a day
349 (Petäjä et al., 2016). Both the temperature measured near ground level (8.4 m above ground level) and the
350 temperature corresponding to 90% RH are shown in Fig. 1c. While these temperatures show similar temporal
351 behavior at times, also major differences exist, arising e.g., from instable temperature profiles as well as sudden
352 changes in air masses that the interpolated data product built from sondes sent three times a day fails to capture.
353 A well-mixed boundary layer is assumed, and therefore the dry PNSD and aerosol chemical composition are
354 assumed suitable as such for PARSEC-UFO input.

355 The PNSD for the ~~ICPM~~ PARSEC-UFO initialization are obtained from the Differential Mobility
356 Particle Sizer (DMPS) measurements from SMEAR II performed within the forest canopy (Aalto et al., 2001;
357 Petäjä et al., 2016; Fig. 1a). Since ~~ICPM~~ PARSEC-UFO takes in the log-normal parameters that the size
358 distribution comprises (N_i, D_i, σ_i), ~~also~~ the fitting of the PNSD is performed. This is done using the Hussein et
359 al. (2005) algorithm that allows fitting 1–4 modes into the measured distributions and decides the optimal number

360 of modes. For the BAECC data set, the optimal number would always be between three and four modes, with a
361 higher number of modes generally yielding a better fit to the observational data as expected. Despite the optimal
362 number of 3–4 modes, the maximum number of modes is restricted to two as the agreement between the fitted
363 and measured distributions remained good considering the experimental uncertainties (Fig. S.1). ~~and including~~
364 ~~two modes only instead of four considerably sped up the simulations. Moreover, the DMPS is suitable for~~
365 ~~sampling aerosol particles of ca. 3–1000 nm in size (electrical mobility equivalent diameter) and hence does not~~
366 ~~capture the coarse mode. In addition, the Aitken mode at SMEAR II typically originates from a growing nucleation~~
367 ~~mode. In more polluted environments, where small particles have sources other than new particle formation,~~
368 ~~simplifications like this might not be appropriate. The PNSD time series measured during BAECC is shown in~~
369 ~~Fig. 1a. It shows clearly the growth of nucleation mode to Aitken mode on several occasions.~~ Statistics regarding
370 the log-normal parameters of the fitted data during BAECC are provided in Tables 1 and S.1. The bimodal PNSD
371 fits are also calculated for the years 2012–2017. These data are used later to evaluate the frequency of times size
372 distributions yielding high Δ CDNC appear in long-term in-situ data.

373 The aerosol chemical composition for ~~ICPM-PARSEC-UFO~~ initialization are obtained from Aerosol
374 Chemical Speciation Monitor (ACSM; Ng et al., 2011) measurements performed within the forest canopy
375 (Heikkinen et al., 2020). The ACSM measures the non-refractory (NR) sub-micrometer particular matter (PM₁)
376 chemical composition, which means that the reported composition is restricted to organics, sulfate, nitrate,
377 chloride and ammonium. The salts measured by the instrument do not include sea salt, because it typically exists
378 in the coarse mode and does not fully evaporate at the ACSM vaporizer temperature of 600°C. The latter reason
379 restricts the instrument also from detecting black carbon (BC). The composition from the ACSM measurements
380 is shown in Fig. 1b. Statistics regarding the organic mass fractions (f_{org}) are shown in Table 2. The ACSM data
381 are further used to derive volatility distributions similar to those utilized by Topping et al. (2013; see Sect. 2.3.1
382 for details). The volatility distributions derived from ACSM are termed as CJ in the following. The letter
383 combination refers to Cappa and Jimenez (2010), the source of the volatility distribution shapes determined for
384 different OA types. The construction of CJ distributions suitable as PARSEC-UFO input data is explained in Sect.
385 2.3.1.

386 The Filter Inlet for Gases and AEROsols (FIGAERO; Lopez-Hilfiker et al., 2014) coupled with a chemical
387 ionization mass spectrometer (CIMS; the coupling of these instruments hereafter referred to as FIGAERO-I-
388 CIMS), sampling above the forest canopy in a ca. 30 m tower, is used to retrieve molecular composition and
389 volatility distributions of gas- and particle-phase species during BAECC (Mohr et al., 2017, 2019; Schobesberger
390 et al., 2016; Lee et al., 2018, 2020; see Sect. 2.3.2 for details). The FIGAERO-I-CIMS stands as one of the very
391 few instruments capable of performing near-simultaneous measurements of both gas and particle phases. The
392 FIGAERO inlet allows the gas phase to be sampled while aerosol particles are collected on a Teflon filter, and
393 after sufficient particle deposition time the sample is heated and the evaporated molecules are measured similarly
394 to the gas phase. The heating procedure, which typically reaches a maximum temperature of around 200°C can,
395 however, cause thermal fragmentation of molecules (Lopez-Hilfiker et al., 2015). This leads to the detection of
396 small molecular fragments, which get assigned a higher C^* than that of the parent molecule, which can be seen in
397 the FIGAERO-I-CIMS thermograms when compounds with high C^* vaporize at exceptionally high temperatures.
398 In addition to the indistinguishable isomers from any of the phases from online FIGAERO-I-CIMS measurements
399 (or any other mass spectrometer for that matter), thermal fragmentations add to the uncertainty of volatility

distributions retrieved from these data. The derivation of the volatility distributions derived from FIGAERO-I-CIMS data (termed F distributions in the following) is explained in Sect. 2.3.2.

2.3.3.1 Volatility distributions ~~based on from~~ ACSM measurements data (CJ distributions)

Previous to the development of the FIGAERO-I-CIMS, organic volatility distributions were probed only through particle phase measurements (e.g., Huffman et al., 2009b), which enabled volatility constraints of relatively low volatility species (Cappa and Jimenez, 2010). More precisely, these early generation OA volatility distributions were obtained from e.g. Aerosol Mass Spectrometer (AMS; Canagaratna et al., 2007) measurements coupled with a thermal denuder (TD; e.g., Huffman et al., 2009a, b). The TD-AMS measurements provide thermograms (mass fractions remaining in the particle phase as a function of TD temperature of ca. 25–250 °C) that could be assigned to individual OA components i.e., low-volatility oxygenated organic aerosol (LV-OOA), semi-volatile oxygenated organic aerosol (SV-OOA), hydrocarbon-like OA (HOA) and biomass burning OA (BBOA). Cappa and Jimenez (2010) then reproduced such thermograms using a kinetic evaporation model (Cappa, 2010) through fitted OA volatility distributions. In this paper, volatility distributions of this kind are referred to as CJ distributions. ~~It is important to keep in mind that the general CJ volatility distribution shape (i.e., the relative proportions of the volatility bins) is assumed to be of the form $C_{i, \text{tot}} = a_1 + a_2 \exp[a_3(\log_{10} C^* - 3)]$, which was motivated by previous studies on organic aerosol volatility distribution shapes retrieved from chamber experiments (Presto and Donahue, 2006; Robinson et al., 2007), with a_1 , a_2 and a_3 as fitting parameters. Later theoretical work on OA volatility distribution retrievals from TD data states, however, that due to uncertainties associated with the enthalpy of vaporization (ΔH_{vap}), mass accommodation coefficients, and volatility distribution shapes, the attained distributions can be reproduced with several combinations of the three (Karnezzi et al., 2014).~~

To calculate the CJ distributions for the BAEC OA types, the LV-OOA, SV-OOA and primary organic aerosol (POA; taken as a mix of HOA and BBOA) from the SMEAR II ACSM long-term data set are utilized (Heikkinen et al., 2021). During BAEC, the organic aerosol comprised 63% LV-OOA, 32% SV-OOA and only 5% POA on average. Using the time-dependent mass fractions of each OA type, mass-weighted average CJ volatility distributions for each of the model initialization scenarios (97 of them) are calculated. The CJ distribution shapes are taken from Cappa and Jimenez (2010), and they are provided under 298.15 K. The HOA volatility distribution is used for POA (due to the low abundance of levoglucosan in the ACSM mass spectrum; Heikkinen et al., 2021).

~~Topping et al. (2013) utilized the $\log_{10} C^*$ range of [-6, 3] in their simulations and their example is followed in this work.~~ As the CJ volatility distributions have been reported for 298.15 K (Cappa and Jimenez, 2010), and as the ICPM-PARSEC-UFO simulations are generally initialized at different lower temperatures (Fig. 1c), accounting for the impact these temperature changes reduction had on the volatility distributions has on C^* is necessary. The relationship between temperature e , ΔH_{vap} , and C^* is accounted for through an using the Arrhenius-type Clausius-Clapeyron relation (-Eq. 13), where T is the ambient temperature in Kelvin (the ICPMPARSEC-UFO initialization temperature), and T_{ref} is 298.15 K. For the relationship between ΔH_{vap} and $C^*(T_{\text{ref}})$, the formulation provided in Epstein et al. (2010) is used:

$$\Delta H_{\text{vap}} = -11 \log_{10} C^*(T_{\text{ref}}) + 129, \quad (17)$$

where ΔH_{vap} is the change in heat (enthalpy) of vaporization in kJ mol^{-1} . A lower limit of 20 kJ mol^{-1} is set to the ΔH_{vap} , which is close to the ΔH_{vap} determined for formic acid (NIST Chemistry WebBook, 2022). Eq. (17) would otherwise provide too low, unphysical and even negative values. The temperature adjustment (Eq. 13), does not change the shape of the volatility distribution, but the volatility distribution x -axis shifts to the left. See example in Fig. S.2. After the temperature adjustments, the volatility distributions are binned to ranges between $\log_{10} C^* = [-8, 3]$ spaced by one decade in C^* . The lower limit is reduced by two orders of magnitude ($C^*(T_{\text{ref}}) = [-6, 3]$), but the upper limit remains as the initialization temperatures did not exceed T_{ref} . The campaign average CJ volatility distribution is shown with black bars in Fig. 2a. However, each simulation utilizes a unique distribution constructed using the LV-OOA, SV-OOA, and POA time series.

2.3.3.2 Volatility distributions based on from FIGAERO-I-CIMS measurements data (F distributions)

Organic aerosol volatility distributions from FIGAERO-I-CIMS measurements conducted during BAEC (Mohr et al., 2017, 2019; Schobesberger et al., 2016; Lee et al., 2018, 2020) are also derived. It can be assumed that the FIGAERO-I-CIMS detected most of the OA measured with the ACSM. This is, because with the iodide adduct-ization, FIGAERO-I-CIMS is most sensitive to oxidized organic species, such as organic acids (Lutz et al., 2019), and, but not sensitive to non-oxidized hydrocarbons (dominating AMS-derived HOA) and as mentioned in Sect. 2.3.1, most of the observed OA mass (~95%) measured by the ACSM can be. The OA measured with the ACSM comprised on average 95% attributed to oxygenated organic aerosol (LV-OOA + SV-OOA), which is generally thought to represent organic acids (Yatavelli et al., 2015). The agreement between the two measurements is supported by the comparison between the daytime FIGAERO-I-CIMS particle phase signal (of identified ions) and the OA mass concentration retrieved from ACSM measurements provided in Fig. S.13. While the quantification of the FIGAERO-I-CIMS measurements remains challenging and therefore whilst a quantitative comparison between the concentrations is uncertain, the high correlation between measurement data (Pearson $R = 0.79$) proves that the instruments generally sample the same aerosol population. Notably, the ICPM PARSEC-UFO simulations obtain-use OA mass fraction (f_{org}) only from the ACSM measurements. The volatility distributions are derived from FIGAERO-I-CIMS data using molecular formula parameterizations derived under 300 K in Li et al. (2016):

$$\log_{10} C^*(T_{\text{ref}}) = (n_{\text{C}}^0 - n_{\text{C}}) b_{\text{C}} - n_{\text{O}} b_{\text{O}} - 2 \frac{n_{\text{C}} n_{\text{O}}}{(n_{\text{C}} + n_{\text{O}})} b_{\text{CO}} - n_{\text{N}} b_{\text{N}}, \quad (18)$$

where n_{C}^0 is a reference carbon number; b_{C} , b_{O} , and b_{N} are the contributions of each carbon, oxygen, and nitrogen atom to the $\log_{10} C^*$, respectively; b_{CO} is a so-called carbon-oxygen non-ideality parameter (Donahue et al., 2011); n_{C} , n_{O} , and n_{N} are the numbers of carbon, oxygen, and nitrogen atoms in the molecular formulae assigned for the FIGAERO-I-CIMS data during high resolution peak fitting of the measured mass spectra. The b -values utilized are listed in Li et al. (2016). In their recent work, Huang et al. (2021) derived volatility distributions from various organic vapor measurements from SMEAR II. They adjusted the Li et al. (2016) parameterization for organic nitrates. As shown in Isaacman-VanWertz and Aumont (2021), the utilization of the Li et al. (2016) parameterization for OA rich in organic nitrates leads to biased vapor pressure estimates. Organic nitrates are known to form in the boreal air as a result of nitrate radical chemistry, which is pronounced during night, along

476 with daytime oxidation of monoterpenes in the presence of nitric oxide (e.g., Yan et al., 2016; Zhang et al., 2020).
477 To account for these nitrates, Huang et al. (2021) followed the suggestions presented in Daumit et al. (2013) and
478 treated all the nitrate functional groups as hydroxyl ($-\text{OH}$) groups. Given that the focus of this study is on the
479 same measurement site as Huang et al. (2021), their methodology for deriving a volatility distribution from the
480 FIGAERO-I-CIMS is followed here. Once the volatility distributions are constructed using Eq. (18) for 300 K
481 (reference temperature), their adjustments to the parcel model simulation initial temperatures using Eqs. (16–
482 1713) ~~is~~ are performed.

483 The volatilities are calculated for the 1596 ions identified by the FIGAERO-I-CIMS measurements, ~~and~~
484 ~~Afterwards the signals are~~ binned with ~~a one~~ decadal spacing so that all the ~~extremely low volatility organic~~
485 ~~compounds (ELVOC) ELVOC and LVOC are~~ summed into one bin at $C^* = 10^{-4} \mu\text{g m}^{-3}$. ~~This is assumed to be~~
486 ~~appropriate as ELVOCs contain little or no gas phase signals post initialization (See Sect. 2.1.1).~~ The highest
487 volatilities reached $C^* = 10^7 \mu\text{g m}^{-3}$, which is therefore set as the upper limit of the volatility distribution. Following
488 from this, the volatility span is $\log_{10}C^* = [-4, 7]$. The campaign average volatility distribution is shown in red
489 bars in Fig. 2a. The average CJ distribution exhibits generally higher fractions in the ELVOC region as compared
490 to the F distribution (Fig. 2a). This mostly results from the low ~~or~~ non-existent SVOC and IVOC concentrations
491 in the CJ distribution. ~~As the ELVOCs and LVOCs contain little or no gas phase signals post-initialization, the F~~
492 ~~distribution used as input for PARSEC-UFO simulations uses the volatility span of $\log_{10}C^* = [0, 7]$ to speed up~~
493 ~~the simulations.~~

494 The ~~average F distributions~~ shows a remarkable agreement with the organic volatility distributions from
495 the BEACHON-RoMBAS field campaign conducted at the Manitou Experimental Forest Observatory in the
496 Colorado Rocky Mountains in summer 2011 (Hunter et al., 2017, see Fig. 2a). ~~Initially, H~~ Hunter et al. (2017)
497 derived a volatility distribution for the total atmospheric reactive carbon (other than CH_4 , CO_2 and CO) using six
498 different types of measurements and assuming minimal overlap among the measured species. ~~This volatility~~
499 ~~distribution~~ Here, the Hunter et al. (2017) distribution is displayed in Fig. 2a after shifting it to the mean ICPM
500 PARSEC-UFO initialization temperature (280 K) using Eqs. (16–1713) and subtracting ~~non-oxygenated~~ VOC
501 signals from it for comparison. ~~The Hunter et al. (2017) distribution is not used in PARSEC-UFO simulations, it~~
502 ~~is only shown for comparative purposes due to its similarity with the F distributions.~~

503 In Figs. 2b and c, the partitioning coefficients ζ_q (see Eq. 11) from the ICPM PARSEC-UFO initialization
504 (see Sect. 2.1.2) are compared against the partitioning suggested by the FIGAERO-I-CIMS measurements, where
505 the C^* represent the mean PARSEC-UFO initialization temperature and range from $\log_{10}C^* = [-4, 7]$. ~~is compared,~~
506 ~~after accounting for the temperature differences between ground level and ICPM initialization temperatures using~~
507 ~~Eqs. (16–17).~~ The concentrations in volatility bins with $\log_{10}C^* \leq 1$ agree, suggesting that the majority of the
508 organics in these bins are in the particle phase. Similarly, the agreement in the highest volatility bin ($\log_{10}C^* = 7$)
509 suggests the presence of gas-phase compounds only in both distributions. The estimations of the gas phase vary
510 between $\log_{10}C^* = [1, \text{and } 7]$, showing a higher gas-phase fraction for the modelled partitioning coefficients (Fig.
511 2b–d). This variability can result from numerous reasons, which apart from uncertainties related to measurements
512 and parametrizations include viscous particle coatings inhibiting equilibration between gas and particle phases,
513 and therefore showing high particle-phase concentrations of high-volatility compounds in the observations.
514 Alternatively, these concentrations can also result from thermal decomposition of lower volatility products during
515 the FIGAERO-I-CIMS heating process (Lopez-Hilfiker et al., 2015) or from the tendency of the Eq. (18)

parameterization to underestimate [the volatility](#) of organic nitrates (Graham et al., 2022; [despite treating the \$-\text{NO}_2\$ groups at \$-\text{OH}\$ groups](#)), shown to be abundant in the BA ECC FIGAERO-I-CIMS data set (Fig. 2e). Understanding these differences is important and requires further analysis.

The molecular composition of the gas-phase compounds detected by the I-CIMS during BA ECC are analyzed and presented in detail in Lee et al. (2018). In the following, the average composition of each volatility bin during daytime is briefly described. Except for the highest volatility bin, nitrogen-containing species (CHON), which are prominently organic nitrates at SMEAR II (Huang et al., 2021), make up significant mass fractions of each bin in the gas phase (Fig. 2e). Fig. 2f shows the concentration of the gas-phase compounds as a function of the compound carbon and oxygen atom numbers. The figure shows how ELVOCs and LVOCs have the highest numbers of both carbon and oxygen atoms. IVOCs and SVOCs comprise compounds with highly variable carbon skeleton lengths, but the number of oxygen atoms per compound remains low, notably always lowest for IVOCs and VOCs. Formic acid (HCOOH) makes up most of the gas phase signal. It is distributed in the most volatile volatility bin ($C^* = 10^7 \mu\text{g m}^{-3}$). HCOOH is one of the most abundant carboxylic acids in the atmosphere and rain water (e.g., Galloway et al., 1982; Millet et al., 2015 and references therein) and is known to have various sources and precursors (Millet et al., 2015). The I-CIMS measurements discussed here were also performed as part of an eddy covariance flux measurement setup during BA ECC (Schobesberger et al., 2016). These flux measurements provided insight into the high HCOOH concentrations possibly due to high emissions from the boreal forest ecosystem. More details from these results can be found in Schobesberger et al. (2016).

2.45 UK Earth System Model (UKESM1) simulations

To evaluate the frequency of times size distributions yielding high ΔCDNC (which is the percent-change in CDNC due to co-condensation) during BA ECC would become evident over the boreal biome in an ESM if a parameterization of co-condensation was implemented, the United Kingdom Earth System Model (UKESM1, Sellar et al., 2019; Mulcahy et al., 2020) is utilized. The simulations performed with UKESM1 are configured for Atmospheric Model Intercomparison Project (AMIP) style simulations, where UKESM1 is run in its atmosphere-only configuration with time-evolving sea surface temperature and sea ice as well as prescribed marine biogenic emissions from fully coupled model simulations. In addition to the HadGEM3-GC3.1 core physical dynamical model of the atmosphere, land, ocean and sea ice systems (Ridley et al., 2018; Storkey et al., 2018; Walters et al., 2017), UKESM1 also contains additional component models for atmospheric chemistry and ocean and terrestrial biogeochemistry for carbon and nitrogen cycle representation. A N96L85 horizontal resolution structure ($1.875^\circ \times 1.25^\circ$ longitude–latitude, which corresponds roughly a horizontal resolution of 135 km) is chosen for the simulations and the vertical space is split to 85 levels (50 levels between 0 and 18 km and 35 levels between 18 and 85 km). In this study the model is run in a nudged configuration (horizontal wind nudging (but not temperature) between model levels 12 and 80 with a constant 6-hour relaxation time), for the years 2009–2013 inclusively. External forcing and emission datasets are consistent with the Coupled Model Intercomparison Project Phase 6 (CMIP6) implementation as described in Sellar et al. (2020). The simulation setup is same as in the Aerosol Comparisons between Observations and Models (AeroCom) Phase III GCM Trajectory experiment (AeroCom, 2022; Kim et al., 2020).

The UKESM1 aerosol scheme represents the particle size distributions with five log-normal modes: the nucleation soluble mode, Aitken soluble and insoluble modes, accumulation soluble mode, and coarse soluble

556 mode (Mulcahy et al., 2020). The aerosol microphysical processes of new particle formation (NPF), condensation,
557 coagulation, wet scavenging, dry deposition and cloud processing are handled with GLOMAP (Global Model of
558 Aerosol Processes; Mann et al., 2010; Mulcahy et al., 2020). The UKESM1 NPF mechanism follows the
559 parameterization derived in Vehkamäki et al. (2002) for binary homogeneous nucleation of H₂SO₄ and water.
560 Separate boundary layer NPF is not included in the simulations (Mulcahy et al., 2020). The soluble aerosol size
561 distribution lognormal aerosol modal parameters (nucleation mode, soluble Aitken mode and soluble
562 accumulation mode) and sub-grid scale updraft velocities with a 3-hour time resolution at cloud base of stratiform
563 clouds are used. These diagnostics are subsequently masked to include only data in which activated aerosol
564 particles exceeds zero and the temperature exceeds 237.15 K in keeping with criteria used by the droplet activation
565 scheme. The PNSD modal parameters are used to construct aerosol size distributions. In UKESM1 the geometric
566 standard deviations are fixed parameters. The same values are used for consistency for the modes that are
567 accounted for in this work. The geometric standard deviation for UKESM1 Nucleation soluble mode and the
568 Aitken soluble mode is 1.59, and for the accumulation soluble mode it is 1.40. UKESM1 outputs for the Aitken
569 insoluble mode and coarse mode are not used in analysis performed in this study because they do not contribute
570 to CCN in the model representation of cloud droplet activation. UKESM1 uses a 26% SOA yield from
571 monoterpenes, the emissions of which are from The Model of Emissions of Gases and Aerosols from Nature
572 (MEGAN) version 2.1 (Guenther et al., 1995).

573 **3 Results and discussion**

574 **3.1 Organic condensation: time and volatility dependencies**

575 The first ~~cloud parcel model~~ PARSEC-UFO simulation results (Fig. 3) correspond to initializing the model with
576 data collected on May 11, 2014 at 13:37 EET (East European winter time). This simulation is identified from
577 the full dataset as one that represents a strong-median cloud response to co-condensation of organics and water.
578 Figure- 3a shows the vertical evolution of total SVOC and IVOC concentrations in the gas phase for the three
579 different updraft scenarios ($w = 0.1, 0.3, \text{ or } 1 \text{ m s}^{-1}$, respectively). Both SVOC and IVOC concentrations decrease
580 significantly along the adiabatic ascent in subsaturated conditions below cloud base (CB, $\text{RH}_{\text{CB}} = 100\%$). “Below
581 CB” is defined as the ascent from $\text{RH} = 90\%$ upwards as long as $\text{RH} < 100\%$. Given that the PARSEC-UFO
582 simulation output is saved with 2-meter vertical resolution, “below CB” contains all the simulation output under
583 sub-saturated conditions. When moving to saturated conditions,- SVOCs and IVOCs are further scavenged inside
584 the cloud in saturated conditions. This result is in line with Bardakov et al. (2020), who modelled complete gas
585 removal of volatility bins up to roughly $\log_{10}C^* = 9$ within convective clouds.

586 When considering all 97 simulations, the net mass fractions of organics condensed below CB are on
587 average 91, 702 and 2835% for the 0.1, 0.3 and 1.0 m s^{-1} updraft, respectively, which in absolute concentrations
588 means additions of 1.8, 1.4, and 0.7 $\mu\text{g m}^{-3}$ to the aerosol particle soluble mass (Table 2). The yielded mass
589 concentrations are in the same order of magnitude as the PM₁ mass concentrations measured during BAEC
590 (interquartile range, IQR: 0.95, 1.95, and 3.22 $\mu\text{g m}^{-3}$ from ACSM data), which means that such organic
591 condensation along the adiabatic ascents as simulated here would yield roughly a doubling of the soluble mass
592 due to SVOC and IVOC condensation below CB. Figures 4d-f show the simulated organic condensate
593 concentrations for each volatility bin. While the condensed fraction for the highest volatility bin is smallest (Figs.
594 4a-c), the absolute concentrations of condensate are amongst the largest due to the high availability of organic

595 vapor in the highest volatility bin (mostly HCOOH; Sect. 2.3.2). The condensation efficiency of the highest
596 volatility bin correlates with the number of large particles serving as condensation sink for vapors (Fig. S.4). This
597 suggests that these organic vapors are likely to condense onto larger particles, which are susceptible to be activated
598 into cloud droplets regardless of co-condensation. Similar correlations are observed to a lesser extent with the
599 $\log_{10}C^* = 6$ volatility bin (not shown). In this work, the information of the size ranges of particles which the high-
600 volatility IVOCs condense onto is lacking. Therefore, more systematic studies should be conducted to better
601 understand whether the condensation of the high-volatility IVOCs onto ultrafine particles is sufficient enough to
602 lead to increased droplet activation.

603 The exact numbers presented here should, however, be assessed with caution as an ideal liquid phase, as
604 well as partitioning being determined by mole fractions of water-soluble organics are assumed ~~in this work~~ (Sect.
605 2.1.1). Topping et al. (2013) looked into the assumption of ideality in their supplementary material. They found
606 it to enhance the amount of modelled organic condensate as compared to a non-ideal case. However, their
607 simulations exploring non-ideality with organic activity coefficients predicted with the UNIFAC method
608 (UNIQUAC Functional-group Activity Coefficients; Fredenslund et al., 1975) ~~or solubilities~~ still led to significant
609 amounts of condensed organic mass. The impact of the ideality assumption was shown to be most significant in
610 their highest volatility bin ($C^* = 1000 \mu\text{g m}^{-3}$). Activity coefficients (and solubilities) of organics should in the
611 future be better constrained to assess the impact on volatility bins of $\log_{10}C^* > 3$, which was not explored in
612 Topping et al. (2013). As discussed in the Topping et al. (2013) supplementary information, it is likely that
613 solubility decreases towards the higher volatility bins. Here, a simple assessment of the assumption of ideality
614 (Appendix A, Fig. A.2b) suggests that the gained organic soluble mass reduces only when the overall mass
615 accommodation coefficient for organics is less than 0.4. This would mean that the organic condensation shown
616 here could be taken as the upper limit.

617 Further investigation on how efficiently different volatility bins condensed along the adiabatic ascents
618 across all the 97 simulation scenarios repeated with the three fixed updraft velocities is also performed (Fig. 4a-
619 c). In the 0.1 m s^{-1} updraft scenario, almost all organic vapor condenses up to $\log_{10}C^* = 5$ and the condensation
620 capability of the highest volatility bin ($\log_{10}C^* = 7$) shows the highest variability (~~27–91%~~ ~20–91% condensed
621 below CB; Fig. 4a). The same features can be observed with the 0.3 m s^{-1} and 1.0 m s^{-1} updraft simulations,
622 although the fraction of organic vapor condensed per volatility bin is reduced (in the $w = 1 \text{ m s}^{-1}$ scenarios only
623 ca. ~~40%~~ 30% of the vapor condenses below CB (Figs. 4b–c). The results from these simulations reveal that there
624 is enough time only under slow adiabatic ascents for most of the organic vapor to condense.

625 ~~As the results from Figure 4 underline the time dependence of co-condensation, it is worth remembering~~
626 ~~that the ICPM initialization RH is set to 90% (see Sect. 2.4). If the initial RH was set to a lower value, more time~~
627 ~~would be available for co-condensation before reaching CB, and if the initial RH was set to a higher value, less~~
628 ~~time would be available. While the decision of maintaining a fixed initial RH for the different simulations is~~
629 ~~proven useful for this study as it eases the data interpretation process, it should be acknowledged that the initial~~
630 ~~RH could be better constrained in future simulations.~~

631

3.2 Impact of updraft velocity meteorological conditions on the sensitivity of cloud microphysics to organic vapor condensation

As explained previously in Topping et al. (2013), the CDNC enhancements associated with co-condensation arise from the enhancement-increase in organic solute concentration, which decreases the critical supersaturation (s^*) needed for a given particle to activate. The s^* reductions from 0.15% to 0.10% is reduced about 10–20% for the May 11, 2014 at 13:11:30–37 EET case presented in Fig. 3b when co-condensation is enabled. are shown in Fig. 3b, and correspond This reduction is calculated for to a particle with a dry radius of 71.9 nm (i.e., the smallest activated dry radius when co-condensation is disabled, r_{noCC}^* and $w = 0.1 \text{ m s}^{-1}$; Table 2). Fig. S.52 shows the development of the wet particle size as a function of altitude in the ICPM-PARSEC-UFO simulation summarized in Fig. 3. It clearly demonstrates the differ differences introduced by co-condensation through the activation of new size bins (4 size bins in total when $w = 0.1 \text{ m s}^{-1}$) that would have remained as interstitial aerosol particles in the simulations , where co-condensation is turned off. The enhanced growth of more particles due to co-condensation enhances the water vapor condensation sink, which leads to a reduction in the achieved maximum ambient supersaturations (s_{max} ; see Fig. 3c for the May 11 case and Table 2 summarizing all the 97 simulations). As the updraft meteorological conditions are is the same in simulations performed with and without co-condensation, the condensation sink dictates the changes in s_{max} (Eq. 3). A reduced s_{max} would typically lower the number of aerosol particles activating into cloud droplets, but here the suppressions-reductions in s^* are greater than the reductions in s_{max} , which therefore leads to an enhanced CDNC (see Fig. 3b–c for the May 11 case). This can be interpreted as a competition effect between the s_{max} and s^* reductions, respectively, which the s^* reduction wins. When examining the 0.1 m s^{-1} updraft case in the May 11th simulation shown in Fig. 3, the s_{max} is reduced ~7% 12.5% (from 0.16% to 0.14%), which is less significant than the s^* reduction of about 33–20% (from 0.15% to 0.10%; Fig. 3b). This leads to a 22% enhancement in CDNC (Fig. 3d) as r^* reduces from 72 nm to 66 nm ($\Delta r^* \approx 6 \text{ nm}$). Fig. 3e finally shows the droplet spectrum for the May 11 case, which highlights the consistent shift of droplet sizes to smaller diameters due to organic co-condensation (see also Fig. S.25, which displays the same May 11th simulation with $w = 0.1 \text{ m s}^{-1}$). The impact such shift could have on cloud lifetime and precipitation should be studied further.

The modelled BAECC campaign median CDNC values (over the 97 simulations) without co-condensation are on average 161, 300 and 530 cm^{-3} in modeling scenarios utilizing 0.1 m s^{-1} , 0.3 m s^{-1} , and 1.0 m s^{-1} updrafts, respectively (Table 2). CDNC is shown to correlate well with the accumulation mode number concentration (N_2), and at times with the Aitken mode number concentration (N_1) if the Aitken mode particles are large enough in size and accompanied with strong enough updrafts and a low N_2 (Fig. S.36). The reductions in the smallest activated critical dy radii due to co-condensation ($r_{\text{noCC}}^* - r_{\text{CC}}^*$) are on average 8.2, 6.6, and 5.9 nm ~8, ~7, and ~5 nm for the modeling scenarios utilizing 0.1 m s^{-1} , 0.3 m s^{-1} , and 1.0 m s^{-1} updrafts, respectively, and the corresponding median ΔCDNC are 16.8, 23.3 and 20.6%, ~16, ~23 and ~19%, respectively (Table 2 and Fig. 5a). The swarm plot on Fig. 5a shows that ΔCDNC and CDNC do not correlate i.e., low CDNC in the noCC runs high ΔCDNC does not favor susceptibility is in this case not predicted specifically for low CDNC high ΔCDNC .

On average during the BAECC simulation period (97 simulations), the highest ΔCDNC are found when initializing the model with a 0.3 m s^{-1} updraft velocity (also visible in Fig. 3d for the May 11 case) followed by ΔCDNC predictions for the 1 m s^{-1} case. In the latter, high supersaturations are achieved leading to the formation of many cloud droplets, yet the effects of co-condensation remained less pronounced as the high ascent speed

672 poses kinetic limitations for organic condensation (see Sect. 3.1 and Fig. 4). Despite the highest organic uptake in
673 the 0.1 m s^{-1} updraft simulations (Fig. 4a, d), the ΔCDNC remains the lowest. This can be explained by the low
674 s_{max} , which remains insufficient ~~for the activation of to activate~~ small particles ~~to cloud droplets~~ ($-r_{\text{noCC}}^*$ ~~and kept~~
675 ~~the smallest activated dry diameter on average at 63.7 nm ~64 nm;~~ (Table 2). As the Aitken mode possesses most
676 particles in terms of number (Table 1), the few nm reductions in r^* affect ΔCDNC the most when ~~the r^* reduction~~
677 ~~taking place at on~~ the steep PNSD slopes (high dN/dD) between the Aitken and accumulation mode. ~~When the~~
678 ~~updraft velocity is low (0.1 m s^{-1}), ~~which the r^* are too large does~~ to overlap with the parts of the PNSD with a~~
679 ~~high dN/dD even if r^* reduces greatly due to co-condensation. not happen in the simulations performed with 0.1~~
680 ~~m s^{-1} updraft. Due to the high updraft-dependency of the modelled ΔCDNC , future process modeling work should~~
681 ~~consider performing simulations following updraft probability density functions (PDF), as used in GCMs, and~~
682 ~~calculating PDF weighted CDNC (West et al., 2014). This way more weight will be given to lower updrafts, and~~
683 ~~the model outputs will be more robust since the air parcels do not experience single updrafts in reality.~~

684 Besides updraft velocity, the modeled ΔCDNC are also affected by PARSEC-UFO initialization
685 temperatures. This can be seen when the effect of the volatility distribution upgrade (from CJ to F) on the modelled
686 ΔCDNC is investigated. For this purpose, an additional set of PARSEC-UFO simulations using the CJ volatility
687 distribution are performed. Perhaps surprisingly, the CDNC enhancements due to co-condensation attained with
688 the CJ volatility distribution are negligible (median ΔCDNC is 0; Fig. S.7) and therefore strikingly different from
689 those presented in Topping et al. (2013). The large difference in the modeled ΔCDNC between the F and CJ
690 simulations arises from the low amount of organic vapor available for condensation ($\sum C_g^{\text{INIT}}$ is only $0.10 \mu\text{g m}^{-3}$
691 in CJ simulations while in the F simulations it is $2.05 \mu\text{g m}^{-3}$), which in turn results from the low PARSEC-UFO
692 initialization temperature attained from the radio soundings (Sect. 2.3). If the initialization temperatures were
693 higher, more organic vapor would remain in the gas phase after PARSEC-UFO initialization, and larger ΔCDNC
694 could be modeled. The simulations performed in Topping et al. (2013) were initialized at 298 K, which explains
695 why they report significant CDNC enhancements due to co-condensation using a similar CJ volatility distribution
696 as used here. We can reproduce the Topping et al. (2013) findings when increasing the initialization temperature
697 with PARSEC-UFO (see Fig. S.8) and also demonstrate that by decreasing the initialization temperature from 298
698 to 280 K (the BAEC median temperature), the ΔCDNC modeled by Topping et al. (2013) should also be
699 negligible (Fig. S.8). These findings emphasize the critical role of the initialization temperature (and assumptions
700 made on equilibrium upon model initialization) that impacts the amount of organic vapor present in the gas phase
701 prior to the air parcel's ascent. Additionally, the result suggests high importance of organic vapors with saturation
702 vapor concentrations exceeding $\log_{10}C^* = 3$ (under 298 K) for co-condensation. If one were to utilize CJ
703 distributions in future co-condensation work, one could consider multiplying the highest volatility bins e.g., with
704 a carefully selected constant. Similar approaches have been used previously when modeling SOA formation from
705 IVOCs (Lu et al., 2018).

706 An additional set of simulations using the CJ volatility distribution with the 0.3 m s^{-1} updraft velocity are
707 performed to assess the comparability of our simulations to Topping et al. (2013) and to evaluate the impact of
708 the volatility distribution upgrade from CJ to F. (Lu et al., 2018) As the results from Fig. 4 underline the time-
709 dependence of co-condensation (Sect. 3.1), it is worth remembering that the PARSEC-UFO initialization RH is
710 set to 90% where equilibrium conditions are assumed (see Sects. 2.4 and 2.2). Therefore, the kinetic effects play
711 a role only from 90% to 100% RH. Importantly, if the initial RH was set to a lower value, more time would be

712 available for co-condensation before reaching CB, and if the initial RH was set to a higher value, less time would
713 be available. On the other hand, due to the assumption of initial equilibrium conditions, a lower initial RH also
714 ensures a higher organic vapor concentration available for co-condensation, and a higher initial RH reduces the
715 organic vapor availability. Together with initial temperature, the initial RH strongly control the amount of organic
716 vapor available for co-condensation (Appendix A, Fig. A.1, Fig. S.3) and thereby the amount of soluble organic
717 mass yielded by the time the air parcel reaches cloud base. While the decision of maintaining a fixed initial RH
718 for the different simulations is proven useful for this study as it eases the data interpretation process, it should be
719 acknowledged that the initial RH could be better constrained in future simulations. Naturally, the organic vapor
720 condensation depends on the initial RH, and as a result Δ CDNC is also sensitive to the selection of the initial RH
721 (Fig. A.1). If the initial RH is set to 60%, CDNC enhancements as high as ~100% could be expected, while if the
722 initial RH is set to 99% the enhancements are expected to range between 0 and ~20%. This variation is greater
723 than the impact the ideality assumption (or the selection of vaporization enthalpy) has on Δ CDNC (Sect. 3.1,
724 Appendix A).

725 Results from these simulations are summarized in Table 2, but also visualized in black in Figs. 3 and 5a.
726 The Δ CDNC predicted in the simulations using CJ volatility distributions are lower (Δ CDNC = 12.4%) than those
727 predicted using the F distribution, but fall within the variability reported in Topping et al. (2013; Δ CDNC of ~5–
728 55%). The difference between the simulations performed with CJ and F volatility distributions, respectively, can
729 be explained by the lower organic vapor concentration in the CJ distribution at model initialization, leading to a
730 lower amount of soluble mass at CB (Table 2; Fig. S.4). This result highlights that significant quantities of co-
731 condensable organic vapors are distributed in the higher volatility bins and these concentrations should not be
732 neglected in further co-condensation studies.

734 3.3 Impact of initial aerosol size distribution and organic vapor concentration on the sensitivity of CDNC 735 to organic vapor condensation

736 As briefly mentioned in the previous section, PNSD affects Δ CDNC along with the initial meteorological
737 conditions. The importance of Aitken mode in Δ CDNC associated with turning co-condensation on in ~~ICPM~~
738 ~~PARSEC-UFO~~ is exemplified in Fig. 5b for the 0.3 m s⁻¹ updraft simulations. In this figure, the initial dry PNSD
739 are averaged from the simulations with the highest ~~50%–25%~~ and lowest 50% modelled Δ CDNC, respectively.
740 The PNSD corresponding to the highest ~~50%–25%~~ of the modelled Δ CDNC has a very minor accumulation mode
741 and a large Aitken mode (with respect to the mode total number concentrations i.e., N_2 and N_1 , respectively) with
742 a diameter (D_1) of ~40 nm (D_2 is ~110 nm). It is ~~therefore~~ named as PNSD_{NUM}, where NUM refers to a strong
743 nascent ultrafine mode characteristic of the shown size distribution. The PNSD corresponding to the lowest 50%
744 of the modelled Δ CDNC is strongly bimodal, where the Aitken and accumulation modes are almost equal in terms
745 of N . Moreover, the two modes are separated by a clear Hoppel minimum (Hoppel and Frick, 1990). Hoppel
746 minimum is characteristic for ~~particulate matter aerosol populations~~, which have undergone cloud processing.
747 This result underlines that environments rich in particles from a local source would be more susceptible to high
748 Δ CDNC due to co-condensation while regions with aged and cloud processed size distributions are affected less
749 (Δ CDNC < 20% in our simulations; Fig. 5a).

751 Interestingly, a nascent ultrafine aerosol particle mode (NUM) was found to be important when looking
752 into suitable conditions for large increase in CDNC caused by surface active organics (~~Lowe et al., 2019;~~

753 Ovadnevaite et al., 2017; [Lowe et al., 2019](#)). Lowe et al. (2019) utilized ~~the same a similar~~ CPM ([ICPM, Sect. 2.1](#))
754 as used in this study (notably without co-condensation), but enabled a fraction of the particulate organics to form
755 a thin, max. 0.2 nm thick film around the particle. The film was characterized by a surface tension of 40 mN m⁻¹
756 as opposed to the surface tension of pure water (72.8 mN m⁻¹). The idea of this compressed film (CF) approach
757 was to simulate the surface tension reductions caused by organic species leading to the activation of smaller
758 particles to cloud droplets at the coastal Mace Head site (Ovadnevaite et al., 2017). Through sensitivity studies,
759 Lowe et al. (2019) found that the largest percent change in CDNC due to surface active organics (>10%) took
760 place in Mace Head when $N_2 < aN_1^b + c$ ($a = 602$, $b = 0.0884$, $c = -766$). The increase in CDNC in the Lowe et al.
761 (2019) study was also attributed to the reduction in s_e^* when comparing against simulations where the surface
762 tension was that of water. Moreover, the same competition effect between s_{max} and s_e^* reductions – as described
763 here in Sect. 3.2 – was demonstrated in their study, but just triggered by different chemical parameters. The
764 sensitivity of the CDNC enhancements to PNSD_{NUM} in this study as well as in Lowe et al. (2019) demonstrates
765 that the activation of fresh and non-cloud-processed aerosol particles is susceptible to small reductions in s_e^* that
766 can be triggered e.g., by organic surfactants or co-condensation. Importantly, potential surface activity also affects
767 the CCN activation behavior of atmospheric organics (Ruehl et al., 2012, 2016; Lowe et al., 2019), correlating
768 with volatility and solubility. The combined effect of all these three properties needs to be thoroughly investigated,
769 ~~because of the potential of the organic film to suppress the solute effect (Sorjamaa et al., 2004) and thereby co-~~
770 ~~condensation and its effects on Δ CDNC, in the future.~~

771 In conjunction with the Δ CDNC susceptibility to PNSD_{NUM}, this study most critically highlights the
772 importance of incorporating multimodal, and representative size distributions in process modeling studies
773 examining the cloud response to ~~surface active organics, or~~ co-condensation ~~(or surface-active organics as~~
774 ~~demonstrated in Lowe et al., 2019)~~. Topping et al. (2013), for example, used monomodal distributions (with
775 varying log-normal parameters) in their study, which could lead to overestimation of Δ CDNC as size distributions
776 with Hoppel minima are not explored. Multimodal distributions were used later by Crooks et al. (2018), but further
777 explanation of the cloud response of the update remained lacking. In summary, our results [together with the Lowe](#)
778 [et al. \(2019\) results](#) suggest that in clean environments with a local source of ultrafine particles, such as the boreal
779 forest or marine environments, organic species in the presence of a NUM-featured PNSD can have significant
780 impact on cloud properties either via co-condensation or through surface tension reductions.

781 Subsequently, a dry PNSD-based criteria for identifying regimes (conditions) in which co-condensation
782 has the highest impact on CDNC are defined. It is found that restricting the ratio between the accumulation and
783 Aitken mode geometric mean diameters in the initial dry PNSD to below six (i.e., $D_2/D_1 < 6$) and the Aitken mode
784 number concentration to exceed 1000 cm⁻³ (i.e., $N_1 > 1000$ cm⁻³) would yield Δ CDNC >20% in our simulations
785 [\(Fig. 5d\)](#). By using the diameter ratio criterion, size distributions without a distinguishable Hoppel minimum are
786 selected, which is characteristic in the simulations yielding the highest Δ CDNC (Fig. 5b) and the high N_1 ensures
787 a high concentration of aerosol particles potentially activating into cloud droplets. ~~Fig. 5d shows the Δ CDNC as~~
788 ~~a function of D_2/D_1 , N_1 and the Pearson correlation coefficient with PNSD_{NUM} (0.3 m s⁻¹ updraft case). The~~
789 ~~simulations with the initial dry PNSD fulfilling the criteria are highlighted with white crosses. Most of the high~~
790 ~~Δ CDNC are well captured, and at those times the correlation with the PNSD_{NUM} is high (Pearson $R > 0.7$). The~~
791 ~~simulations fulfilling the dry PNSD based criteria are marked also in Fig. 5e showing that most of the high~~

~~ACDNC are captured, which again highlights the critical role of the aerosol size distribution representation in capturing the co-condensation driven ACDNC.~~

In addition to the PNSD_{NUM} features, also the initial organic vapor concentration (C_g^{INIT}) influences the modeled ΔCDNC . ~~This relationship extent to which the modeled ΔCDNC are sensitive to C_g^{INIT} is depicted in Fig. 5c using the ICPM-PARSEC-UFO simulations performed with corresponding to 0.3 m s⁻¹ updrafts. The y-axis represents the modeled ΔCDNC and the x-axis the organic vapor concentration distributed in log₁₀ C^* bins within [-4, 4] (denoted as $C_{g,-4:4}^{\text{INIT}}$) i.e., in bins that do not show high dependency on N_2 or initial temperature the available surface area (see Sect. 3.2 and Fig. S.4 for details). The relationship is not straightforward, but linear increases in ΔCDNC as a function of $C_{g,-4:4}^{\text{INIT}}$ can be seen under constant, yet sufficiently high s_{max} (here >0.2%). Under the modelled scenarios, where $s_{\text{max}} > 0.2\%$, the $C_{g,-4:4}^{\text{INIT}}$ remains is generally low ($\leq 2 \mu\text{g m}^{-3}$); and still, the highest CDNC enhancements during the BAEEC simulation period are achieved when $C_{g,-4:4}^{\text{INIT}}$ is $\leq 1 \mu\text{g m}^{-3}$. The high CDNC enhancements can be achieved – despite the low organic vapor abundance – simply because the soluble organic mass is distributed to more smaller particles. The markers in Fig. 5c are color-coded by the initial PNSD surface area, which under a constant updraft anticorrelates with s_{max} (see Eq. 3). ΔCDNC shows high sensitivity to $C_{g,-4:4}^{\text{INIT}}$ when the dry PNSD surface area stays below a $100 \mu\text{m}^2 \text{cm}^{-3}$ threshold. Based on this analysis, it can be concluded that in the presence of a NUM-featured PNSD enabling the formation of high supersaturations (the dry PNSD surface area stays below $100 \mu\text{m}^2 \text{cm}^{-3}$), an adiabatic ascent with an updraft of 0.1 or 0.3 m s⁻¹ can yield ΔCDNC of >40% if $1 \mu\text{g m}^{-3}$ of co-condensable organic vapor is present in the rising air. This is a likely occurrence in the spring and summertime boreal forest (Huang et al., 2021). However, it should be noted that under such scenarios the modeled ΔCDNC are highly sensitive to organic vapor concentration (Fig. 5c) and a reduction of $\sim 0.5 \mu\text{g m}^{-3}$ in organic vapor concentration can half the modeled CDNC when the PNSD surface area is low. The simulations performed with the highest updraft velocity ($w = 1.0 \text{ m s}^{-1}$) yield lower ΔCDNC under these clean conditions (ΔCDNC does not exceed 40%) even though the simulated s_{max} increase as opposed to the results obtained with lower updrafts (e.g., Table 2), because of the kinetic limitations hindering co-condensation (see Sect. 3.1).~~

3.4 Expected seasonality in the impact of co-condensation on CDNC at SMEAR II

In the following, the seasonality of the dry PNSD surface area at SMEAR II (6-year-long time series, 2012–2017) is investigated to estimate how often it stays below the previously mentioned threshold of $100 \mu\text{m}^2 \text{cm}^{-3}$ i.e., times when only $1 \mu\text{g m}^{-3}$ of co-condensable organic vapor present in the rising air could yield significant ΔCDNC . This is followed by an investigation of the frequency of the PNSD criteria ($D_2/D_1 < 6$ and $N_1 > 1000 \text{ cm}^{-3}$) fulfillments in the long-term size distribution measurements at SMEAR II.

Fig. 6a shows the seasonality of the dry surface area at SMEAR II. During daytime (9–19 EET) the surface area stays below the previously mentioned threshold 86% of the time during the 2012–2017 measurement period (Fig. S.59), which suggests that under 0.3 m s⁻¹ updraft velocities, generation of $s_{\text{max}} > 0.2\%$ at this site is likely. During summer months, the likelihood of surpassing the dry PNSD surface area threshold of $100 \mu\text{m}^2 \text{cm}^{-3}$ increases ~~to 22%~~ from 10% to 22% (Fig. S.95) due to biogenic SOA formation (e.g., Tunved et al., 2006; Heikkinen et al., 2020), which grows the accumulation mode in the PNSD. Biogenic SOA formation depends on the SOA precursor i.e., BVOC emissions and concentrations. Monoterpene concentrations are highest at SMEAR

831 II in summer (Kontkanen et al., 2016; Hakola et al., 2012) as their emissions are strongly temperature-driven
832 (Guenther et al., 1993). The organic vapor concentration available for co-condensation is therefore also highest in
833 summer, but due to the enhanced surface area, the soluble organic mass is distributed to ~~more~~-larger particles
834 dampening the cloud response to co-condensation. However, the monoterpene emission period is longer than just
835 summer, and elevated monoterpene concentrations can be observed throughout the thermal growing season (when
836 the daily average temperature is above 5°C; Kontkanen et al., 2016; Hakola et al., 2012). Therefore, monoterpene
837 emissions take place also at times when the dry PNSD surface area stays below the 100 $\mu\text{m}^2 \text{cm}^{-3}$ threshold.

838 Fig. 6b shows the dry PNSD surface area derived from the long-term PNSD measurements at SMEAR
839 II as a function of temperature. When the ambient temperature exceeds 5°C, the dry PNSD surface area starts to
840 increase with increasing temperature. The dry PNSD surface areas and ambient temperatures (from 8.4 m height;
841 Fig. 1c) from the BAECC simulation period are also shown to highlight the fact that the BAECC sample represents
842 well the long-term statistics of the thermal growing season, providing confidence in the representativity of the
843 BAECC sampling period for this boreal environment. The BAECC samples are color-coded by the modelled
844 ΔCDNC . The highest ΔCDNC (i.e., $\Delta\text{CDNC} > 40\%$) are modeled when the dry PNSD surface areas are below
845 the 100 $\mu\text{m}^2 \text{cm}^{-3}$ threshold. Importantly, most of these model scenarios yielding $\Delta\text{CDNC} > 40\%$ coincide with
846 ambient temperatures between 5 and 8°C i.e., at times when the monoterpene concentrations are not at their
847 highest yet sufficient concentrations of organic vapor are still present to cause a large cloud response. It can
848 thereby be concluded that the highest ΔCDNC due to co-condensation can be expected in thermal Spring and Fall.
849 However, due to the seasonality in hygroscopicity and the slightly higher κ in spring and autumn (as opposed to
850 summer; Fig. 6a) the likelihoods of obtaining S_{max} exceeding 0.2% to yield significant ΔCDNC can be somewhat
851 buffered due to hygroscopic growth.

852 Next, the frequency to which the PNSD criteria ($D_2/D_1 < 6$ and $N_1 > 1000 \text{ cm}^{-3}$) are fulfilled in the long-
853 term size distribution measurements is examined. For this purpose, the same 6-year PNSD data set collected at
854 SMEAR II fitted with two log-normal size distributions (Hussein et al., 2005) is utilized. The percentage of times
855 the criteria are met is shown in Fig. 7a. The highest frequencies (30–40% of the time) are observed in April, May
856 and September, which correlates with ~~the a high~~ new particle formation (NPF) frequency at the site (Nieminen et
857 al., 2014; Dada et al., 2017). The monthly median size distributions fulfilling the criteria are shown in Fig. 7c.
858 They all clearly exhibit the lack of a Hoppel minimum, similarly to PNSD_{NUM} , and suggest a potentially high
859 impact of newly formed particles on cloud properties through co-condensation. However, future work should
860 focus on understanding how frequently the measured PNSD_{NUM} are actually exposed to droplet activation, which
861 would help us assess the likelihood of large CDNC enhancements taking place in reality. This is particularly
862 important, because NPF typically takes place in sunny, non-cloudy days, which provides time for the PNSD_{NUM}
863 to evolve before exposed to cloud base and subsequent droplet activation. The results again clearly emphasize the
864 need of accurate representation of aerosol size distributions and lifecycle in models (such as other CPMs or global
865 circulation models, GCMs) to account for the impacts of co-condensation and the strong seasonality to be expected
866 in the magnitudes in ΔCDNC .

867

868 3.5 Expected spatiotemporal variability in the impact of co-condensation on CDNC over the boreal biome

869

870 In this section the SMEAR II results are compared against a 5-year UKESM1 simulation (see Sect. 2.45; analysis
871 restricted to the boreal biome). While the SMEAR II PNSD data are retrieved at ground level, utilization of the

872 UKESM1 modal parameters (only soluble modes considered) from CB is chosen, because these PNSD log-normal
873 parameters would actually meet the cloud droplet activation scheme in the model. [Previous co-condensation](#)
874 [parameterization schemes have also been developed to treat the CB PNSD to account for co-condensation](#)
875 (Connolly et al., 2014; Crooks et al., 2018). The monthly averages of the percentage of times the criteria ($D_2/D_1 < 6$
876 and $N_1 > 1000 \text{ cm}^{-3}$) are fulfilled in the boreal grids are shown in Fig. 7b. Here, the Aitken mode geometric mean
877 diameter and total number concentration (D_1 , N_1) and accumulation mode geometric mean diameter (D_2) are
878 obtained from the soluble Aitken and accumulation modal parameters (see Sect. 2.45 for more details regarding
879 the UKESM1 modes). The frequencies, which remain roughly well below 6%, are in general much lower than
880 observed at SMEAR II. This can be explained by the lack of the boundary layer NPF process in the UKESM1
881 simulations (Sect 2.45). Therefore, the UKESM1 results can be taken as the lower estimate. Fig. 7d displays the
882 monthly median PNSD in the boreal grid cells fulfilling the criteria ($D_2/D_1 < 6$ and $N_1 > 1000 \text{ cm}^{-3}$), which are
883 constructed from the soluble Nucleation, soluble Aitken and soluble accumulation mode modal parameters from
884 the UKESM1 simulations when the criteria are fulfilled (criteria only uses soluble Aitken and soluble
885 accumulation modes). The size distributions calculated using these UKESM1 modal parameters are in general
886 less similar to the PNSD_{NUM} than the monthly median SMEAR II size distributions are (Fig. 7c), because they
887 have more distinguished multimodal shapes, [which arises from the modal representation of the PNSD](#). However,
888 they still feature a minor accumulation mode in the presence of a large Aitken mode (with respect to N).

889 The UKESM1 results suggest [that a](#) strong spatiotemporal variability in the co-condensation driven
890 ΔCDNC should be expected if this process were to be represented in GCMs. Consistently with the SMEAR II
891 observations (Fig. 7a), spring months stand out as the times when the criteria are most likely to be met, but the
892 other peak in the frequency, expected in September at SMEAR II, cannot be seen. Another interesting feature is
893 the large spatial variability in the frequency. In March and April, a very evident hotspot can be seen in the southern
894 parts of the boreal forest, more precisely in the north of Kazakhstan. When the whole northern hemisphere is
895 displayed, it is clear that the hot spot region extends over Europe during Spring (Fig. S.106) when the conditions
896 favor the formation, growth and survival of small particles (Kerminen et al., 2018) as shown in Fig. S.117 in terms
897 of nucleation mode number concentration. The result therefore suggests high co-condensation potential in areas
898 rich in ultrafine particles. The cloud response of co-condensation in an extended domain covering most of Eurasia
899 could be an interesting follow-up study. However, such a study should incorporate also the condensation of nitric
900 acid and ammonia, the concentrations of which are presumably abundant in the regions, where the co-
901 condensation PNSD criteria are met (Kakavas et al., 2022). As this “Kazakhstan hotspot” is connected to aerosol
902 phenomenology outside the boreal biome, the analysis is not continued further. Another evident springtime hot
903 spot is located in North America, near the Rocky Mountains, but the updraft velocities at the area are not within
904 the desired range ($[0.2, 0.5] \text{ m s}^{-1}$) to yield significant cloud response from co-condensation (Fig. 7b).

905 Aside from these hotspots, it is notable that the overall background of the frequency of the times the
906 criteria are met in the latitude range of $[0, 75]^\circ\text{E}$ increases from $<2\%$ to $2\text{--}6\%$ when moving from March to April.
907 This background stays elevated until June. Smaller hotspots within this area are visible and they correspond to
908 regions known with high sulfur dioxide (SO_2) emissions, such as the Kola peninsula. The Kola peninsula SO_2
909 emissions have shown to trigger NPF events measured at SMEAR I in Finnish Eastern Lapland (e.g., Kyrö et al.,
910 2014). An interesting next step would be to see how Fig. 7b changes with UKESM1 simulations incorporating
911 boundary layer NPF and whether the percentage of times the criteria are met increases to values comparable with

912 the SMEAR II observations and whether the frequency becomes larger also in Fall. Another interesting
913 observation to be made from Fig. 7b is that no significant impact of co-condensation would be expected in
914 UKESM1 in most of Siberia (East and Northeastern Siberia), which can be explained by the lack of nucleation
915 mode particles in the UKESM1 simulations over the region (Fig. S.127).

916 4 Conclusions

917
918 This study focuses on the role of the co-condensation of organic vapor and water on warm cloud microphysics in
919 a boreal forest environment. Co-condensation has been proposed as a potentially significant process contributing
920 to the feedbacks between VOC emissions, SOA loadings, cloud formation and climate. Boreal forests account for
921 about a third of the Earth's forested area and are potentially significant sources of such co-condensing species.

922 First, ICPM-PARSEC-UFO model is used to perform simulations for the BA ECC measurement
923 campaign which took place at the SMEAR II station in Southern Finland during 2014 (Petäjä et al., 2016). The
924 measurement setup during BA ECC was very advanced, enabling the initialization of ICPM-PARSEC-UFO with
925 state-of-the art data describing the ambient aerosol physical and chemical properties. The measurements
926 conducted with the FIGAERO-I-CIMS (e.g., Mohr et al., 2017) are of high importance for this study due to the
927 simultaneous measurements of organic particle and vapor species. These data enable the incorporation of organic
928 vapors from a broad volatility range into the ICPM-PARSEC-UFO simulations. The previous modeling work on
929 this topic used volatility distributions based on particle-phase measurements only, resulting in overall lower
930 volatility and contributions of semi- and intermediate volatility organic vapor.

931 The results from the ICPM-PARSEC-UFO simulations reveal that a competition effect exists between
932 the reductions in maximum supersaturations and critical supersaturations needed for aerosol particle activation
933 into cloud droplets when co-condensation is considered. The reductions in critical supersaturations are greater
934 than the reductions in maximum supersaturation, which results in the simulated CDNC enhancements (simulations
935 with co-condensation are compared against simulations without it under same meteorological conditions). The
936 CDNC enhancements are of the order of 20% under realistic updraft velocities (0.1, 0.3, and 1 m s⁻¹) and
937 correspond to reductions of 1012–136 nm in the smallest activated dry diameters (~~144 to 126 nm, 102 to 88.6 nm,~~
938 72 to 61 nm (~144 to ~128 nm, ~102 to ~88 nm, 72 to ~62 nm for the 0.1, 0.3, and 1 m s⁻¹ updraft scenarios,
939 respectively). The activation of smaller particles into cloud droplets results, as expected, in the formation of more
940 numerous smaller cloud droplets. The critical supersaturation suppressions-reductions result from the additions of
941 soluble organic mass below cloud base along the simulated air parcels' adiabatic ascents while the reductions in
942 maximum supersaturation are caused by the increasing condensation sink provided by more cloud droplets (the
943 source of supersaturation is fixed as the meteorological conditions between simulations with and without co-
944 condensation are kept constant).

945 The predicted CDNC enhancements are highest for the 0.3 m s⁻¹ updraft velocities and depend on several,
946 at least partly, interlinked parameters (see also Lowe et al., 2019). One parameter affecting the modelled CDNC
947 is the availability of the co-condensable organic vapors, which in turn depends on the updraft velocities and, the
948 features of the organic volatility distribution as well as initial temperature and relative humidity. Most organic
949 vapor condenses under the slowest adiabatic ascents and least in the highest due to kinetics. The organic volatility
950 bins spanning from ELVOCs to the lower-volatility IVOCs condense in a similar, updraft-dependent, degree prior
951 reaching the cloud base. Organic vapors of higher volatility involving species such as formic acid condense less

952 efficiently and their condensation is sensitive to ~~the model initialization temperature and~~ the presence of large
953 particles, which are likely to activate regardless of co-condensation. Therefore, small enhancements in particularly
954 SVOC and lower-volatility IVOC concentrations lead to significant enhancements in CDNC, while increases in
955 the most volatile IVOCs and formic acid do not affect CDNC much.

956 The simulations performed with 0.3 m s^{-1} updrafts are repeated using volatility distributions from
957 previous co-condensation studies (Cappa and Jimenez, 2010; Topping et al., 2013; Crooks et al., 2018). By doing
958 so, the BAEC campaign median CDNC enhancement decreased from ~~23.3 to 12.4%–22%~to non-significant~~
959 ~~values.~~ This result is explained by the lower initialization temperature regulating organic vapor availability as
960 well as lower SVOC and IVOC concentrations in previous studies, highlighting the added value of capturing these
961 higher volatility bins within the VBS representations of atmospheric organic species. On the other hand, adding
962 information on the LVOC and ELVOC range do not significantly influence the CDCN enhancements due to co-
963 condensation.

964 The sensitivity of the modelled Δ CDNC to organic vapor concentrations is strongest when high
965 maximum supersaturations ($s_{\text{max}} > 0.2\%$ for the 0.3 m s^{-1} updraft scenarios) are reached. Such conditions are
966 achieved when the dry PNSD surface area (a proxy for the condensation sink) remains below $100 \mu\text{m}^2 \text{ cm}^{-3}$. Under
967 those conditions, CDNC enhancements exceeding 40% are predicted for conditions in which roughly $1 \mu\text{g m}^{-3}$ of
968 co-condensable organic vapor is present.

969 Besides the ~~updraft velocities meteorological conditions~~ and the availability of co-condensable vapors,
970 the CDNC enhancements depend critically on the size distribution of the initial aerosol population. Highest CDNC
971 enhancements are generally achieved when the model is initialized with a relatively weak accumulation mode
972 combined with a large nascent ultrafine particle mode with a geometric mean diameter of ca. 40 nm, with no
973 visible Hoppel minimum present in the distribution. Such conditions are observed most frequently in Spring and
974 September (about 30–40% of the time in years 2012–2017), when new particle formation events take place at
975 SMEAR II.

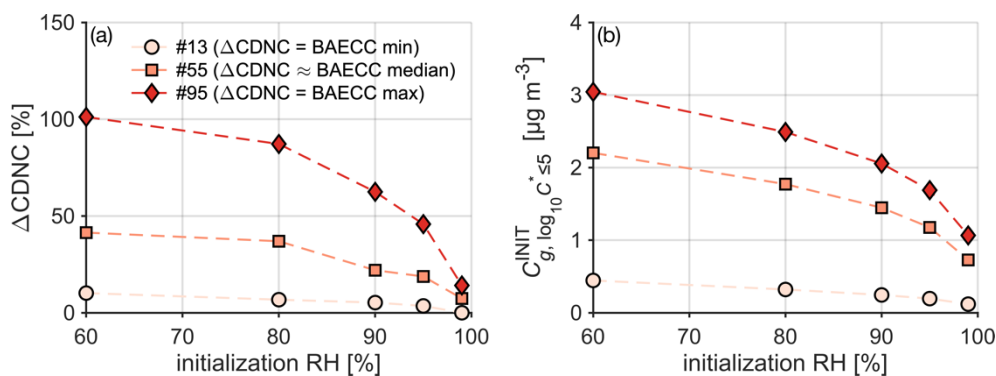
976 Further on, UKESM1 simulations (years 2009–2013) are utilized to investigate the potential impact of
977 including the process of co-condensation on droplet formation in this model over the whole boreal biome using
978 the criteria developed from the SMEAR II case to identify most susceptible PNSD conditions. Overall, the
979 UKESM1 PNSD are different from those observed at SMEAR II even when the strict criteria are used to select
980 the ideal PNSD for co-condensation driven enhancements in CDNC. This discrepancy can arise from multiple
981 causes such as the lack of critical aerosol processes (boundary layer new particle formation), but it could also be
982 a common ESM feature arising from the modal representation of PNSD.– Nonetheless, a Aside from two hotspots
983 (one near the Rocky Mountains in North America, one over northern Kazakhstan, which are not analyzed further),
984 the presence of suitable PNSD, as experienced by UKESM1, is most frequent over Fennoscandia and western
985 parts of Siberia in spring, yet the frequencies at which those PNSD are modelled remained much lower than those
986 obtained from the long-term SMEAR II PNSD measurements (2–6% in UKESM1). ~~It is likely that the~~
987 ~~incorporation of boundary layer NPF in UKESM1 will increase this frequency.~~ Perhaps surprisingly, suitable
988 PNSD are never modeled over most of Siberia, suggesting that for the model configuration of UKESM1 used in
989 this study, the process of co-condensation would not be expected to have an influence on droplet formation in this
990 area. This is due to the low concentration of ultrafine particle particles modeled in the area.

991 In summary, these results highlight the potential significance of co-condensation in pristine boreal
 992 environments with a nascent ultrafine particle mode present. Such conditions are met over Fennoscandia and
 993 Western parts of Siberia in Spring and to a lesser extent in the Fall, when NPF takes place. For future modelling
 994 purposes, it is vital to stress the importance of the accurate representation of PNSD for capturing the role of co-
 995 condensation of organics on CDNC enhancements, including appropriate description of boundary layer NPF.
 996 Because the modelled CDNC enhancements are so significant, further research focus especially regarding
 997 observations of the co-condensation should be targeted in the future to motivate future assessments of co-
 998 condensation-driven radiative forcing. Perhaps this work inspires aircraft measurements (of the relevant
 999 parameters discussed in this paper) to take place over the Fennoscandia in the future to finally narrow down the
 1000 importance of co-condensation for the accurate representation of CDNC in GCMs.-

1002 Appendix A

1004 The effect of the initialization relative humidity, organic mass accommodation coefficient and vaporization
 1005 enthalpy on the modelled CDNC enhancements due to co-condensation are investigated for three individual
 1006 simulations. The three simulations were selected as they are representative of low, median and high Δ CDNC
 1007 simulated during BAECC (simulation IDs #13, #55 and #95, respectively; Table S.1).

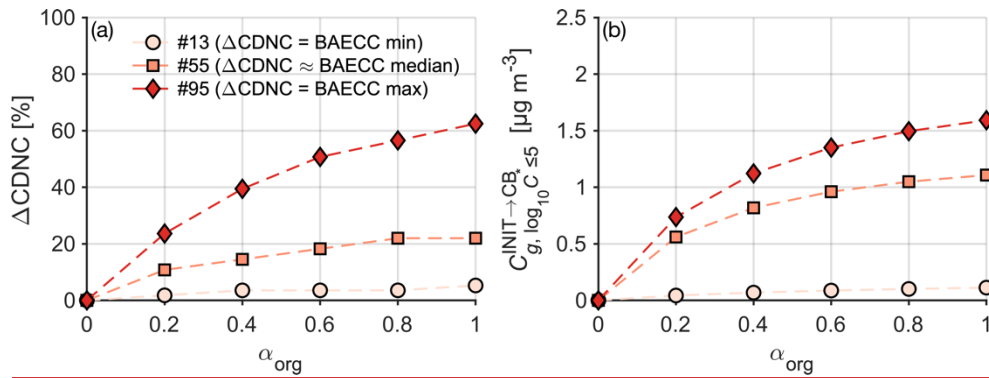
1008 The initialization RH affects the availability of organic vapor for co-condensation: when PARSEC-UFO
 1009 is initialized under high RH ($\sim >95\%$), most organic vapor is scavenged at initial conditions causing negligible
 1010 enhancements in CDNC. On the other hand, if the initialization RH is lower ($<90\%$), less organic vapor is
 1011 scavenged at initial conditions, and the modeled Δ CDNC are greater (Fig. A.1). By varying α_{org} , the effect of the
 1012 assumption of ideality has on the projected CDNC enhancements is probed. For simplicity, the mass
 1013 accommodation coefficient for organics (α_{org}) is set to be constant across the volatility bins. By reducing α_{org}
 1014 from 1 to 0.8, the condensation of organics reduces. However, this impacts CDNC only in the simulation ID #95
 1015 (Fig. A.2; CDNC reduces from $\sim 62\%$ to 55%), i.e., simulation with the highest Δ CDNC. When $\alpha_{\text{org}} < 0.4$, also
 1016 the simulation ID #55 shows a reduction in the modeled Δ CDNC as it drops from $\sim 22\%$ to $\sim 15\%$. The selection
 1017 of the enthalpy of vaporization for organics does not affect Δ CDNC (Fig. A.3). Over all, the initial relative
 1018 humidity plays the most critical role out of the three parameters considered here (RH, α_{org} and ΔH_{VAP}), on the
 1019 modelled Δ CDNC.



1023 **Figure A.1** The modelled CDNC enhancements as function of initialization RH ranging from 60% to 99%
 1024 (indicated with different colors) for each simulation ID are shown, respectively. The initialization temperature
 1025 and pressure are fixed to values shown in Table S.1. and only the volatility bins $\log_{10} C^* \leq 5$ are included, which

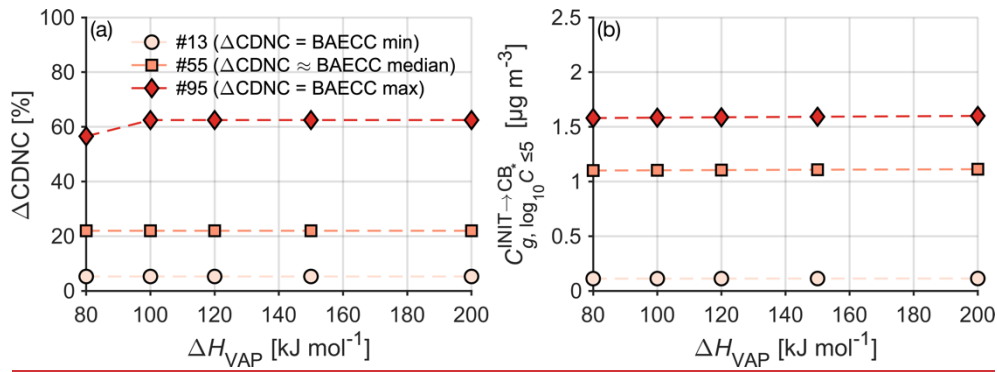
1026
1027
1028
1029
1030
1031

is motivated e.g., by Fig. 4. The simulations are performed with an updraft velocity of 0.3 m s^{-1} . The markers with the lightest color refer to the BAEC simulation, where co-condensation influenced ΔCDNC negligibly (ID #13, $\Delta\text{CDNC} = 3\%$), the orange markers to the BAEC median ΔCDNC (ID #55), and the red markers represent a simulation, where the modelled ΔCDNC was greatest (ID #95, $\Delta\text{CDNC} = 75\%$).



1032
1033
1034
1035
1036

Figure A.2 The modelled CDNC enhancements as function of mass accommodation coefficient for organics (α_{org}) ranging from zero to one. The colorings and presented simulations are same as in Fig. A.1.



1037
1038
1039
1040
1041
1042

Figure A.3 The modelled CDNC enhancements as function of vaporization enthalpy for organics (ΔH_{VAP}) ranging from zero to one. The colorings and presented simulations are same as in Fig. A.1.

1043

1044 **Data availability**

1045 The [ICPM-PARSEC-UFO](#) input and outputs for reproducing the figures will be available on the Bolin Centre
1046 database.

1047

1048 **Competing interests**

1049 The authors have the following competing interests: Some authors are members of the editorial board of
1050 Atmospheric Chemistry and Physics. The peer-review process will be guided by an independent editor. One or
1051 more authors have received funding from European Union's Horizon 2020 research and innovation programme,
1052 European Research Council, Knut and Alice Wallenberg foundation, Academy of Finland and US Department of
1053 Energy, [UK Natural Environment Research Council \(NERC\)](#), and/or support from ACTRIS Translational Access
1054 and ACTRIS-HY. The authors have no other competing interests to declare.

1055 **Author contributions**

1056 LH, IR, DGP and CM conceptualized the idea of the study [and designed the simulations](#). LH prepared the ~~model~~
1057 [PARSEC-UFO](#) input data, performed the [PARSEC-UFO](#) simulations, analyzed the simulation outputs, made the
1058 [majority of the](#) figures and wrote the manuscript with contributions from the coauthors. TP designed and led the
1059 BA ECC campaign. CM performed the FIGAERO-I-CIMS measurements, WH processed and delivered the
1060 FIGAERO-I-CIMS data and gave input on the volatility distribution calculation. RR assisted [LH](#) with the
1061 radiosonde data ~~and~~, provided the hygroscopicity seasonal cycle data [and contributed to the PARSEC-UFO](#)
1062 [description writing](#). ET and DGP performed the UKESM1 simulations and DGP designed and processed the data
1063 for analysis input parameters to droplet activation parameterization. [DGP and PB created PARSEC and extended](#)
1064 [it to include UFO, provided documentation for PARSEC-UFO and contribution to description](#). SB visualized the
1065 UKESM1 data, [assisted LH with FORTRAN programming and](#) ~~and~~ gave input on the data interpretation. ~~LH~~
1066 [wrote the paper with input from all co-authors](#).

1067 **Acknowledgements**

1068 We gratefully acknowledge Samuel Lowe for developing the unified framework for organics onto the ICPM
1069 (Lowe, 2020), the useful discussions, code and support. We acknowledge Ellie Duncan for useful discussions and
1070 support regarding the UKESM1 data [and Megan Haslum for their documentation on PARSEC-UFO Köhler](#)
1071 [terms](#). We acknowledge Pasi Aalto and SMEAR II staff for their efforts during the BA ECC campaign. [We thank](#)
1072 [and Dmitri Moisseev, Federico Bianchi and Annica Ekman](#) for useful discussions. ~~regarding updraft velocities.~~
1073 ~~We thank Federico Bianchi for useful discussion regarding NPF in the Northern Hemisphere.~~ We acknowledge
1074 the Atmospheric Radiation Measurement (ARM) Program for their inputs during BA ECC, the interpolated
1075 radiosonde data were obtained from the ARM Program sponsored by the U.S. Department of Energy, Office of
1076 Science, Office of Biological and Environmental Research, Climate and Environmental Sciences Division. We
1077 acknowledge use of the Monsoon2 system, a collaborative facility supplied under the Joint Weather and Climate
1078 Research Programme, a strategic partnership between the Met Office and the Natural Environment Research
1079 Council. We also thank all the people responsible for the development of UKESM1. DGP would like to extend a
1080 personal thanks to Dr Alistair Sellar, who provided support for the configuration of the UKESM1 simulations
1081 performed as part of the AeroCom GCM Trajectory experiment on which these simulations are based.

1082 **Funding**

1083 Financial support from the European Union's Horizon 2020 research and innovation programme (project FORCeS
1084 under grant agreement No 821205, project FOCI under grant agreement No101056783, project CRiceS under
1085 grant agreement No 101003826), European Research Council (Consolidator grant INTEGRATE No 865799,
1086 starting grant CHAPAs No 850614), and Knut and Alice Wallenberg foundation (Wallenberg Academy
1087 Fellowship projects AtmoRemove No 2015.0162 and CLOUDFORM No 2017.0165), Academy of Finland via a
1088 Flagship programme for Atmospheric and Climate Competence Center (ACCC, No 337549) and projects No
1089 353386, 334792, 340791, 325681 are gratefully acknowledged. The BA ECC campaign was supported by US
1090 Department of Energy (Petäjä, No DE-SC0010711) and additional measurements were supported via ACTRIS
1091 Transnational Access. University of Helsinki is acknowledged for supporting the SMEAR II station via ACTRIS-
1092 HY. [DGP and PB acknowledge support from Natural Environment Research Council grant no. NE/W001713/1](#)

1093 for the creation of the Pseudo-Adiabatic bin-micRophySics university of Exeter Cloud parcel model (PARSEC)
1094 and for adding Unified Framework for Organics (UFO) to PARSEC to create PARSEC-UFO.
1095

1096

1097 **Tables**

1098

1099

1100

1101

1102

1103

Table 1 Overview of the [PARSEC-UFO](#) simulation input parameters that remain unchanged in all of the simulation sets conducted with or without co-condensation. The updraft velocities, organic volatility distributions and [organic](#) vapor concentrations that change between simulation sets are reported in Table 2 together with the median model outputs. The time series of these model input data are shown in Fig.1. All the modelling scenarios are initiated at 90% relative humidity.

Parameter	Min	Max	Median
Aitken mode number conc. N_1 [cm^{-3}] ^a	160	12 316	1491
Accumulation mode number conc. N_2 [cm^{-3}] ^a	44	2 433	560
Aitken mode geometric mean dry diameter D_1 [nm] ^a	7.1	71.0	23.8
Accumulation mode geometric mean dry diameter D_2 [nm] ^a	62.6	201.9	115.3
Geom. standard deviation of Aitken mode σ_1 ^a	1.50	2.08	1.75
Geom. standard deviation of accumulation mode σ_2 ^a	1.33	2.06	1.75
Number of PNSD size bins	400	400	400
Organic mass fraction f_{org} [%] ^b	25	84	68
Initial T [K] ^c	271	295	279
Initial p [hPa]	980	980	980
Mass accommodation coefficient α	1	1	1
Vaporization enthalpy for organics ΔH_{vap} [kJ mol⁻¹]^d	150	150	150
Effective soluble fraction of organics	1	1	1
Surface tension γ [mN m ⁻¹]	72.8	72.8	72.8
ICPM time step [s]	10⁻³	10⁻³	10⁻³

1104

^a Retrieved from fits assigned onto the measured aerosol size distributions (Aalto et al., 2001) using a fitting algorithm by Hussein et al. (2005).

1105

^b Retrieved from aerosol chemical composition measurements (Heikkinen et al., 2020).

1106

^c Retrieved from radio soundings (ARM Data Center, 2014). The temperatures shown were recorded when the relative humidity measured by the radiosonde reached 90%, i.e., the initial relative humidity used for the adiabatic ascents.

1107

^d[Note that in the volatility distribution construction \(offline from PARSEC\) the \$\Delta H_{\text{vap}}\$ is temperature-adjusted following Epstein et al. \(2010\).](#)

1108

1109

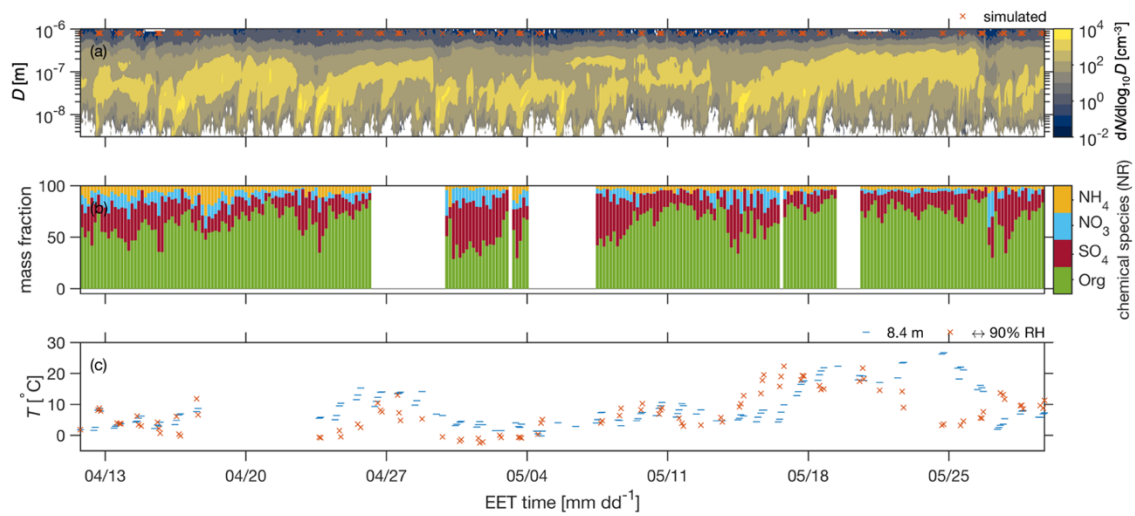
1110 **Table 2-3** Overview of the PARSECF-UFO simulation output for the no co-condensation (noCC) and co-
 1111 condensation (CC with F volatility distribution) simulations performed using varying updraft velocities.

<u>Parameter</u>	<u>Median</u>		
<u>Updraft velocity w [m s⁻¹]^a</u>	<u>0.1</u>	<u>0.3</u>	<u>1.0</u>
<u>Parcel displacement before CB [m]</u>	<u>190</u>	<u>190</u>	<u>190</u>
<u>Cloud droplet number conc. CDNC_{noCC} [cm⁻³]^b</u>	<u>158</u>	<u>292</u>	<u>523</u>
<u>Cloud droplet number conc. CDNC_{CC} [cm⁻³]^b</u>	<u>186</u>	<u>400</u>	<u>618</u>
<u>CDNC enhancement ΔCDNC [%]^b</u>	<u>15.6</u>	<u>22.1</u>	<u>18.9</u>
<u>Maximum supersaturation s_{\max}^{noCC} [%]</u>	<u>0.14</u>	<u>0.24</u>	<u>0.40</u>
<u>Maximum supersaturation s_{\max}^{CC} [%]</u>	<u>0.14</u>	<u>0.22</u>	<u>0.38</u>
<u>Smallest activated dry radius r_{noCC}^* [nm]</u>	<u>72</u>	<u>51</u>	<u>36</u>
<u>Smallest activated dry radius r_{CC}^* [nm]</u>	<u>64</u>	<u>44</u>	<u>31</u>
<u>Initial organic vapor conc. $\sum C_g^{\text{INIT}}$ [$\mu\text{g m}^{-3}$]</u>	<u>22.05</u>	<u>2.05</u>	<u>2.05</u>
<u>Organic vapor condensed below cloud base $\sum C_g^{\text{INIT}} - \sum C_g^{\text{CB}}$ [$\mu\text{g m}^{-3}$]</u>	<u>1.82</u>	<u>1.41</u>	<u>0.55</u>
<u>Fraction of organic vapor condensed below cloud base $\Delta C_g^{\text{INIT} \rightarrow \text{CB}}$ [%]</u>	<u>91</u>	<u>70</u>	<u>28</u>

1112 ^a Model input parameters crucial for understanding the differences between the co-condensation simulation model outputs.

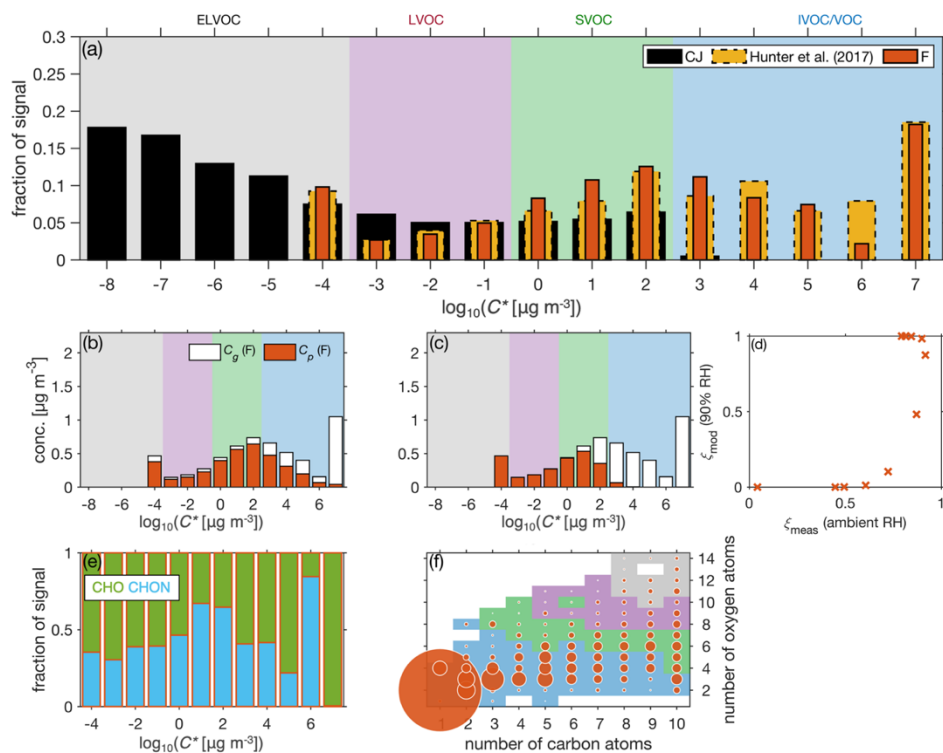
1113 ^b The CDNC represent the integrated number concentration in size bins exceeding the critical radius in wet size at 50 meters above cloud base
 1114 (CB).
 1115
 1116
 1117

1118 **Figures**
1119



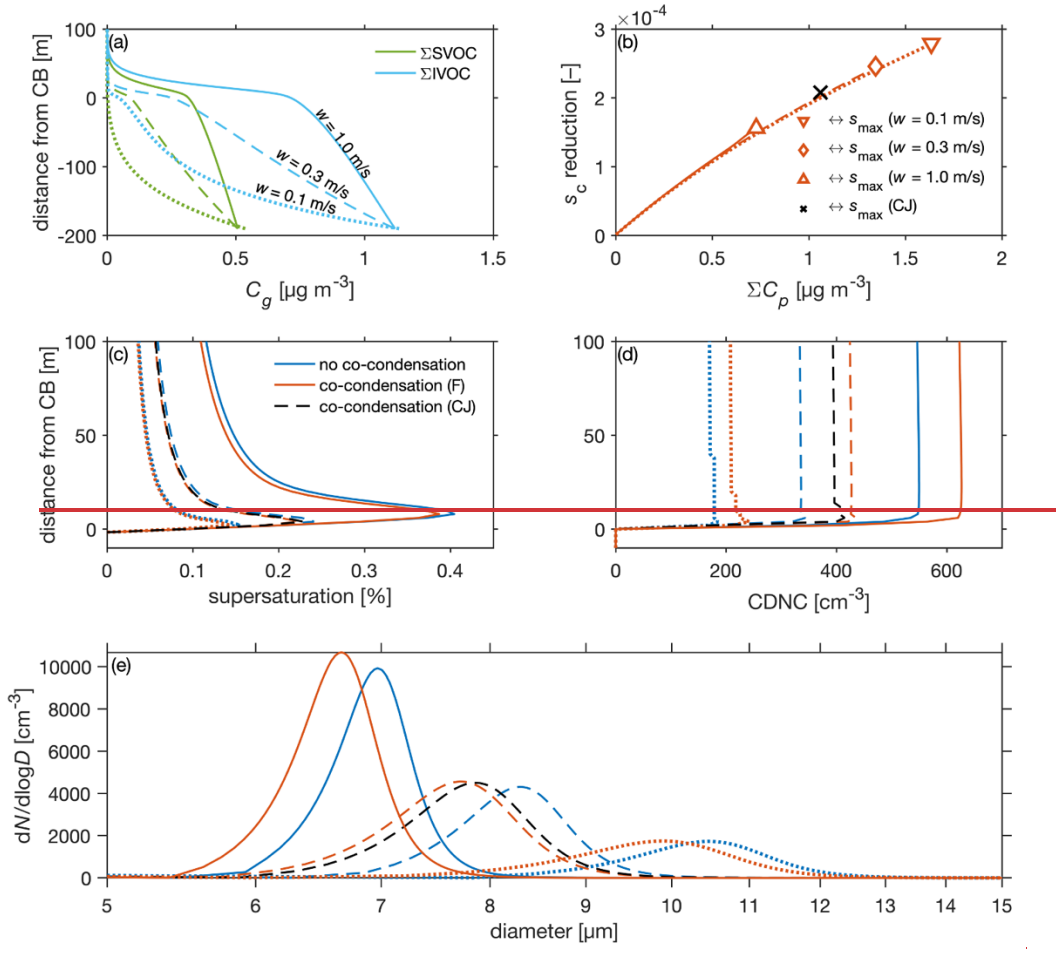
1120
1121
1122
1123
1124
1125
1126
1127

Figure 1 (a) Time-series of the particle number size distribution in the time period of interest during BA ECC. The time points used for the ICPM-PARSEC-UFO initialization are shown as red/orange crosses. (b) The non-refractory (NR) chemical composition of sub-micrometer aerosol particles for the same time period. (c) The time series of ambient temperature near ground level (8.4 m a.g.l.) is shown in blue and the ICPM-PARSEC-UFO initialization temperature corresponding to RH = 90% from the interpolated radiosonde data product is shown in orange. The subpanels have a common x-axis representing the East European winter time (UTC+2).

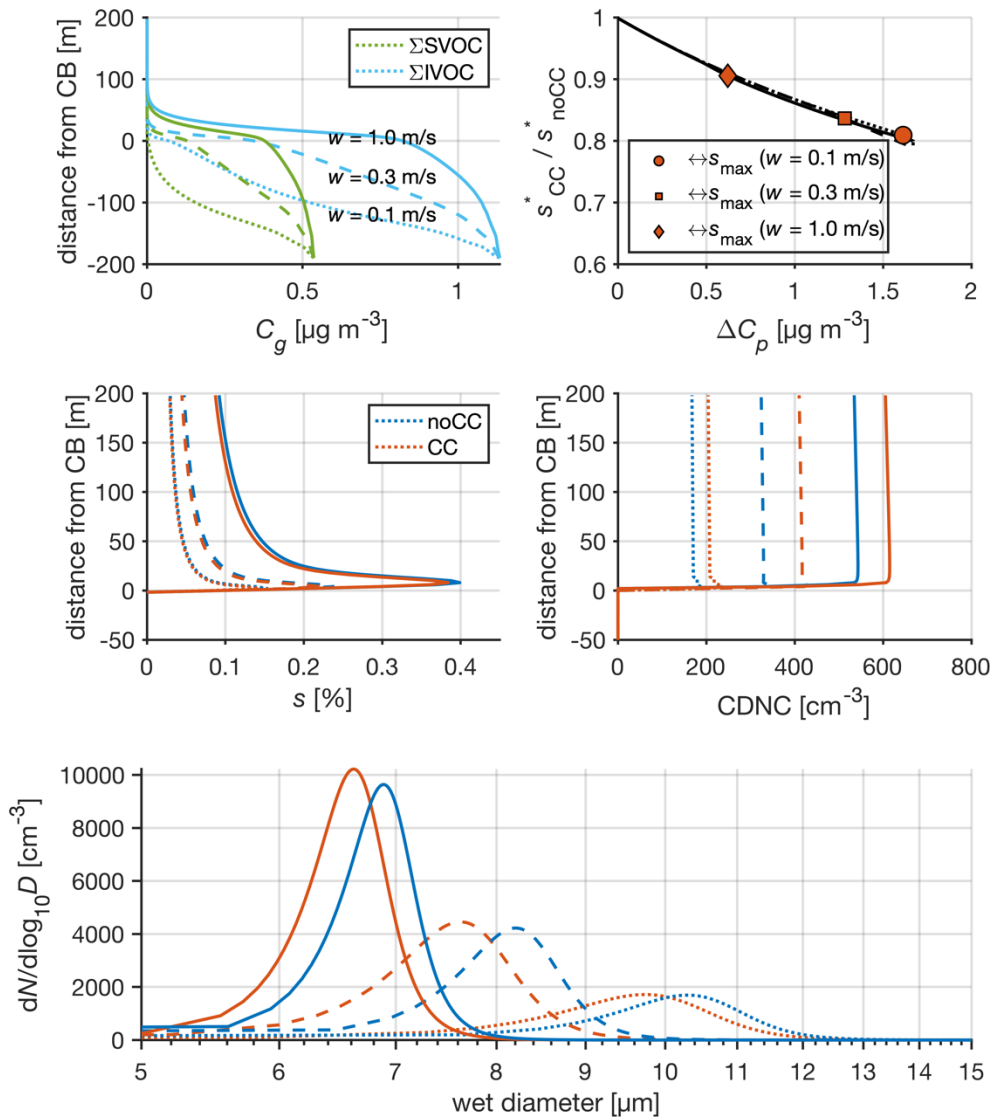


1129
 1130
 1131
 1132
 1133
 1134
 1135
 1136
 1137
 1138
 1139
 1140
 1141

Figure 2 (a) The normalized volatility distributions ($C_g + C_p$) from Cappa and Jimenez (2010; CJ) and the BAEC I-CIMS measurements (F) using the modified Li et al. (2016) molecular formulae-based parameterizations. A volatility distribution from Hunter et al. (2017) constructed from the BEACHON-RoMBAS measurement campaign is shown in this figure by the dashed bars. The volatility ranges for ELVOC, LVOC, SVOC and IVOC/VOC are shown in color scales. These C^* limits apply throughout the paper. (b–c) The partitioning predicted based on the FIGAERO-I-CIMS gas- and particle-phase measurements and the ICPM-PARSEC-UFO, respectively. The PARSEC-UFO partitioning corresponds to 90% RH while the ambient observation is under ambient RH. (d) A scatterplot drawn between the FIGAERO-I-CIMS derived partitioning coefficients (ζ_{meas}) and ICPM-PARSEC-UFO-derived coefficients (ζ_{mod}) for the 12 different volatility bins. Panels (e–f) represent the gas phase molecular composition from the FIGAERO-I-CIMS: panel (e) the distribution between organic nitrates and non-nitrates and panel (f) the degree of oxygenation in the form of oxygen and carbon numbers. The marker size in panel f corresponds to the concentration of signal for the given n_C and n_O combination.

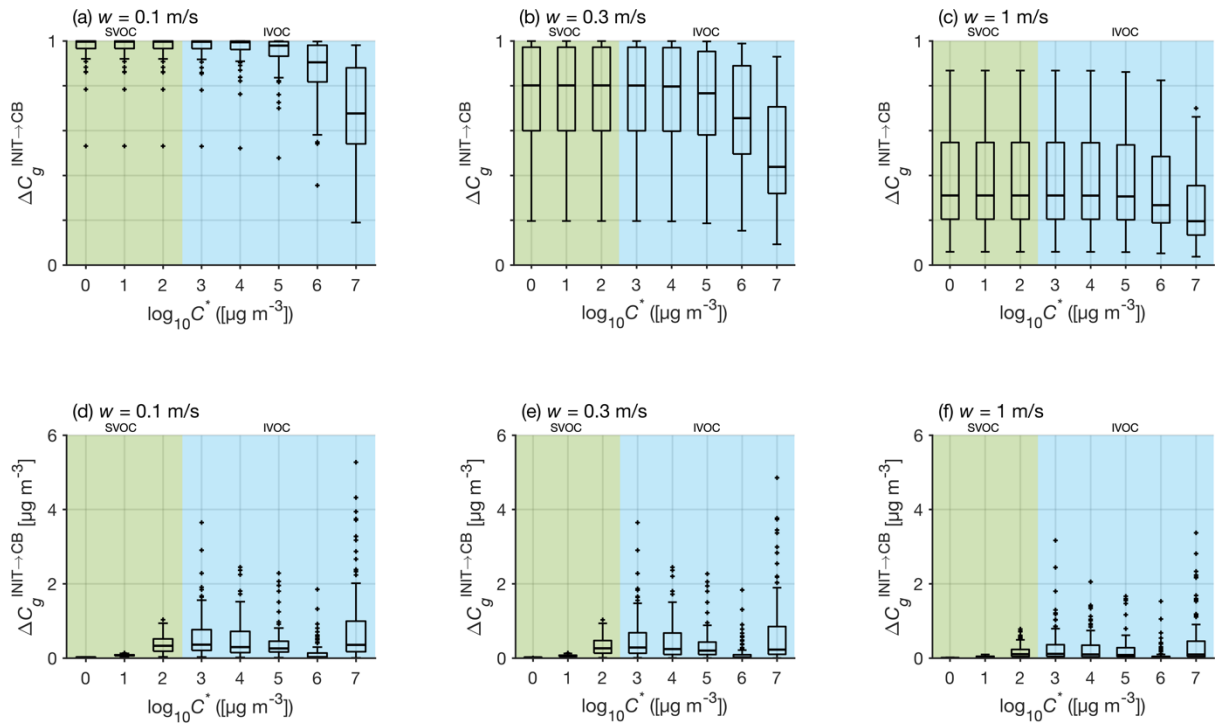


1142

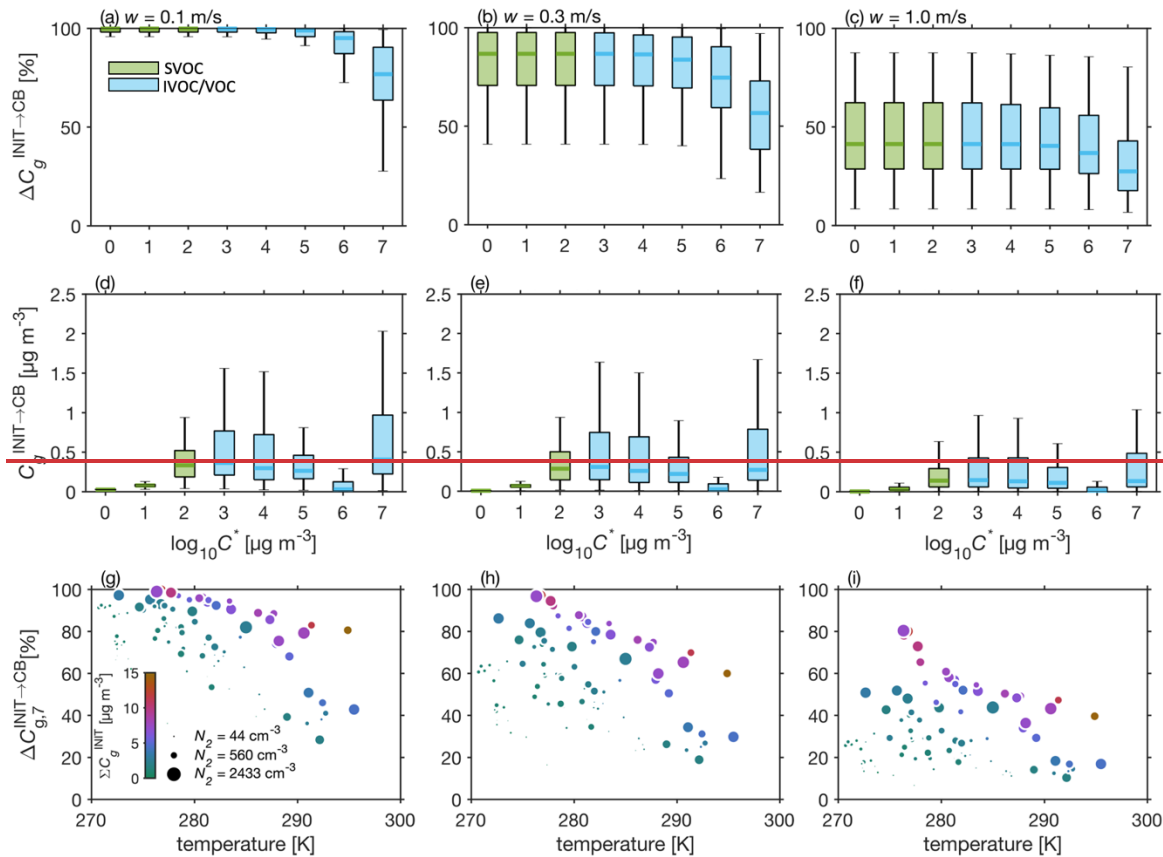


1143
 1144
 1145
 1146
 1147
 1148
 1149
 1150
 1151
 1152
 1153
 1154

Figure 3 A summary of simulated cloud microphysics on May 11, 134:379 EET during the BAECC campaign. Simulations are performed both with and without organic condensation (red and blue lines, respectively) for three different updraft velocities (see line styles from panel a). The initial temperature is 279 K, pressure 980 hPa and supersaturation -0.1% ($RH = 90\%$). (a) The concentration of SVOCs and IVOCs in the gas phase as a function of distance from cloud base (CB). SVOCs have $\log_{10}C^* = [0, 2]$ and IVOCs $\log_{10}C^* = [3, 7]$ under 279K. (b) The absolute change in critical supersaturation as a function of soluble mass added along the ascent by condensing organics. The markers represent the reductions at the maximum supersaturation (s_{max}). (c–d) The evolution of the s_{max} and CDNC with altitude, respectively. (e) The droplet spectra 50 meters above CB. Size bins exceeding the critical diameter as predicted by Köhler theory are calculated as cloud droplets. The red lines are obtained with F volatility distributions and the black with CJ (Fig. 2a). The line type specifications in panels d–e follow those shown in panel a and the colors used in panels d–e are documented in the panel c legend.



1155



1156

1157

1158

1159

1160

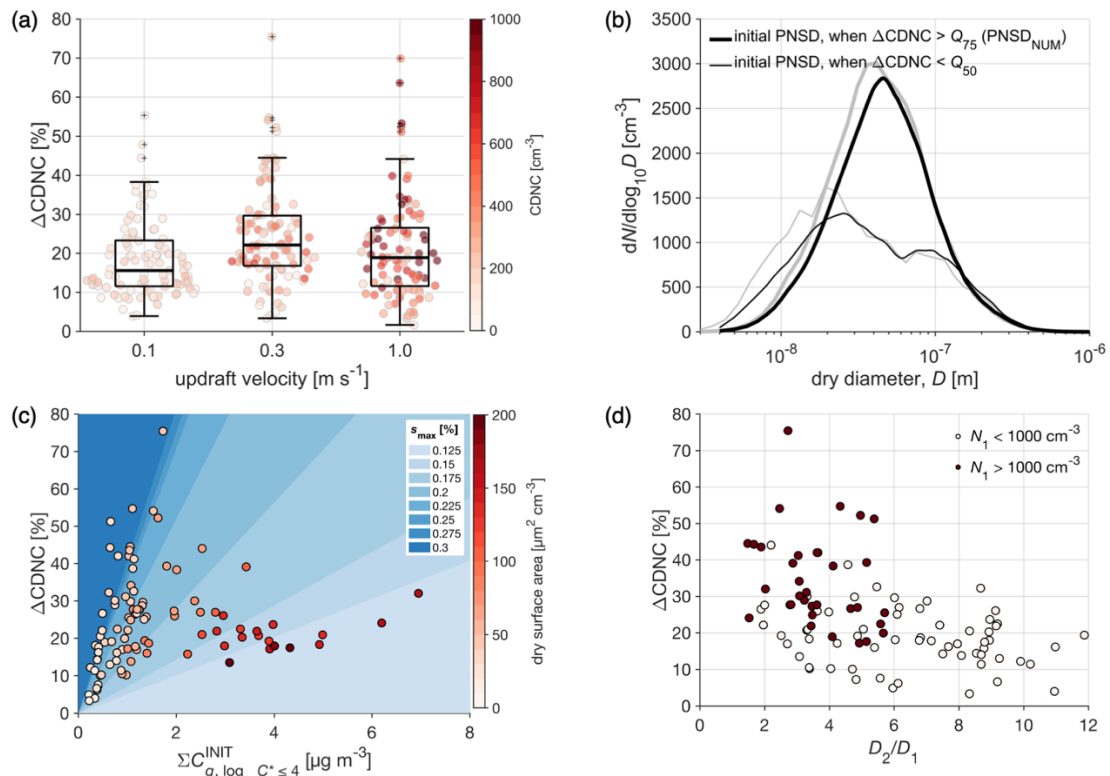
1161

1162

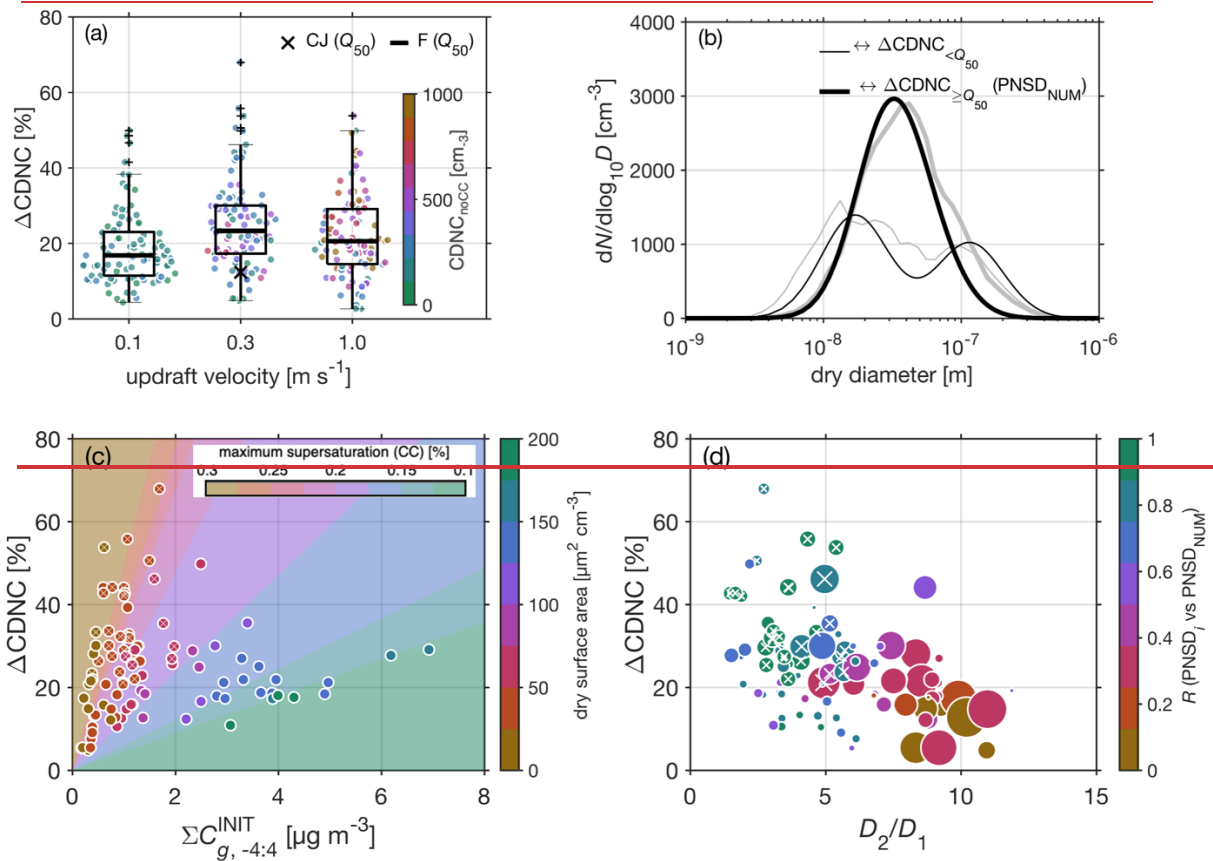
1163

1164

Figure 4 Box plots showing the fractions (a–c) and absolute concentrations (d–f) of organic vapor condensed below cloud base per volatility bin for the 0.1, 0.3 and 1.0 m s⁻¹ updraft scenarios, respectively. The shaded backgrounds reflect SVOC (green) and IVOC/VOC (blue) volatility ranges under PARSEC-UFO initialization temperature. The volatility ranges in panels a–f start from $\log_{10}C^* = 0$ because of the negligible gas-phase concentrations in the lower volatility bins. The final row (g–i) shows how the fraction of vapor condensed from the highest volatility bin (y axis) behaves as a function of ICPM initialization temperature (x axis), accumulation mode number concentration (marker size) and total initial organic vapor concentration (marker color).



1166



1167

1168

1169

1170

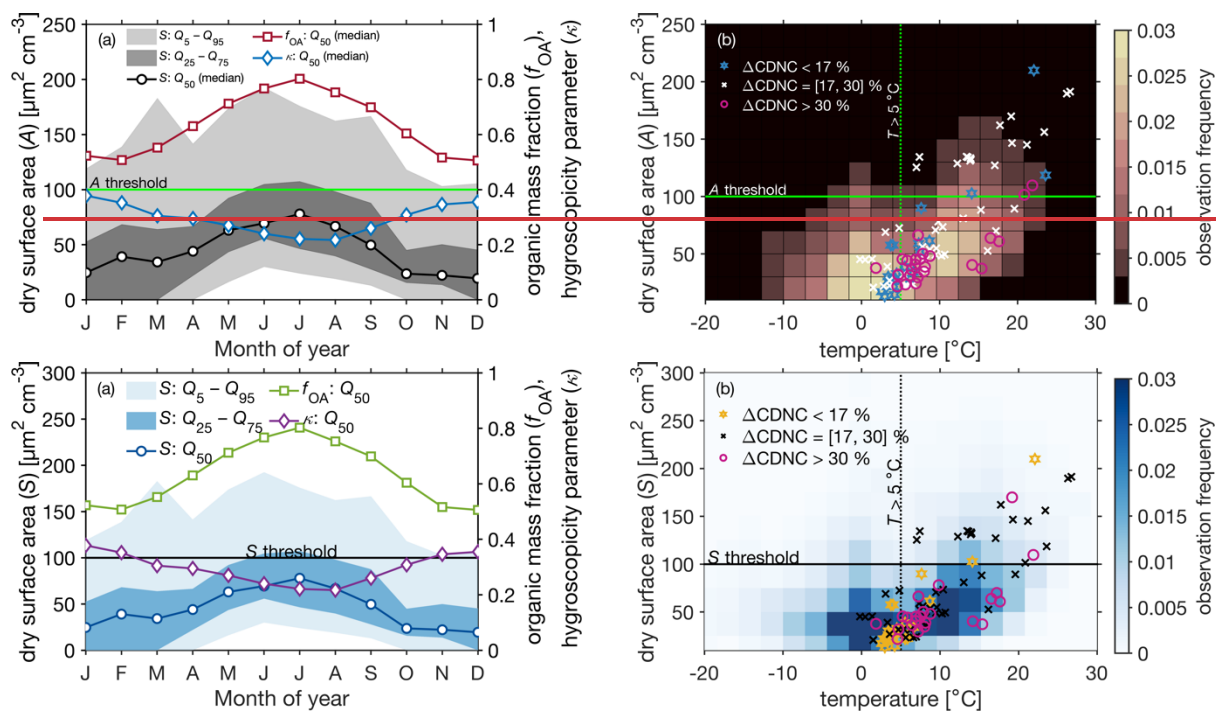
1171

1172

1173

Figure 5 (a) Box plots showing the predicted ΔCDNC (using F volatility distributions) due to co-condensation in the three different modelling scenarios (0.1, 0.3 and 1.0 m s^{-1} updrafts). The median (Q_{50}) ΔCDNC yielded using the CJ distribution is shown with a black cross. The colorful markers represent CDNC (without accounting for co-condensation) in form of a swarmplot. The median (Q_{50}) ΔCDNC yielded using the CJ distribution are shown in Fig. S.7. (b) The median initial dry size distributions calculated from the simulations exceeding the 75th percentile in ΔCDNC ($>Q_{75}$; thick lines) and remaining

1174 below the Δ CDNC 25th percentile median ($\leftrightarrow Q_{5025}$; thin lines), respectively. The PNSD medians are calculated by taking
1175 a median of the PNSD calculated using the log-normal parameters from both sets of simulations (in black) and from the
1176 measurement data (in grey). The data are shown for the simulation performed with a 0.3 m s^{-1} updraft. The black lines are
1177 drawn from the ICPM input modal parameters and the grey lines from the measured size distribution data. (c) The relationship
1178 between the modeled Δ CDNC and the initial organic vapor concentration within the $\log_{10} C^*$ range from -4 to 4 ($C_{g,-4:4}^{\text{INIT}}$). The
1179 marker color-coding represents the initial dry size distribution surface area (S). The plot background is colored with the
1180 modeled maximum supersaturations (s_{max}). These are calculated from s_{max} binned Δ CDNC vs $C_{g,-4:4}^{\text{INIT}}$ linear fit 90% confidence
1181 intervals (CI; area between CI is colored). The figure shows that S anticorrelates with s_{max} (see Eq. 3). The data are shown
1182 for the simulations performed with a 0.3 m s^{-1} updraft only. (d) The figure evaluates how well the simple criteria ($D_2/D_1 < 6$
1183 and $N_1 > 1000 \text{ cm}^{-3}$) works on the PARSEC-UFO simulations.
1184



1185

1186

1187

1188

1189

1190

1191

1192

1193

1194

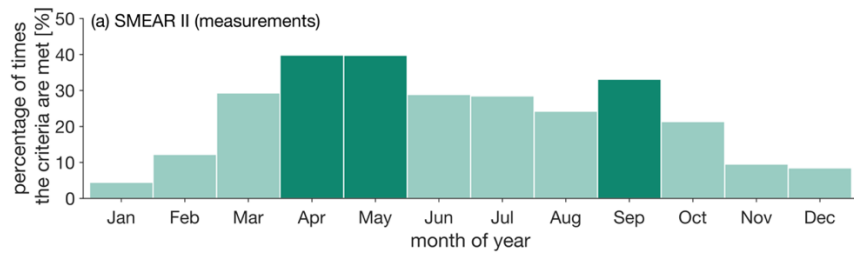
1195

1196

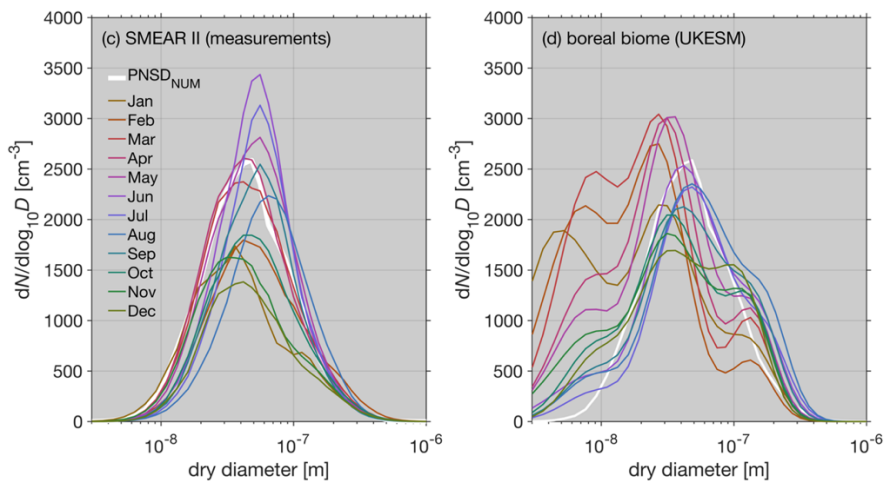
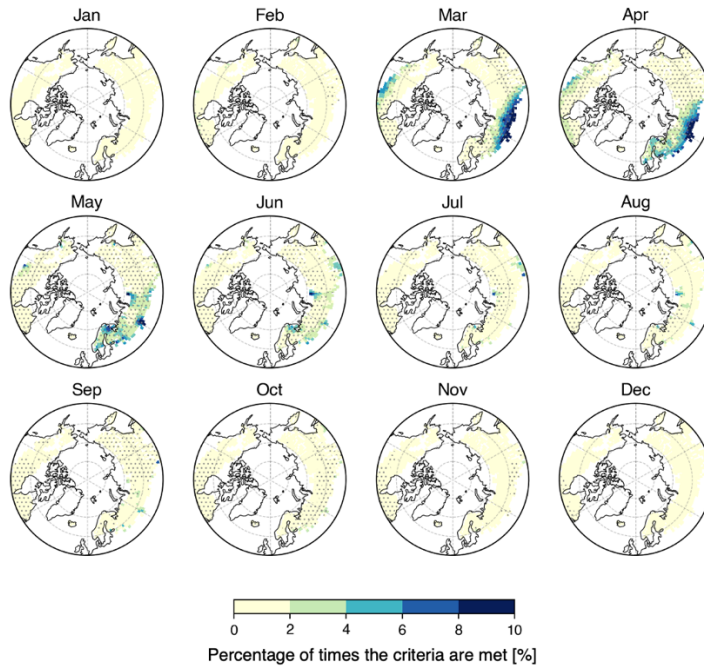
1197

1198

Figure 6 (a) The seasonal cycle of the dry aerosol size distribution surface area (S) calculated from the long-term aerosol size distribution observations (2012–2017; left y-axis), where the markers represent the median values, the darkest shading the interquartile range and the lighter shading the area between the 5th and 95th percentiles. The panel also contains the median seasonal cycles of organic mass fraction and the κ hygroscopicity parameter compiled from the same long-term period (right y-axis). The green horizontal line refers to the dry surface area threshold of 100 $\mu\text{m}^2 \text{cm}^{-3}$ from Fig. 5, under which the greatest ΔCDNC are modeled using the BA ECC data. (b) A density plot showing the observations of S under different ambient temperatures during the 2012–2017 long-term period. The A - S threshold of 100 $\mu\text{m}^2 \text{cm}^{-3}$ is again shown with the horizontal green line. The vertical dashed green line is a rough estimate for the start of the thermal growing season, which also refers to the starting point of the majority of the BVOC emissions. The markers show the IC_{CPM}-PARSEC-UFO simulation data color-coded with the associated ΔCDNC (simulations yielding the ΔCDNC below the 25th percentile are shown in blue, simulations yielding ΔCDNC above the 75th percentile in red and the simulations between those limits are shown in white).



(b) boreal biome monthly medians (UKESM)



1199
1200
1201
1202
1203
1204
1205
1206
1207
1208
1209
1210
1211

Figure 7 (a) Percentage of times the criteria ($D_2/D_1 < 6$ and $N_1 > 1000 \text{ cm}^{-3}$) are met at SMEAR II between the 2012–2017 measurement period. D_2 , D_1 and N_1 are attained from bimodal fits calculated for the measured PNSD using the Hussein et al. (2005) algorithm. (b) The percentage of times the criteria are met in a 2009–2013 UKESM1 simulation. D_2 , D_1 and N_1 are the modal parameters representing the soluble accumulation mode and soluble Aitken mode parameters. The gray markers refer to boreal grid cells, where the median updraft velocity at cloud base is between 0.2 and 0.5 m s^{-1} . (c–d) Monthly median size distributions from the long-term PNSD measurements at SMEAR II and UKESM1 simulation, respectively. The UKESM1 size distributions are calculated from the log-normal PNSD parameters for nucleation, soluble Aitken and soluble accumulation modes assuming geometric standard deviations of $\sigma = 1.59$ for nucleation and soluble Aitken modes and $\sigma = 1.4$ for the soluble accumulation mode. The soluble coarse mode is not included in the analysis.

1212 **References**

- 1213 Aalto, P., Hämeri, K., Becker, E., Weber, R., Salm, J., Mäkelä, J. M., Hoell, C., O’ Dowd, C. D.,
1214 Hansson, H.-C., Väkevä, M., Koponen, I. K., Buzorius, G., and Kulmala, M.: Physical characterization
1215 of aerosol particles during nucleation events, *Tellus B: Chemical and Physical Meteorology*, 53, 344–
1216 358, <https://doi.org/10.3402/tellusb.v53i4.17127>, 2001.
- 1217 Allan, J. D., Alfarra, M. R., Bower, K. N., Coe, H., Jayne, J. T., Worsnop, D. R., Aalto, P. P., Kulmala,
1218 M., Hyötyläinen, T., Cavalli, F., and Laaksonen, A.: Size and composition measurements of
1219 background aerosol and new particle growth in a Finnish forest during QUEST 2 using an Aerodyne
1220 Aerosol Mass Spectrometer, *Atmos. Chem. Phys.*, 6, 315–327, [https://doi.org/10.5194/acp-6-315-](https://doi.org/10.5194/acp-6-315-2006)
1221 2006, 2006.
- 1222 AeroCom: <https://aerocom.met.no/>, last access: 21 November 2022.
- 1223 ARM Data Center: Atmospheric Radiation Measurement (ARM) user facility. 2014, updated hourly.
1224 Interpolated Sonde (INTERPOLATEDSONDE). 2014-04-01 to 2014-07-01, ARM Mobile Facility
1225 (TMP) U. of Helsinki Research Station (SMEAR II), Hyytiälä, Finland; AMF2 (M1). Compiled by M.
1226 Jensen, S. Giangrande, T. Fairless and A. Zhou., 2014.
- 1227 Artaxo, P., Hansson, H.-C., Andreae, M. O., Bäck, J., Alves, E. G., Barbosa, H. M. J., Bender, F.,
1228 Boutsoukidis, E., Carbone, S., Chi, J., Decesari, S., Després, V. R., Ditas, F., Ezhova, E., Fuzzi, S.,
1229 Hasselquist, N. J., Heintzenberg, J., Holanda, B. A., Guenther, A., Hakola, H., Heikkinen, L.,
1230 Kerminen, V.-M., Kontkanen, J., Krejci, R., Kulmala, M., Lavric, J. V., Leeuw, G. de, Lehtipalo, K.,
1231 Machado, L. A. T., McFiggans, G., Franco, M. A. M., Meller, B. B., Morais, F. G., Mohr, C., Morgan,
1232 W., Nilsson, M. B., Peichl, M., Petäjä, T., Praß, M., Pöhlker, C., Pöhlker, M. L., Pöschl, U., Randow,
1233 C. V., Riipinen, I., Rinne, J., Rizzo, L. V., Rosenfeld, D., Dias, M. A. F. S., Sogacheva, L., Stier, P.,
1234 Swietlicki, E., Sörgel, M., Tunved, P., Virkkula, A., Wang, J., Weber, B., Yáñez-Serrano, A. M., Zieger,
1235 P., Mikhailov, E., Smith, J. N., and Kesselmeier, J.: Tropical and Boreal Forest – Atmosphere
1236 Interactions: A Review, *Tellus B: Chemical and Physical Meteorology*, 74, 24–163,
1237 <https://doi.org/10.16993/tellusb.34>, 2022.
- 1238 Bardakov, R., Riipinen, I., Krejci, R., Savre, J., Thornton, J. A., and Ekman, A. M. L.: A Novel
1239 Framework to Study Trace Gas Transport in Deep Convective Clouds, *Journal of Advances in*
1240 *Modeling Earth Systems*, 12, e2019MS001931, <https://doi.org/10.1029/2019MS001931>, 2020.
- 1241 Barley, M., Topping, D. O., Jenkin, M. E., and McFiggans, G.: Sensitivities of the absorptive
1242 partitioning model of secondary organic aerosol formation to the inclusion of water, *Atmos. Chem.*
1243 *Phys.*, 9, 2919–2932, <https://doi.org/10.5194/acp-9-2919-2009>, 2009.
- 1244 Bellouin, N., Quaas, J., Gryspeerdt, E., Kinne, S., Stier, P., Watson-Parris, D., Boucher, O., Carslaw,
1245 K. S., Christensen, M., Daniau, A.-L., Dufresne, J.-L., Feingold, G., Fiedler, S., Forster, P., Gettelman,
1246 A., Haywood, J. M., Lohmann, U., Malavelle, F., Mauritsen, T., McCoy, D. T., Myhre, G.,
1247 Mülmstädt, J., Neubauer, D., Possner, A., Rugenstein, M., Sato, Y., Schulz, M., Schwartz, S. E.,
1248 Sourdeval, O., Storelvmo, T., Toll, V., Winker, D., and Stevens, B.: Bounding Global Aerosol
1249 Radiative Forcing of Climate Change, *Reviews of Geophysics*, 58, e2019RG000660,
1250 <https://doi.org/10.1029/2019RG000660>, 2020.
- 1251 Boucher, O., Randall, D., Artaxo, P., Bretherton, C., Feingold, G., Forster, P., Kerminen, V.-M.,
1252 Kondo, Y., Liao, H., Lohmann, U., Rasch, P., Satheesh, S. K., Sherwood, S., Stevens, B., Zhang, X.
1253 Y., Stocker, T. F., Qin, D., Plattner, G.-K., Tignor, M., Allen, S. K., Boschung, J., Nauels, A., Xia, Y.,
1254 Bex, V., and Midgley, P. M.: Clouds and Aerosols. In: *Climate Change 2013: The Physical Science*
1255 *Basis. Contribution of Working Group I to the Fifth Assessment Report of the Intergovernmental Panel*
1256 *on Climate Change*, Cambridge University Press, 2013.
- 1257 Canagaratna, M. r., Jayne, J. t., Jimenez, J. l., Allan, J. d., Alfarra, M. r., Zhang, Q., Onasch, T. b.,
1258 Drewnick, F., Coe, H., Middlebrook, A., Delia, A., Williams, L. r., Trimborn, A. m., Northway, M. j.,
1259 DeCarlo, P. f., Kolb, C. e., Davidovits, P., and Worsnop, D. r.: Chemical and microphysical
1260 characterization of ambient aerosols with the aerodyne aerosol mass spectrometer, *Mass*
1261 *Spectrometry Reviews*, 26, 185–222, <https://doi.org/10.1002/mas.20115>, 2007.

- 1262 Cappa, C. D.: A model of aerosol evaporation kinetics in a thermodenuder, *Atmos. Meas. Tech.*, 3,
1263 579–592, <https://doi.org/10.5194/amt-3-579-2010>, 2010.
- 1264 Cappa, C. D. and Jimenez, J. L.: Quantitative estimates of the volatility of ambient organic aerosol,
1265 *Atmos. Chem. Phys.*, 10, 5409–5424, <https://doi.org/10.5194/acp-10-5409-2010>, 2010.
- 1266 Carslaw, K. S., Lee, L. A., Reddington, C. L., Pringle, K. J., Rap, A., Forster, P. M., Mann, G. W.,
1267 Spracklen, D. V., Woodhouse, M. T., Regayre, L. A., and Pierce, J. R.: Large contribution of natural
1268 aerosols to uncertainty in indirect forcing, *Nature*, 503, 67–71, <https://doi.org/10.1038/nature12674>,
1269 2013.
- 1270 Cerully, K. M., Raatikainen, T., Lance, S., Tkacik, D., Tiitta, P., Petäjä, T., Ehn, M., Kulmala, M.,
1271 Worsnop, D. R., Laaksonen, A., Smith, J. N., and Nenes, A.: Aerosol hygroscopicity and CCN
1272 activation kinetics in a boreal forest environment during the 2007 EUCAARI campaign, *Atmospheric
1273 Chemistry and Physics*, 11, 12369–12386, <https://doi.org/10.5194/acp-11-12369-2011>, 2011.
- 1274 Connolly, P. J., Topping, D. O., Malavelle, F., and McFiggans, G.: A parameterisation for the
1275 activation of cloud drops including the effects of semi-volatile organics, *Atmos. Chem. Phys.*, 14,
1276 2289–2302, <https://doi.org/10.5194/acp-14-2289-2014>, 2014.
- 1277 Crooks, M., Connolly, P., and McFiggans, G.: A parameterisation for the co-condensation of semi-
1278 volatile organics into multiple aerosol particle modes, *Geosci. Model Dev.*, 11, 3261–3278,
1279 <https://doi.org/10.5194/gmd-11-3261-2018>, 2018.
- 1280 Dada, L., Paasonen, P., Nieminen, T., Buenrostro Mazon, S., Kontkanen, J., Peräkylä, O., Lehtipalo,
1281 K., Hussein, T., Petäjä, T., Kerminen, V.-M., Bäck, J., and Kulmala, M.: Long-term analysis of clear-
1282 sky new particle formation events and nonevents in Hyytiälä, *Atmos. Chem. Phys.*, 17, 6227–6241,
1283 <https://doi.org/10.5194/acp-17-6227-2017>, 2017.
- 1284 Daumit, K. E., Kessler, S. H., and Kroll, J. H.: Average chemical properties and potential formation
1285 pathways of highly oxidized organic aerosol, *Faraday Discuss.*, 165, 181–202,
1286 <https://doi.org/10.1039/C3FD00045A>, 2013.
- 1287 Donahue, N. M., Robinson, A. L., Stanier, C. O., and Pandis, S. N.: Coupled Partitioning, Dilution, and
1288 Chemical Aging of Semivolatile Organics, *Environ. Sci. Technol.*, 40, 2635–2643,
1289 <https://doi.org/10.1021/es052297c>, 2006.
- 1290 Donahue, N. M., Epstein, S. A., Pandis, S. N., and Robinson, A. L.: A two-dimensional volatility basis
1291 set: 1. organic-aerosol mixing thermodynamics, *Atmos. Chem. Phys.*, 11, 3303–3318,
1292 <https://doi.org/10.5194/acp-11-3303-2011>, 2011.
- 1293 Epstein, S. A., Riipinen, I., and Donahue, N. M.: A Semiempirical Correlation between Enthalpy of
1294 Vaporization and Saturation Concentration for Organic Aerosol, *Environ. Sci. Technol.*, 44, 743–748,
1295 <https://doi.org/10.1021/es902497z>, 2010.
- 1296 Forster, P., Storelvmo, T., Armour, K., Collins, W., Dufresne, J.-L., Frame, D., Lunt, D. J., Mauritsen,
1297 T., Palmer, M. D., Watanabe, M., Wild, M., and Zhang, H.: The Earth's energy budget, climate
1298 feedbacks, and climate sensitivity, in: *Climate Change 2021: The Physical Science Basis. Contribution of Working Group I to the Sixth Assessment Report of the Intergovernmental Panel on
1299 Climate Change*, edited by: Masson-Delmotte, V., Zhai, P., Pirani, A., Connors, S. L., Péan, C.,
1300 Berger, S., Caud, N., Chen, Y., Goldfarb, L., Gomis, M. I., Huang, M., Leitzell, K., Lonnoy, E.,
1301 Matthews, J. B. R., Maycock, T. K., Waterfield, T., Yelekçi, Ö., Yu, R., and Zhou, B., Cambridge
1302 University Press, 2021.
- 1304 Fredenslund, A., Jones, R. L., and Prausnitz, J. M.: Group-contribution estimation of activity
1305 coefficients in nonideal liquid mixtures, *AIChE Journal*, 21, 1086–1099,
1306 <https://doi.org/10.1002/aic.690210607>, 1975.

- 1307 Galloway, J. N., Likens, G. E., Keene, W. C., and Miller, J. M.: The composition of precipitation in
 1308 remote areas of the world, *Journal of Geophysical Research: Oceans*, 87, 8771–8786,
 1309 <https://doi.org/10.1029/JC087iC11p08771>, 1982.
- 1310 Graham, E. L., Wu, C., Bell, D. M., Bertrand, A., Haslett, S. L., Baltensperger, U., El Haddad, I.,
 1311 Krejci, R., Riipinen, I., and Mohr, C.: Volatility of aerosol particles from NO₃ oxidation of various
 1312 biogenic organic precursors, *EGUsphere*, 1–22, <https://doi.org/10.5194/egusphere-2022-1043>, 2022.
- 1313 Guenther, A., Hewitt, C. N., Erickson, D., Fall, R., Geron, C., Graedel, T., Harley, P., Klinger, L.,
 1314 Lerdau, M., McKay, W. A., Pierce, T., Scholes, B., Steinbrecher, R., Tallamraju, R., Taylor, J., and
 1315 Zimmerman, P.: A global model of natural volatile organic compound emissions, *Journal of*
 1316 *Geophysical Research: Atmospheres*, 100, 8873–8892, <https://doi.org/10.1029/94JD02950>, 1995.
- 1317 Guenther, A. B., Zimmerman, P. R., Harley, P. C., Monson, R. K., and Fall, R.: Isoprene and
 1318 monoterpene emission rate variability: Model evaluations and sensitivity analyses, *Journal of*
 1319 *Geophysical Research: Atmospheres*, 98, 12609–12617, <https://doi.org/10.1029/93JD00527>, 1993.
- 1320 Gunthe, S. S., Liu, P., Panda, U., Raj, S. S., Sharma, A., Darbyshire, E., Reyes-Villegas, E., Allan, J.,
 1321 Chen, Y., Wang, X., Song, S., Pöhlker, M. L., Shi, L., Wang, Y., Kommula, S. M., Liu, T., Ravikrishna,
 1322 R., McFiggans, G., Mickley, L. J., Martin, S. T., Pöschl, U., Andreae, M. O., and Coe, H.: Enhanced
 1323 aerosol particle growth sustained by high continental chlorine emission in India, *Nat. Geosci.*, 14, 77–
 1324 84, <https://doi.org/10.1038/s41561-020-00677-x>, 2021.
- 1325 Hakola, H., Hellén, H., Hemmilä, M., Rinne, J., and Kulmala, M.: In situ measurements of volatile
 1326 organic compounds in a boreal forest, *Atmos. Chem. Phys.*, 12, 11665–11678,
 1327 <https://doi.org/10.5194/acp-12-11665-2012>, 2012.
- 1328 Hallquist, M., Wenger, J. C., Baltensperger, U., Rudich, Y., Simpson, D., Claeys, M., Dommen, J.,
 1329 Donahue, N. M., George, C., Goldstein, A. H., Hamilton, J. F., Herrmann, H., Hoffmann, T., Iinuma,
 1330 Y., Jang, M., Jenkin, M. E., Jimenez, J. L., Kiendler-Scharr, A., Maenhaut, W., McFiggans, G., Mentel,
 1331 T. F., Monod, A., Prévôt, A. S. H., Seinfeld, J. H., Surratt, J. D., Szmigielski, R., and Wildt, J.: The
 1332 formation, properties and impact of secondary organic aerosol: current and emerging issues,
 1333 *Atmospheric Chemistry and Physics*, 9, 5155–5236, <https://doi.org/10.5194/acp-9-5155-2009>, 2009.
- 1334 Hänel, G.: The role of aerosol properties during the condensational stage of cloud: A reinvestigation
 1335 of numerics and microphysics, *Beitr. Phys. Atmos.*, 60, 321–339, 1987.
- 1336 Hari, P. and Kulmala, M.: Station for Measuring Ecosystem–Atmosphere Relations (SMEAR II),
 1337 *Boreal Environ. Res.*, 10, 8, 2005.
- 1338 Hegg, D. A.: Impact of gas-phase HNO₃ and NH₃ on microphysical processes in atmospheric clouds,
 1339 *Geophysical Research Letters*, 27, 2201–2204, <https://doi.org/10.1029/1999GL011252>, 2000.
- 1340 Heikkinen, L., Äijälä, M., Riva, M., Luoma, K., Daellenbach, K., Aalto, J., Aalto, P., Aliaga, D., Aurela,
 1341 M., Keskinen, H., Makkonen, U., Rantala, P., Kulmala, M., Petäjä, T., Worsnop, D., and Ehn, M.:
 1342 Long-term sub-micrometer aerosol chemical composition in the boreal forest: inter- and intra-annual
 1343 variability, *Atmos. Chem. Phys.*, 20, 3151–3180, <https://doi.org/10.5194/acp-20-3151-2020>, 2020.
- 1344 Heikkinen, L., Äijälä, M., Daellenbach, K. R., Chen, G., Garmash, O., Aliaga, D., Graeffe, F., Rätty, M.,
 1345 Luoma, K., Aalto, P., Kulmala, M., Petäjä, T., Worsnop, D., and Ehn, M.: Eight years of sub-
 1346 micrometre organic aerosol composition data from the boreal forest characterized using a machine-
 1347 learning approach, *Atmos. Chem. Phys.*, 21, 10081–10109, [https://doi.org/10.5194/acp-21-10081-](https://doi.org/10.5194/acp-21-10081-2021)
 1348 2021, 2021.
- 1349 Hong, J., Häkkinen, S. a. K., Paramonov, M., Äijälä, M., Hakala, J., Nieminen, T., Mikkilä, J., Prisle, N.
 1350 L., Kulmala, M., Riipinen, I., Bilde, M., Kerminen, V.-M., and Petäjä, T.: Hygroscopicity, CCN and
 1351 volatility properties of submicron atmospheric aerosol in a boreal forest environment during the
 1352 summer of 2010, *Atmospheric Chemistry and Physics*, 14, 4733–4748, [https://doi.org/10.5194/acp-](https://doi.org/10.5194/acp-14-4733-2014)
 1353 14-4733-2014, 2014.

- 1354 Hoppel, W. A. and Frick, G. M.: Submicron aerosol size distributions measured over the tropical and
1355 South Pacific, *Atmospheric Environment. Part A. General Topics*, 24, 645–659,
1356 [https://doi.org/10.1016/0960-1686\(90\)90020-N](https://doi.org/10.1016/0960-1686(90)90020-N), 1990.
- 1357 Hu, D., Topping, D., and McFiggans, G.: Measured particle water uptake enhanced by co-condensing
1358 vapours, *Atmospheric Chemistry and Physics*, 18, 14925–14937, [https://doi.org/10.5194/acp-18-](https://doi.org/10.5194/acp-18-14925-2018)
1359 14925-2018, 2018.
- 1360 Huang, W., Li, H., Sarnela, N., Heikkinen, L., Tham, Y. J., Mikkilä, J., Thomas, S. J., Donahue, N. M.,
1361 Kulmala, M., and Bianchi, F.: Measurement report: Molecular composition and volatility of gaseous
1362 organic compounds in a boreal forest – from volatile organic compounds to highly oxygenated organic
1363 molecules, *Atmos. Chem. Phys.*, 21, 8961–8977, <https://doi.org/10.5194/acp-21-8961-2021>, 2021.
- 1364 Huffman, J. A., Docherty, K. S., Aiken, A. C., Cubison, M. J., Ulbrich, I. M., DeCarlo, P. F., Sueper, D.,
1365 Jayne, J. T., Worsnop, D. R., Ziemann, P. J., and Jimenez, J. L.: Chemically-resolved aerosol
1366 volatility measurements from two megacity field studies, *Atmos. Chem. Phys.*, 9, 7161–7182,
1367 <https://doi.org/10.5194/acp-9-7161-2009>, 2009a.
- 1368 Huffman, J. A., Docherty, K. S., Mohr, C., Cubison, M. J., Ulbrich, I. M., Ziemann, P. J., Onasch, T. B.,
1369 and Jimenez, J. L.: Chemically-Resolved Volatility Measurements of Organic Aerosol from Different
1370 Sources, *Environ. Sci. Technol.*, 43, 5351–5357, <https://doi.org/10.1021/es803539d>, 2009b.
- 1371 Hunter, J. F., Day, D. A., Palm, B. B., Yatavelli, R. L. N., Chan, A. W. H., Kaser, L., Cappellin, L.,
1372 Hayes, P. L., Cross, E. S., Carrasquillo, A. J., Campuzano-Jost, P., Stark, H., Zhao, Y., Hohaus, T.,
1373 Smith, J. N., Hansel, A., Karl, T., Goldstein, A. H., Guenther, A., Worsnop, D. R., Thornton, J. A.,
1374 Heald, C. L., Jimenez, J. L., and Kroll, J. H.: Comprehensive characterization of atmospheric organic
1375 carbon at a forested site, *Nature Geosci.*, 10, 748–753, <https://doi.org/10.1038/ngeo3018>, 2017.
- 1376 Hussein, T., Maso, M. D., Petäjä, T., Koponen, I. K., Paatero, P., Aalto, P. P., Hämeri, K., and
1377 Kulmala, M.: Evaluation of an automatic algorithm for fitting the particle number size distributions,
1378 *Boreal Environ. Res.*, 10, 19, 2005.
- 1379 Isaacman-VanWertz, G. and Aumont, B.: Impact of organic molecular structure on the estimation of
1380 atmospherically relevant physicochemical parameters, *Atmos. Chem. Phys.*, 21, 6541–6563,
1381 <https://doi.org/10.5194/acp-21-6541-2021>, 2021.
- 1382 Kakavas, S., Pandis, S. N., and Nenes, A.: ISORROPIA-Lite: A Comprehensive Atmospheric Aerosol
1383 Thermodynamics Module for Earth System Models, *Tellus B: Chemical and Physical Meteorology*, 74,
1384 1–23, <https://doi.org/10.16993/tellusb.33>, 2022.
- 1385 Kerminen, V.-M., Chen, X., Vakkari, V., Petäjä, T., Kulmala, M., and Bianchi, F.: Atmospheric new
1386 particle formation and growth: review of field observations, *Environ. Res. Lett.*, 13, 103003,
1387 <https://doi.org/10.1088/1748-9326/aadf3c>, 2018.
- 1388 Kim, P., Partridge, D. G., and Haywood, J.: Constraining the model representation of the aerosol life
1389 cycle in relation to sources and sinks, *EGU General Assembly 2020*, Online, 4–8 May 2020,
1390 EGU2020-21948, <https://doi.org/10.5194/egusphere-egu2020-21948>, 2020.
- 1391 Köhler, H.: The nucleus in and the growth of hygroscopic droplets, *Trans. Faraday Soc.*, 32, 1152–
1392 1161, <https://doi.org/10.1039/TF9363201152>, 1936.
- 1393 Kontkanen, J., Paasonen, P., Aalto, J., Bäck, J., Rantala, P., Petäjä, T., and Kulmala, M.: Simple
1394 proxies for estimating the concentrations of monoterpenes and their oxidation products at a boreal
1395 forest site, *Atmospheric Chemistry and Physics*, 16, 13291–13307, [https://doi.org/10.5194/acp-16-](https://doi.org/10.5194/acp-16-13291-2016)
1396 13291-2016, 2016.
- 1397 Korhonen, P., Kulmala, M., and Vesala, T.: Model simulation of the amount of soluble mass during
1398 cloud droplet formation, *Atmospheric Environment*, 30, 1773–1785, [https://doi.org/10.1016/1352-](https://doi.org/10.1016/1352-2310(95)00380-0)
1399 2310(95)00380-0, 1996.

- 1400 Kulmala, M., Laaksonen, A., Korhonen, P., Vesala, T., Ahonen, T., and Barrett, J. C.: The effect of
1401 atmospheric nitric acid vapor on cloud condensation nucleus activation, *Journal of Geophysical*
1402 *Research: Atmospheres*, 98, 22949–22958, <https://doi.org/10.1029/93JD02070>, 1993.
- 1403 Kulmala, M., Rannik, Ü., Pirjola, L., Maso, M. D., Karimäki, J., Asmi, A., Jäppinen, A., Karhu, V.,
1404 Korhonen, H., Malvikko, S.-P., Puustinen, A., Raittila, J., Romakkaniemi, S., Suni, T., Yli-Koivisto, S.,
1405 Paatero, J., Hari, P., and Vesala, T.: Characterization of atmospheric trace gas and aerosol
1406 concentrations at forest sites in southern and northern Finland using back trajectories, *Boreal Environ.*
1407 *Res.*, 5, 22, 2000.
- 1408 Kulmala, M., Suni, T., Lehtinen, K. E. J., Dal Maso, M., Boy, M., Reissell, A., Rannik, Ü., Aalto, P.,
1409 Keronen, P., Hakola, H., Bäck, J., Hoffmann, T., Vesala, T., and Hari, P.: A new feedback mechanism
1410 linking forests, aerosols, and climate, *Atmospheric Chemistry and Physics*, 4, 557–562,
1411 <https://doi.org/10.5194/acp-4-557-2004>, 2004.
- 1412 Kulmala, M., Nieminen, T., Nikandrova, A., Lehtipalo, K., Manninen, H. E., Kajos, M. K., Kolari, P.,
1413 Lauri, A., Petäjä, T., Krejci, R., Hansson, H.-C., Swietlicki, E., Lindroth, A., Christensen, T. R., Arneth,
1414 A., Hari, P., Bäck, J., Vesala, T., and Kerminen, V.-M.: CO₂-induced terrestrial climate feedback
1415 mechanism: From carbon sink to aerosol source and back, *Boreal Environ. Res.*, 19, 10, 2014.
- 1416 Kyrö, E.-M., Väänänen, R., Kerminen, V.-M., Virkkula, A., Petäjä, T., Asmi, A., Dal Maso, M.,
1417 Nieminen, T., Juhola, S., Shcherbinin, A., Riipinen, I., Lehtipalo, K., Keronen, P., Aalto, P. P., Hari, P.,
1418 and Kulmala, M.: Trends in new particle formation in eastern Lapland, Finland: effect of decreasing
1419 sulfur emissions from Kola Peninsula, *Atmos. Chem. Phys.*, 14, 4383–4396,
1420 <https://doi.org/10.5194/acp-14-4383-2014>, 2014.
- 1421 Lee, B. H., Lopez-Hilfiker, F. D., D'Ambro, E. L., Zhou, P., Boy, M., Petäjä, T., Hao, L., Virtanen, A.,
1422 and Thornton, J. A.: Semi-volatile and highly oxygenated gaseous and particulate organic compounds
1423 observed above a boreal forest canopy, *Atmos. Chem. Phys.*, 18, 11547–11562,
1424 <https://doi.org/10.5194/acp-18-11547-2018>, 2018.
- 1425 Lee, B. H., D'Ambro, E. L., Lopez-Hilfiker, F. D., Schobesberger, S., Mohr, C., Zawadowicz, M. A.,
1426 Liu, J., Shilling, J. E., Hu, W., Palm, B. B., Jimenez, J. L., Hao, L., Virtanen, A., Zhang, H., Goldstein,
1427 A. H., Pye, H. O. T., and Thornton, J. A.: Resolving Ambient Organic Aerosol Formation and Aging
1428 Pathways with Simultaneous Molecular Composition and Volatility Observations, *ACS Earth Space*
1429 *Chem.*, 4, 391–402, <https://doi.org/10.1021/acsearthspacechem.9b00302>, 2020.
- 1430 Lee, I.-Y. and Pruppacher, H. R.: A comparative study on the growth of cloud drops by condensation
1431 using an air parcel model with and without entrainment, *PAGEOPH*, 115, 523–545,
1432 <https://doi.org/10.1007/BF00876119>, 1977.
- 1433 Li, Y., Pöschl, U., and Shiraiwa, M.: Molecular corridors and parameterizations of volatility in the
1434 chemical evolution of organic aerosols, *Atmos. Chem. Phys.*, 16, 3327–3344,
1435 <https://doi.org/10.5194/acp-16-3327-2016>, 2016.
- 1436 Lohmann, U. and Feichter, J.: Global indirect aerosol effects: a review, *Atmos. Chem. Phys.*, 23,
1437 2005.
- 1438 Lopez-Hilfiker, F. D., Mohr, C., Ehn, M., Rubach, F., Kleist, E., Wildt, J., Mentel, T. F., Lutz, A.,
1439 Hallquist, M., Worsnop, D., and Thornton, J. A.: A novel method for online analysis of gas and particle
1440 composition: description and evaluation of a Filter Inlet for Gases and AEROSols (FIGAERO), *Atmos.*
1441 *Meas. Tech.*, 7, 983–1001, <https://doi.org/10.5194/amt-7-983-2014>, 2014.
- 1442 Lopez-Hilfiker, F. D., Mohr, C., Ehn, M., Rubach, F., Kleist, E., Wildt, J., Mentel, T. F., Carrasquillo, A.
1443 J., Daumit, K. E., Hunter, J. F., Kroll, J. H., Worsnop, D. R., and Thornton, J. A.: Phase partitioning
1444 and volatility of secondary organic aerosol components formed from α -pinene ozonolysis and OH
1445 oxidation: the importance of accretion products and other low volatility compounds, *Atmospheric*
1446 *Chemistry and Physics*, 15, 7765–7776, <https://doi.org/10.5194/acp-15-7765-2015>, 2015.

- 1447 Lowe, S. J.: Modelling the effects of organic aerosol phase partitioning processes on cloud formation,
1448 PhD thesis, Stockholm University, Faculty of Science, Department of Environmental Science,
1449 Stockholm, Sweden, 2020.
- 1450 Lowe, S. J., Partridge, D. G., Davies, J. F., Wilson, K. R., Topping, D., and Riipinen, I.: Key drivers of
1451 cloud response to surface-active organics, *Nat Commun*, 10, 5214, [https://doi.org/10.1038/s41467-](https://doi.org/10.1038/s41467-019-12982-0)
1452 019-12982-0, 2019.
- 1453 Luoma, K.: AEROSOL OPTICAL PROPERTIES, BLACK CARBON AND THEIR SPATIO-TEMPORAL
1454 VARIATION, PhD thesis, University of Helsinki, 2021.
- 1455 Lutz, A., Mohr, C., Le Breton, M., Lopez-Hilfiker, F. D., Priestley, M., Thornton, J. A., and Hallquist,
1456 M.: Gas to Particle Partitioning of Organic Acids in the Boreal Atmosphere, *ACS Earth Space Chem.*,
1457 3, 1279–1287, <https://doi.org/10.1021/acsearthspacechem.9b00041>, 2019.
- 1458 Mann, G. W., Carslaw, K. S., Spracklen, D. V., Ridley, D. A., Manktelow, P. T., Chipperfield, M. P.,
1459 Pickering, S. J., and Johnson, C. E.: Description and evaluation of GLOMAP-mode: a modal global
1460 aerosol microphysics model for the UKCA composition-climate model, *Geoscientific Model*
1461 *Development*, 3, 519–551, <https://doi.org/10.5194/gmd-3-519-2010>, 2010.
- 1462 Mikhailov, E. F., Mironova, S., Mironov, G., Vlasenko, S., Panov, A., Chi, X., Walter, D., Carbone, S.,
1463 Artaxo, P., Heimann, M., Lavric, J., Pöschl, U., and Andreae, M. O.: Long-term measurements (2010–
1464 2014) of carbonaceous aerosol and carbon monoxide at the Zotino Tall Tower Observatory (ZOTTO)
1465 in central Siberia, *Atmos. Chem. Phys.*, 17, 14365–14392, [https://doi.org/10.5194/acp-17-14365-](https://doi.org/10.5194/acp-17-14365-2017)
1466 2017, 2017.
- 1467 Millet, D. B., Baasandorj, M., Farmer, D. K., Thornton, J. A., Baumann, K., Brophy, P., Chaliyakunnel,
1468 S., de Gouw, J. A., Graus, M., Hu, L., Koss, A., Lee, B. H., Lopez-Hilfiker, F. D., Neuman, J. A.,
1469 Paulot, F., Peischl, J., Pollack, I. B., Ryerson, T. B., Warneke, C., Williams, B. J., and Xu, J.: A large
1470 and ubiquitous source of atmospheric formic acid, *Atmos. Chem. Phys.*, 15, 6283–6304,
1471 <https://doi.org/10.5194/acp-15-6283-2015>, 2015.
- 1472 Mohr, C., Lopez-Hilfiker, F. D., Yli-Juuti, T., Heitto, A., Lutz, A., Hallquist, M., D'Ambro, E. L.,
1473 Rissanen, M. P., Hao, L., Schobesberger, S., Kulmala, M., Mauldin III, R. L., Makkonen, U., Sipilä, M.,
1474 Petäjä, T., and Thornton, J. A.: Ambient observations of dimers from terpene oxidation in the gas
1475 phase: Implications for new particle formation and growth, *Geophysical Research Letters*, 44, 2958–
1476 2966, <https://doi.org/10.1002/2017GL072718>, 2017.
- 1477 Mohr, C., Thornton, J. A., Heitto, A., Lopez-Hilfiker, F. D., Lutz, A., Riipinen, I., Hong, J., Donahue, N.
1478 M., Hallquist, M., Petäjä, T., Kulmala, M., and Yli-Juuti, T.: Molecular identification of organic vapors
1479 driving atmospheric nanoparticle growth, *Nat Commun*, 10, 4442, [https://doi.org/10.1038/s41467-019-](https://doi.org/10.1038/s41467-019-12473-2)
1480 12473-2, 2019.
- 1481 Mulcahy, J. P., Johnson, C., Jones, C. G., Povey, A. C., Scott, C. E., Sellar, A., Turnock, S. T.,
1482 Woodhouse, M. T., Abraham, N. L., Andrews, M. B., Bellouin, N., Browse, J., Carslaw, K. S., Dalvi,
1483 M., Folberth, G. A., Glover, M., Grosvenor, D. P., Hardacre, C., Hill, R., Johnson, B., Jones, A.,
1484 Kipling, Z., Mann, G., Mollard, J., O'Connor, F. M., Palmiéri, J., Reddington, C., Rumbold, S. T.,
1485 Richardson, M., Schutgens, N. A. J., Stier, P., Stringer, M., Tang, Y., Walton, J., Woodward, S., and
1486 Yool, A.: Description and evaluation of aerosol in UKESM1 and HadGEM3-GC3.1 CMIP6 historical
1487 simulations, *Geosci. Model Dev.*, 13, 6383–6423, <https://doi.org/10.5194/gmd-13-6383-2020>, 2020.
- 1488 Murphy, B. N., Julin, J., Riipinen, I., and Ekman, A. M. L.: Organic aerosol processing in tropical deep
1489 convective clouds: Development of a new model (CRM-ORG) and implications for sources of particle
1490 number, *Journal of Geophysical Research: Atmospheres*, 120, 10,441-10,464,
1491 <https://doi.org/10.1002/2015JD023551>, 2015.
- 1492 Ng, N. L., Herndon, S. C., Trimborn, A., Canagaratna, M. R., Croteau, P. L., Onasch, T. B., Sueper,
1493 D., Worsnop, D. R., Zhang, Q., Sun, Y. L., and Jayne, J. T.: An Aerosol Chemical Speciation Monitor
1494 (ACSM) for Routine Monitoring of the Composition and Mass Concentrations of Ambient Aerosol,

- 1495 Aerosol Science and Technology, 45, 780–794, <https://doi.org/10.1080/02786826.2011.560211>,
1496 2011.
- 1497 Nieminen, T., Asmi, A., Maso, M. D., Aalto, P. P., Keronen, P., Petäjä, T., Kulmala, M., and Kerminen,
1498 V.-M.: Trends in atmospheric new-particle formation: 16 years of observations in a boreal-forest
1499 environment, *Boreal Environ. Res.*, 19, 191–214, 2014.
- 1500 NIST Chemistry WebBook: <https://webbook.nist.gov/cgi/cbook.cgi?ID=C64186&Mask=4>, last access:
1501 8 November 2022.
- 1502 Ovadnevaite, J., Zuend, A., Laaksonen, A., Sanchez, K. J., Roberts, G., Ceburnis, D., Decesari, S.,
1503 Rinaldi, M., Hodas, N., Facchini, M. C., Seinfeld, J. H., and O’ Dowd, C.: Surface tension prevails over
1504 solute effect in organic-influenced cloud droplet activation, *Nature*, 546, 637–641,
1505 <https://doi.org/10.1038/nature22806>, 2017.
- 1506 Paasonen, P., Asmi, A., Petäjä, T., Kajos, M. K., Äijälä, M., Junninen, H., Holst, T., Abbatt, J. P. D.,
1507 Arneth, A., Birmili, W., van der Gon, H. D., Hamed, A., Hoffer, A., Laakso, L., Laaksonen, A., Richard
1508 Leitch, W., Plass-Dülmer, C., Pryor, S. C., Räsänen, P., Swietlicki, E., Wiedensohler, A., Worsnop,
1509 D. R., Kerminen, V.-M., and Kulmala, M.: Warming-induced increase in aerosol number concentration
1510 likely to moderate climate change, *Nature Geosci.*, 6, 438–442, <https://doi.org/10.1038/ngeo1800>,
1511 2013.
- 1512 Pankow, J. F., Seinfeld, J. H., Asher, W. E., and Erdakos, G. B.: Modeling the Formation of
1513 Secondary Organic Aerosol. 1. Application of Theoretical Principles to Measurements Obtained in the
1514 α -Pinene/, β -Pinene/, Sabinene/, Δ 3-Carene/, and Cyclohexene/Ozone Systems, *Environ. Sci.*
1515 *Technol.*, 35, 1164–1172, <https://doi.org/10.1021/es001321d>, 2001.
- 1516 Paramonov, M., Aalto, P. P., Asmi, A., Prisle, N., Kerminen, V.-M., Kulmala, M., and Petäjä, T.: The
1517 analysis of size-segregated cloud condensation nuclei counter (CCNC) data and its implications for
1518 cloud droplet activation, *Atmos. Chem. Phys.*, 13, 10285–10301, <https://doi.org/10.5194/acp-13-10285-2013>, 2013.
- 1520 Paramonov, M., Kerminen, V.-M., Gysel, M., Aalto, P. P., Andreae, M. O., Asmi, E., Baltensperger, U.,
1521 Bougiatioti, A., Brus, D., Frank, G. P., Good, N., Gunthe, S. S., Hao, L., Irwin, M., Jaatinen, A.,
1522 Jurányi, Z., King, S. M., Kortelainen, A., Kristensson, A., Lihavainen, H., Kulmala, M., Lohmann, U.,
1523 Martin, S. T., McFiggans, G., Mihalopoulos, N., Nenes, A., O’Dowd, C. D., Ovadnevaite, J., Petäjä, T.,
1524 Pöschl, U., Roberts, G. C., Rose, D., Svenningsson, B., Swietlicki, E., Weingartner, E., Whitehead, J.,
1525 Wiedensohler, A., Wittbom, C., and Sierau, B.: A synthesis of cloud condensation nuclei counter
1526 (CCNC) measurements within the EUCAARI network, *Atmospheric Chemistry and Physics*, 15,
1527 12211–12229, <https://doi.org/10.5194/acp-15-12211-2015>, 2015.
- 1528 Partridge, D. G., Vrugt, J. A., Tunved, P., Ekman, A. M. L., Gorea, D., and Sorooshian, A.: Inverse
1529 modeling of cloud-aerosol interactions – Part 1: Detailed response surface analysis, *Atmos. Chem.*
1530 *Phys.*, 11, 7269–7287, <https://doi.org/10.5194/acp-11-7269-2011>, 2011.
- 1531 Partridge, D. G., Vrugt, J. A., Tunved, P., Ekman, A. M. L., Struthers, H., and Sorooshian, A.: Inverse
1532 modelling of cloud-aerosol interactions – Part 2: Sensitivity tests on liquid phase clouds using a
1533 Markov chain Monte Carlo based simulation approach, *Atmos. Chem. Phys.*, 12, 2823–2847,
1534 <https://doi.org/10.5194/acp-12-2823-2012>, 2012.
- 1535 Petäjä, T., O’Connor, E. J., Moisseev, D., Sinclair, V. A., Manninen, A. J., Väänänen, R., Lerber, A.
1536 von, Thornton, J. A., Nicoll, K., Petersen, W., Chandrasekar, V., Smith, J. N., Winkler, P. M., Krüger,
1537 O., Hakola, H., Timonen, H., Brus, D., Laurila, T., Asmi, E., Riekkola, M.-L., Mona, L., Massoli, P.,
1538 Engelmann, R., Komppula, M., Wang, J., Kuang, C., Bäck, J., Virtanen, A., Levula, J., Ritsche, M.,
1539 and Hickmon, N.: BAECC: A Field Campaign to Elucidate the Impact of Biogenic Aerosols on Clouds
1540 and Climate, *Bulletin of the American Meteorological Society*, 97, 1909–1928,
1541 <https://doi.org/10.1175/BAMS-D-14-00199.1>, 2016.
- 1542 Petäjä, T., Tabakova, K., Manninen, A., Ezhova, E., O’Connor, E., Moisseev, D., Sinclair, V. A.,
1543 Backman, J., Levula, J., Luoma, K., Virkkula, A., Paramonov, M., Rätty, M., Äijälä, M., Heikkinen, L.,

- 1544 Ehn, M., Sipilä, M., Yli-Juuti, T., Virtanen, A., Ritsche, M., Hickmon, N., Pulik, G., Rosenfeld, D.,
 1545 Worsnop, D. R., Bäck, J., Kulmala, M., and Kerminen, V.-M.: Influence of biogenic emissions from
 1546 boreal forests on aerosol–cloud interactions, *Nat. Geosci.*, 15, 42–47, [https://doi.org/10.1038/s41561-](https://doi.org/10.1038/s41561-021-00876-0)
 1547 021-00876-0, 2022.
- 1548 Petters, M. D. and Kreidenweis, S. M.: A single parameter representation of hygroscopic growth and
 1549 cloud condensation nucleus activity – Part 2: Including solubility, *Atmos. Chem. Phys.*, 7, 2008.
- 1550 Pruppacher, H. R. and Klett, J. D.: *Microphysics of Clouds and Precipitation*, Springer Netherlands,
 1551 Dordrecht, <https://doi.org/10.1007/978-0-306-48100-0>, 1997.
- 1552 Ridley, J. K., Blockley, E. W., Keen, A. B., Rae, J. G. L., West, A. E., and Schroeder, D.: The sea ice
 1553 model component of HadGEM3-GC3.1, *Geoscientific Model Development*, 11, 713–723,
 1554 <https://doi.org/10.5194/gmd-11-713-2018>, 2018.
- 1555 Roelofs, G. J. H.: Drop size dependent sulfate distribution in a growing cloud, *J Atmos Chem*, 14,
 1556 109–118, <https://doi.org/10.1007/BF00115227>, 1992a.
- 1557 Roelofs, G. J. H.: On the drop and aerosol size dependence of aqueous sulfate formation in a
 1558 continental cumulus cloud, *Atmospheric Environment. Part A. General Topics*, 26, 2309–2321,
 1559 [https://doi.org/10.1016/0960-1686\(92\)90362-O](https://doi.org/10.1016/0960-1686(92)90362-O), 1992b.
- 1560 Roelofs, G.-J. and Jongen, S.: A model study of the influence of aerosol size and chemical properties
 1561 on precipitation formation in warm clouds, *J. Geophys. Res.*, 109,
 1562 <https://doi.org/10.1029/2004JD004779>, 2004.
- 1563 Romakkaniemi, S., Kokkola, H., and Laaksonen, A.: Parameterization of the nitric acid effect on CCN
 1564 activation, *Atmospheric Chemistry and Physics*, 5, 879–885, <https://doi.org/10.5194/acp-5-879-2005>,
 1565 2005.
- 1566 Ruehl, C. R., Chuang, P. Y., Nenes, A., Cappa, C. D., Kolesar, K. R., and Goldstein, A. H.: Strong
 1567 evidence of surface tension reduction in microscopic aqueous droplets, *Geophysical Research*
 1568 *Letters*, 39, <https://doi.org/10.1029/2012GL053706>, 2012.
- 1569 Ruehl, C. R., Davies, J. F., and Wilson, K. R.: An interfacial mechanism for cloud droplet formation on
 1570 organic aerosols, *Science*, 351, 1447–1450, <https://doi.org/10.1126/science.aad4889>, 2016.
- 1571 Schobesberger, S., Lopez-Hilfiker, F. D., Taipale, D., Millet, D. B., D'Ambro, E. L., Rantala, P.,
 1572 Mammarella, I., Zhou, P., Wolfe, G. M., Lee, B. H., Boy, M., and Thornton, J. A.: High upward fluxes
 1573 of formic acid from a boreal forest canopy, *Geophysical Research Letters*, 43, 9342–9351,
 1574 <https://doi.org/10.1002/2016GL069599>, 2016.
- 1575 Scott, C. E., Arnold, S. R., Monks, S. A., Asmi, A., Paasonen, P., and Spracklen, D. V.: Substantial
 1576 large-scale feedbacks between natural aerosols and climate, *Nature Geosci.*, 11, 44–48,
 1577 <https://doi.org/10.1038/s41561-017-0020-5>, 2018.
- 1578 Sellar, A. A., Jones, C. G., Mulcahy, J. P., Tang, Y., Yool, A., Wiltshire, A., O'Connor, F. M., Stringer,
 1579 M., Hill, R., Palmieri, J., Woodward, S., de Mora, L., Kuhlbrodt, T., Rumbold, S. T., Kelley, D. I., Ellis,
 1580 R., Johnson, C. E., Walton, J., Abraham, N. L., Andrews, M. B., Andrews, T., Archibald, A. T.,
 1581 Berthou, S., Burke, E., Blockley, E., Carslaw, K., Dalvi, M., Edwards, J., Folberth, G. A., Gedney, N.,
 1582 Griffiths, P. T., Harper, A. B., Hendry, M. A., Hewitt, A. J., Johnson, B., Jones, A., Jones, C. D.,
 1583 Keeble, J., Liddicoat, S., Morgenstern, O., Parker, R. J., Predoi, V., Robertson, E., Siahann, A.,
 1584 Smith, R. S., Swaminathan, R., Woodhouse, M. T., Zeng, G., and Zerroukat, M.: UKESM1:
 1585 Description and Evaluation of the U.K. Earth System Model, *Journal of Advances in Modeling Earth*
 1586 *Systems*, 11, 4513–4558, <https://doi.org/10.1029/2019MS001739>, 2019.
- 1587 Sellar, A. A., Walton, J., Jones, C. G., Wood, R., Abraham, N. L., Andrejczuk, M., Andrews, M. B.,
 1588 Andrews, T., Archibald, A. T., de Mora, L., Dyson, H., Elkington, M., Ellis, R., Florek, P., Good, P.,
 1589 Gohar, L., Haddad, S., Hardiman, S. C., Hogan, E., Iwi, A., Jones, C. D., Johnson, B., Kelley, D. I.,
 1590 Kettleborough, J., Knight, J. R., Köhler, M. O., Kuhlbrodt, T., Liddicoat, S., Linova-Pavlova, I.,

- 1591 Mizieliński, M. S., Morgenstern, O., Mulcahy, J., Neininger, E., O'Connor, F. M., Petrie, R., Ridley, J.,
 1592 Rioual, J.-C., Roberts, M., Robertson, E., Rumbold, S., Seddon, J., Shepherd, H., Shim, S.,
 1593 Stephens, A., Teixeira, J. C., Tang, Y., Williams, J., Wiltshire, A., and Griffiths, P. T.: Implementation
 1594 of U.K. Earth System Models for CMIP6, *Journal of Advances in Modeling Earth Systems*, 12,
 1595 e2019MS001946, <https://doi.org/10.1029/2019MS001946>, 2020.
- 1596 Shrivastava, M., Cappa, C. D., Fan, J., Goldstein, A. H., Guenther, A. B., Jimenez, J. L., Kuang, C.,
 1597 Laskin, A., Martin, S. T., Ng, N. L., Petaja, T., Pierce, J. R., Rasch, P. J., Roldin, P., Seinfeld, J. H.,
 1598 Shilling, J., Smith, J. N., Thornton, J. A., Volkamer, R., Wang, J., Worsnop, D. R., Zaveri, R. A.,
 1599 Zelenyuk, A., and Zhang, Q.: Recent advances in understanding secondary organic aerosol:
 1600 Implications for global climate forcing, *Reviews of Geophysics*, 55, 509–559,
 1601 <https://doi.org/10.1002/2016RG000540>, 2017.
- 1602 Sihto, S.-L., Mikkilä, J., Vanhanen, J., Ehn, M., Liao, L., Lehtipalo, K., Aalto, P. P., Duplissy, J.,
 1603 Petäjä, T., Kerminen, V.-M., Boy, M., and Kulmala, M.: Seasonal variation of CCN concentrations and
 1604 aerosol activation properties in boreal forest, *Atmospheric Chemistry and Physics*, 11, 13269–13285,
 1605 <https://doi.org/10.5194/acp-11-13269-2011>, 2011.
- 1606 Sporre, M. K., Blichner, S. M., Karset, I. H. H., Makkonen, R., and Berntsen, T. K.: BVOC–aerosol–
 1607 climate feedbacks investigated using NorESM, *Atmospheric Chemistry and Physics*, 19, 4763–4782,
 1608 <https://doi.org/10.5194/acp-19-4763-2019>, 2019.
- 1609 Sporre, M. K., Blichner, S. M., Schrödner, R., Karset, I. H. H., Berntsen, T. K., van Noije, T., Bergman,
 1610 T., O'Donnell, D., and Makkonen, R.: Large difference in aerosol radiative effects from BVOC-SOA
 1611 treatment in three Earth system models, *Atmospheric Chemistry and Physics*, 20, 8953–8973,
 1612 <https://doi.org/10.5194/acp-20-8953-2020>, 2020.
- 1613 Spracklen, D. V., Bonn, B., and Carslaw, K. S.: Boreal forests, aerosols and the impacts on clouds
 1614 and climate, *Philosophical Transactions of the Royal Society A: Mathematical, Physical and
 1615 Engineering Sciences*, 366, 4613–4626, <https://doi.org/10.1098/rsta.2008.0201>, 2008.
- 1616 Storkey, D., Blaker, A. T., Mathiot, P., Megann, A., Aksenov, Y., Blockley, E. W., Calvert, D., Graham,
 1617 T., Hewitt, H. T., Hyder, P., Kuhlbrodt, T., Rae, J. G. L., and Sinha, B.: UK Global Ocean GO6 and
 1618 GO7: a traceable hierarchy of model resolutions, *Geoscientific Model Development*, 11, 3187–3213,
 1619 <https://doi.org/10.5194/gmd-11-3187-2018>, 2018.
- 1620 Thornhill, G., Collins, W., Olivie, D., Skeie, R. B., Archibald, A., Bauer, S., Checa-Garcia, R., Fiedler,
 1621 S., Folberth, G., Gjernmunden, A., Horowitz, L., Lamarque, J.-F., Michou, M., Mulcahy, J., Nabat, P.,
 1622 Naik, V., O'Connor, F. M., Paulot, F., Schulz, M., Scott, C. E., Séférian, R., Smith, C., Takemura, T.,
 1623 Tilmes, S., Tsigaridis, K., and Weber, J.: Climate-driven chemistry and aerosol feedbacks in CMIP6
 1624 Earth system models, *Atmospheric Chemistry and Physics*, 21, 1105–1126,
 1625 <https://doi.org/10.5194/acp-21-1105-2021>, 2021.
- 1626 Thornton, J. A., Mohr, C., Schobesberger, S., D'Ambro, E. L., Lee, B. H., and Lopez-Hilfiker, F. D.:
 1627 Evaluating Organic Aerosol Sources and Evolution with a Combined Molecular Composition and
 1628 Volatility Framework Using the Filter Inlet for Gases and Aerosols (FIGAERO), *Acc. Chem. Res.*, 53,
 1629 1415–1426, <https://doi.org/10.1021/acs.accounts.0c00259>, 2020.
- 1630 Topping, D., Connolly, P., and McFiggans, G.: Cloud droplet number enhanced by co-condensation of
 1631 organic vapours, *Nature Geosci*, 6, 443–446, <https://doi.org/10.1038/ngeo1809>, 2013.
- 1632 Topping, D. O. and McFiggans, G.: Tight coupling of particle size, number and composition in
 1633 atmospheric cloud droplet activation, *Atmospheric Chemistry and Physics*, 12, 3253–3260,
 1634 <https://doi.org/10.5194/acp-12-3253-2012>, 2012.
- 1635 Tunved, P., Hansson, H.-C., Kerminen, V.-M., Ström, J., Maso, M. D., Lihavainen, H., Viisanen, Y.,
 1636 Aalto, P. P., Komppula, M., and Kulmala, M.: High Natural Aerosol Loading over Boreal Forests,
 1637 *Science*, 312, 261–263, <https://doi.org/10.1126/science.1123052>, 2006.

- 1638 Turnock, S. T., Allen, R. J., Andrews, M., Bauer, S. E., Deushi, M., Emmons, L., Good, P., Horowitz,
1639 L., John, J. G., Michou, M., Nabat, P., Naik, V., Neubauer, D., O'Connor, F. M., Olivie, D., Oshima, N.,
1640 Schulz, M., Sellar, A., Shim, S., Takemura, T., Tilmes, S., Tsigaridis, K., Wu, T., and Zhang, J.:
1641 Historical and future changes in air pollutants from CMIP6 models, *Atmospheric Chemistry and*
1642 *Physics*, 20, 14547–14579, <https://doi.org/10.5194/acp-20-14547-2020>, 2020.
- 1643 Twomey, S.: Pollution and the planetary albedo, *Atmospheric Environment* (1967), 8, 1251–1256,
1644 [https://doi.org/10.1016/0004-6981\(74\)90004-3](https://doi.org/10.1016/0004-6981(74)90004-3), 1974.
- 1645 Twomey, S.: The Influence of Pollution on the Shortwave Albedo of Clouds, *Journal of the*
1646 *Atmospheric Sciences*, 34, 1149–1152, [https://doi.org/10.1175/1520-0469\(1977\)034<1149:TIOPO>2.0.CO;2](https://doi.org/10.1175/1520-0469(1977)034<1149:TIOPO>2.0.CO;2), 1977.
- 1648 Vehkamäki, H., Kulmala, M., Napari, I., Lehtinen, K. E. J., Timmreck, C., Noppel, M., and Laaksonen,
1649 A.: An improved parameterization for sulfuric acid–water nucleation rates for tropospheric and
1650 stratospheric conditions, *Journal of Geophysical Research: Atmospheres*, 107, AAC 3-1-AAC 3-10,
1651 <https://doi.org/10.1029/2002JD002184>, 2002.
- 1652 Walters, D., Boutle, I., Brooks, M., Melvin, T., Stratton, R., Vosper, S., Wells, H., Williams, K., Wood,
1653 N., Allen, T., Bushell, A., Copsey, D., Earnshaw, P., Edwards, J., Gross, M., Hardiman, S., Harris, C.,
1654 Heming, J., Klingaman, N., Levine, R., Manners, J., Martin, G., Milton, S., Mittermaier, M., Morcrette,
1655 C., Riddick, T., Roberts, M., Sanchez, C., Selwood, P., Stirling, A., Smith, C., Suri, D., Tennant, W.,
1656 Vidale, P. L., Wilkinson, J., Willett, M., Woolnough, S., and Xavier, P.: The Met Office Unified Model
1657 Global Atmosphere 6.0/6.1 and JULES Global Land 6.0/6.1 configurations, *Geoscientific Model*
1658 *Development*, 10, 1487–1520, <https://doi.org/10.5194/gmd-10-1487-2017>, 2017.
- 1659 Wang, Y., Chen, Y., Wu, Z., Shang, D., Bian, Y., Du, Z., Schmitt, S. H., Su, R., Gkatzelis, G. I.,
1660 Schlag, P., Hohaus, T., Voliotis, A., Lu, K., Zeng, L., Zhao, C., Alfarra, M. R., McFiggans, G.,
1661 Wiedensohler, A., Kiendler-Scharr, A., Zhang, Y., and Hu, M.: Mutual promotion between aerosol
1662 particle liquid water and particulate nitrate enhancement leads to severe nitrate-dominated particulate
1663 matter pollution and low visibility, *Atmospheric Chemistry and Physics*, 20, 2161–2175,
1664 <https://doi.org/10.5194/acp-20-2161-2020>, 2020.
- 1665 West, R. E. L., Stier, P., Jones, A., Johnson, C. E., Mann, G. W., Bellouin, N., Partridge, D. G., and
1666 Kipling, Z.: The importance of vertical velocity variability for estimates of the indirect aerosol effects,
1667 *Atmos. Chem. Phys.*, 14, 6369–6393, <https://doi.org/10.5194/acp-14-6369-2014>, 2014.
- 1668 Williams, J., Crowley, J., Fischer, H., Harder, H., Martinez, M., Petäjä, T., Rinne, J., Bäck, J., Boy, M.,
1669 Dal Maso, M., Hakala, J., Kajos, M., Keronen, P., Rantala, P., Aalto, J., Aaltonen, H., Paatero, J.,
1670 Vesala, T., Hakola, H., Levula, J., Pohja, T., Herrmann, F., Auld, J., Mesarchaki, E., Song, W.,
1671 Yassaa, N., Nölscher, A., Johnson, A. M., Custer, T., Sinha, V., Thieser, J., Pouvesle, N., Taraborrelli,
1672 D., Tang, M. J., Bozem, H., Hosaynali-Beygi, Z., Axinte, R., Oswald, R., Novelli, A., Kubistin, D.,
1673 Hens, K., Javed, U., Trawny, K., Breitenberger, C., Hidalgo, P. J., Ebben, C. J., Geiger, F. M.,
1674 Corrigan, A. L., Russell, L. M., Ouwersloot, H. G., Vilà-Guerau de Arellano, J., Ganzeveld, L., Vogel,
1675 A., Beck, M., Bayerle, A., Kampf, C. J., Bertelmann, M., Köllner, F., Hoffmann, T., Valverde, J.,
1676 González, D., Riekkola, M.-L., Kulmala, M., and Lelieveld, J.: The summertime Boreal forest field
1677 measurement intensive (HUMPPA-COPEC-2010): an overview of meteorological and chemical
1678 influences, *Atmos. Chem. Phys.*, 11, 10599–10618, <https://doi.org/10.5194/acp-11-10599-2011>, 2011.
- 1679 Yan, C., Nie, W., Äijälä, M., Rissanen, M. P., Canagaratna, M. R., Massoli, P., Junninen, H., Jokinen,
1680 T., Sarnela, N., Häme, S. A. K., Schobesberger, S., Canonaco, F., Yao, L., Prévôt, A. S. H., Petäjä,
1681 T., Kulmala, M., Sipilä, M., Worsnop, D. R., and Ehn, M.: Source characterization of highly oxidized
1682 multifunctional compounds in a boreal forest environment using positive matrix factorization, *Atmos.*
1683 *Chem. Phys.*, 16, 12715–12731, <https://doi.org/10.5194/acp-16-12715-2016>, 2016.
- 1684 Yatavelli, R. L. N., Mohr, C., Stark, H., Day, D. A., Thompson, S. L., Lopez-Hilfiker, F. D.,
1685 Campuzano-Jost, P., Palm, B. B., Vogel, A. L., Hoffmann, T., Heikkinen, L., Äijälä, M., Ng, N. L.,
1686 Kimmel, J. R., Canagaratna, M. R., Ehn, M., Junninen, H., Cubison, M. J., Petäjä, T., Kulmala, M.,
1687 Jayne, J. T., Worsnop, D. R., and Jimenez, J. L.: Estimating the contribution of organic acids to

- 1688 northern hemispheric continental organic aerosol, *Geophysical Research Letters*, 42, 6084–6090,
1689 <https://doi.org/10.1002/2015GL064650>, 2015.
- 1690 Yli-Juuti, T., Mielonen, T., Heikkinen, L., Arola, A., Ehn, M., Isokääntä, S., Keskinen, H.-M., Kulmala,
1691 M., Laakso, A., Lipponen, A., Luoma, K., Mikkonen, S., Nieminen, T., Paasonen, P., Petäjä, T.,
1692 Romakkaniemi, S., Tonttila, J., Kokkola, H., and Virtanen, A.: Significance of the organic aerosol
1693 driven climate feedback in the boreal area, *Nat Commun*, 12, 5637, [https://doi.org/10.1038/s41467-](https://doi.org/10.1038/s41467-021-25850-7)
1694 [021-25850-7](https://doi.org/10.1038/s41467-021-25850-7), 2021.
- 1695 Ylivinkka, I., Kaupinmäki, S., Virman, M., Peltola, M., Taipale, D., Petäjä, T., Kerminen, V.-M.,
1696 Kulmala, M., and Ezhova, E.: Clouds over Hyytiälä, Finland: an algorithm to classify clouds based on
1697 solar radiation and cloud base height measurements, *Atmospheric Measurement Techniques*, 13,
1698 5595–5619, <https://doi.org/10.5194/amt-13-5595-2020>, 2020.
- 1699 Zhang, Y., Peräkylä, O., Yan, C., Heikkinen, L., Äijälä, M., Daellenbach, K. R., Zha, Q., Riva, M.,
1700 Garmash, O., Junninen, H., Paatero, P., Worsnop, D., and Ehn, M.: Insights into atmospheric
1701 oxidation processes by performing factor analyses on subranges of mass spectra, *Atmos. Chem.*
1702 *Phys.*, 20, 5945–5961, <https://doi.org/10.5194/acp-20-5945-2020>, 2020.
- 1703